Biodissolvable Delivery Vehicles for Ultra-Miniature Ultra-Compliant Neural Probes: Fabrication, Characterization, and Insertion Force Analysis

Submitted in partial fulfillment of the requirements for

the degree of

Doctor of Philosophy

in

Mechanical Engineering

Rakesh Khilwani

B.Tech., Mechanical Engineering, Indian Institute of Technology Madras
M.S., Mechanical Engineering, Carnegie Mellon University

Carnegie Mellon University
Pittsburgh, PA

May 2018

Dedicated to my parents,
Sheela and Govind Khilwani
and my extended family

Acknowledgments

First and foremost, I would like to thank my advisor Professor Burak Ozdoganlar for giving me the opportunity to pursue a Ph.D. degree at Multiscale Manufacturing and Dynamics Laboratory. Over so many years he has shown me continuous support, guidance, and patience, for which I owe him a huge debt of gratitude. He has always motivated me to think out of the box and push the boundaries in my research. I deeply appreciate his constructive criticism and friendly admonishment at various times, which has helped me become better at research.

I would like to thank Professor Gary Fedder for his guidance and advice during our collaboration over many years. I would like to additionally thank him for serving on the thesis committee and providing me with valuable feedback. I would also like to thank Professor Aryn Gittis for serving on the thesis committee and providing me with valuable advice and new insights. I would like to express my gratitude to Professor Philip Leduc for agreeing to serve on my thesis committee. I would also like to thank Professor Lee Weiss for providing me with valuable feedback.

I want convey my heartfelt thanks to my friend, Emrullah Korkmaz, who has been there for me through all the ups and downs in my research as well as in my life. I would not have finished my thesis without his constant support and encouragement. Words cannot express the gratitude I have for him. I would like to thank him for his invaluable inputs toward my research and spending many hours for brainstorming with me.

I would like to thank our collaborators on the neural probe project from the ECE department. Especially, I would like to thank Mats Forssell, Dr. Xiao Chuan Ong and Dr. Peter Gilgunn for their collaboration on my research during the early part of my thesis.

I would thank all the people who helped me at various point during my Ph.D. from the MMDL Lab. First, I would like to thank Delin Shi for helping me with the experiments and educating me about physiology of the brain tissue. I would also like to thank the present members of the MMDL lab: Dr. Recep Onler, Dr. Sudhanshu Nahata, Elaine Sung, Shivang Shekhar, Wei Chen, Jonelle Yu, Kadri Bugra Ozutemiz, Ezgi Pinar Yalcintas, Toygun Cetinkaya, Ant Yucesoy, Lisha White, Yusuf Mert, and Ali Alp Gurer for their friendship and help. I would also like to thank the past members of the MMDL lab: Pallavi Gunalan, Bohan Hao, Bin Shen, Dr. Bulent Arda Gozen, Dr. Bekir Bediz, Dr. Nithyanand Kota, Dr. Prashanth Anandan and Gerardo Salas.

I would like to thank Prof. Tracy Cui, Prof. TK Kozai and Xia Li for collaborating with us on the neural probe project. I would also like thank staff members of the mechanical engineering department for sustained support with various aspect during the course of my PhD.

My stay in Pittsburgh wouldn't be enjoyable without my social friend circle. I would like to thank Oluseun Aremu for being a good friend. I would also like to thank Willie Nicholson for being a mentor and providing me with encouragement at all time. I would like to thank and remember Charles Oyenuga who inspired me to be humble and gracious, and my previous roommate and friend Nikhil Sivadas for his sage advice and making my stay in Pittsburgh more pleasant. I would also like to thank Uchenna Mbawuike, Tamala Gee, Nahom Minassie Beyene and Emma Giset for their friendship. I also want to express my gratitude to Xiaofan Wu for providing me with valuable support during the last 12 months of my PhD.

Lastly and most importantly, I would like to thank my parents Govind Khilwani and Sheela Khilwani for their unconditional love and support. I would not be here without the sacrifices they made over the years. I would like to express my gratitude to my grandparents for their blessings and well-wishes. I would also like to thank my sister Pia Tolani and brother-in-

law Vijay Tolani for being my biggest cheerleaders within the family. I would like to thank my cousins Priya, Nikita, Ritesh, Nishant, Nisha, Mayur, Manoj, Rahul, and all my uncles and aunts for creating a wonderful family support structure for me to grow and improve myself.

I would like to acknowledge the Defense Advanced Research Projects Agency (DARPA) Biological Technologies Office (BTO) Electrical Prescriptions (ElectRx) program for providing funding support under the auspices of Dr. Douglas J. Weber through the Space and Naval Warfare Systems Center (SPAWAR) - Pacific, Cooperative Agreement No. HR0011-15-2-0009 and Microsystems Technology Office (MTO) under the auspices of Dr. Jack Judy through the SPAWAR, Pacific Award No. N66001-11-1-4025.

ABSTRACT

Brain-Machine Interfaces (BMIs) have emerged as a viable technology for interacting with central nervous system (CNS) to facilitate understanding different functions of healthy brains and basis of neurological disorders. Neural probes are a fundamental component of BMIs. Stable chronic functionality of neural probes is of utmost importance towards realizing clinical application of BMIs. However, sustained immune response from the brain tissue to the prevailing large and stiff neural probes is one of the major challenges that hinder stable chronic functionality. There is a growing body of evidence in the literature that highly compliant neural probes with sub-cellular dimensions can significantly reduce the foreign-body response, thereby enhancing long-term stability of intracortical recordings. However, a trade-off of reducing the probe size and increasing flexibility of the probe is failure prone insertion of the probes into targeted brain regions. The subcellular-sized and highly-compliant neural probes commonly lack the mechanical strength to penetrate the brain tissue. As such, there is a need for plausible delivery strategies to successfully implant flexible neural probes with sub-cellular dimensions.

One of the most promising approach is to use a delivery vehicle in the form of a micro-scale needle made from dissolvable and biocompatible materials. During penetration/placement of the probe, the needle provides sufficient strength and stiffness, and subsequently dissolves away, leaving behind only the ultra-compliant, ultra-miniature neural probe. As such, a short-term placement of the delivery needle considerably reduces the chronic damage to the brain tissue with respect to permanent placement of a similarly-sized probe.

Although biodissolvable delivery vehicles offer attractive advantages, significant further advances are needed to address critical challenges for their design, fabrication, and application. These challenges involve (1) *design*, including selection of needle geometry and materials; (2)

fabrication, including accurate and reproducible manufacturing approaches; and (3) *characterization*, including analyses on both their geometric and mechanical properties, as well as on the relationship between insertion forces and design/insertion parameters.

In this doctoral research, we propose a novel biodissolvable neural probe delivery vehicle concept for effective, precise, and reproducible delivery of ultra-miniature and ultra-compliant probes to targeted brain regions. The ***overarching objectives*** of this doctoral research are to devise and evaluate a new manufacturing strategy for accurate and reproducible fabrication of biodissolvable delivery vehicles with desired geometries; *and* to understand the relationship between the needle design and insertion conditions towards identifying favorable insertion and design parameters. To address these objectives, we developed novel fabrication techniques for accurate and reproducible manufacturing of biodissolvable delivery vehicles (for ultra-miniature and ultra-compliant probes) with diverse geometries and from different biocompatible and dissolvable materials. We then studied the effects of design parameters and insertion speeds on insertion forces for non-dissolvable and biodissolvable delivery vehicles towards gaining a comprehensive understanding on the tissue-needle interaction.

Table of Contents

List of Tables

List of Figures

Chapter 1

Introduction

1.1 Research Motivation

Brain machine interferences (BMIs) or brain computer interfaces (BCIs) have emerged as a viable technology for interacting with central nervous system (CNS) to facilitate understanding, mitigating, and treating neurological disorders, as well as towards understanding how the brain works [1,2]. Neural probes, which are a fundamental component of BMIs or BCIs, are employed to record neural activity for the brain cortex in the form of action potential or to provide electrical stimulation to the brain tissue [3,4]. Stable chronic functionality of intracortical probes is of utmost importance towards realizing clinical application of BCIs. Furthermore, the strength and quality of the recorded neural signals, i.e., high signal-to-background ratio (SBR), are vital for the success of BCIs [5–8]. As such, effective functioning of BCIs requires neural probes that will provide stable chronic functionality with high neural signal quality.

Sustained immune response from the brain tissue to the neural probes (foreign-body response) is one of the major challenges that hinder their stable chronic functionality [9-11]. The prevailing commercial neural probes are considerably larger than the neurons and are very stiff [12-24]. When applied chronically, the relative motion (micromotion) between the large and stiff probes and the brain tissue induces formation of glial scarring, which produces a glial shield surrounding the probes [29,30]. The glial shield first deteriorates the quality of the recorded signals, and eventually renders the probe completely non-functional [25-27].

There is a growing body of evidence in the literature that highly compliant neural probes with sub-cellular dimensions can significantly reduce the foreign-body response, thereby enhancing long-term stability of intracortical recordings [28-37]. By increasing the probe compliance, the mechanical mistmatch between the probes and brain tissue is reduced, such that the micromotion-induced strains are minimized [30-37]. In addition to its effect on reducing the probe stiffness, smaller size of the probes may reduce the physiological response to the foreign body [30]. As such, new approaches are needed for developing miniature probes with high compliance to achieve reliable functioning of BMIs towards clinical applications.

Towards addressing the aforementioned needs, research efforts have been devoted to manufacturing implantable probes with more flexibility and smaller footprint [37-39]. However, a critical trade-off of reducing the size and increasing flexibility of the probes is failure-free insertion of the probes into the brain tissue and their precise placement to the targeted locations in the brain. The subcellular-sized and highly compliant neural probes commonly lack the mechanical strength to penetrate the brain tissue without failure [37]. Moreover, even if the penetration is accomplished, the highly compliant probes can experience significant deflection inside the tissue, thereby hindering precise positioning of the electrodes [30]. As such, there is a need for strategies to successfully implant flexible neural probes with sub-cellular dimensions.

A number of techniques have been explored towards enabling effective implantation of miniature and flexible neural probes into the brain tissue. Among those, one of the most promising approach is to use a delivery vehicle in the form of a micro-scale needle made from dissolvable and biocompatible materials [40-47]. The ultra-compliant miniature probe is either embedded in or assembled onto the dissolvable needle. During penetration/placement of the probe, the needle provides sufficient strength and stiffness, and subsequently dissolves away, leaving behind only the ultra-compliant, ultra-miniature neural probe [46]. It was also

demonstrated in the literature that a short-term placement of the delivery needle considerably reduces the chronic damage to the brain tissue with respect to permanent placement of a similarly-sized probe [48].

Although biodissolvable delivery vehicles offer attractive advantages, significant further advances are needed to address critical challenges for their creation and application. These challenges involve (1) *design*, including selection of needle geometry and materials; (2) *fabrication*, including accurate, reproducible, high-throughput, and robust manufacturing approaches; and (3) *characterization*, including analysis on both their geometric and mechanical properties, as well as on the relationship between insertion forces, and design/insertion parameters. As such, further research in those areas are needed towards realizing advanced biodissolvable delivery vehicles and associated manufacturing paradigms.

Realizing true potential of biodissolvable delivery vehicle integrated miniature and compliant probes depends critically upon precise and effective insertion of the delivery vehicle into the brain tissue in a minimally invasive manner [14, 30]. To be a clinically viable strategy, biodissolvable delivery vehicles must be capable of reproducibly delivering the integrated probes to the targeted brain regions without a mechanical failure. Insertion performance of biodissolvable neural probe delivery vehicles is highly correlated with the delivery needle design (material, tip shapes, sharpness, cross-sectional shape and size) and insertion conditions (mainly, the insertion speed, and possibly vibration assistance) [49-52]. Ideally, the selected needle design and insertion conditions should result in delivery of the integrated probe (needle and electrode/wiring) to the targeted brain regions with minimal insertion forces and subsequent rapid dissolution of the delivery needle, thereby minimizing the tissue damage, and in turn, unwanted immune response which deteriorates the neural signal quality over time [14,15,53]. Therefore, it is important to understand the effects of the needle design parameters and insertion

conditions on insertion performance towards determining favorable needle design parameters and insertion conditions for successful implementation of the neural probes.

A number of research groups have studied the effects of probe geometry (mostly for the stiff and large neural probes) and insertion conditions on insertion forces in brain-mimmetic polymers (e.g., agarose) [54-56]. However, a comprehensive analysis, including probe (including the needle) design parameters and insertion conditions, has yet to be completed. Specifically, there is still an important knowledge gap in fundamental understanding of the contribution of probe design and insertion conditions on force profiles and associated force components (elastic deflection, penetration, cutting, and friction forces). In addition to using brain-mimetic polymers, to be relevant, such an analysis should also include experiments on actual brain tissue. Such an analysis is particularly important for the integrated probes proposed here, since our proposed neural probe/insertion needle approach provides considerable freedom in selecting needle design parameters and insertion conditions.

A comprehensive research approach is critically needed to address the aforementioned challenges in design, fabrication, and characterization of the biodissolvable delivery vehicles. In particular, a novel manufacturing strategy should be devised to enable accurate and reproducible fabrication of biodissolvable delivery vehicles with diverse geometries and from a myriad of biocompatible and dissolvable polymers. The insertion behavior should also be analyzed for a broad range of needle designs and insertion conditions towards optimal design of the delivery needle and optimal insertion performance.

1.2 Literature Review

1.2.1 Neural probe concepts: Fabrication and characterization

To advance the BMIs toward addressing the aforementioned needs, a number of groups have developed metal and silicon implantable neural probes, e.g., [9-11]. Those studies have demonstrated successful acute recordings and stimulation, as well as promising advancements in channel count and precise targeting of the desired locations in brain. However, for chronic applications, simultaneously achieving high signal-to-noise ratio (SNR) and long-term recording stability still remains a tremendous challenge.

The data in the literature strongly suggest that sustained inflammatory response of the brain tissue to neural probes is one of the leading causes of failure for the prevailing interface technologies used in chronic recording and stimulation applications [12-14]. A majority of the existing neural interface devices include stiff probes with large cross-sectional footprint relative to the neural cells [18-23]. These probes were seen to cause a reactive tissue response from the brain tissue, involving activated astrocytes and microglia, which form a glial shield around the electrode [10-27]. The resulting glial scar and the associated "kill zone" that are characterized by degenerated or dead neurons surround the recording site [25,26]. Although glial scarring stabilizes 5-12 weeks after implantation, the inflammatory response as indicated by microglia activation continues for chronic periods, arising from the persistent presence of the probe [13-14]

The current literature suggest that this response is caused by multiple and confounded effects, including the strain imposed on the tissue due to the micromotion between the probe and the tissue [57-61], breaching of the blood-brain barrier (BBB) throughout the implantation period [62,63], meningeal ingrowth through the probe shafts [64-65], and re-injury caused by mechanical impact, such as collisions and falls [57,59,66,67]. Moreover, the large size of the

silicon or metal probes aggravates the inflammatory tissue response, and thus, further impedes the recording or stimulation quality and longevity [14,28-30].

Previous studies suggest that highly compliant implants with mechanical compliance close to that of the brain tissue, and subcellular sized neural probes could significantly reduce chronic tissue response and improve long term recording stability [28-30,32-35]. To this end, recent research efforts have been devoted to manufacturing implantable probes with more flexibility and smaller footprint. Biocompatible polymers, such as polyimide, parylene-C, and polydimethylsiloxane (PDMS), have been employed for creating flexible probes with subcellular-sized features [29]. Subcellular dimensions further reduce the tissue strain resulting from volumetric displacement of the tissue resulting from the accommodation of the probe volume during insertion [30]. The reduced tissue strain from size and flexibility is understood to reduce production of pro-inflammatory cytokines around the implant and improve tissue health (16). However, a trade-off of reducing the probe size and of increasing flexibility is the challenge of inserting the probes into the brain tissue without failure and precisely delivering them to the targeted location in the tissue. Subcellular-sized and highly compliant probes commonly do not possess mechanical strength to penetrate the pia without failure [37]. Moreover, even when the penetration is accomplished, the high-compliance probes can experience significant deflection inside the tissue, thereby hindering precise positioning of the electrodes [14]. As such, there is a need for plausible strategies to successfully implant flexible neural probes.

A number of techniques have been explored toward enabling effective implantation of neural probes. One approach is to use a rigid insertion vehicle during the insertion of the probe. O'Brien et al. [51] integrated flexible microelectrode arrays with a temporary rigid (silicon) insertion device in a single sequence of fabrication steps. The insertion device was removed after probes were placed in the tissue; however, the flexible probe needs to have sufficiently large cross-

sectional footprint and stiffness to overcome hydrophobic adhesion to the shuttle. Although this adhesion can be reduced by using hydrophilic surface chemistries [39], the array design space remains restricted to linear geometry. Furthermore, and importantly, the rigid shuttle induces considerable stab wound injury [68] used polyimide probes and attached them to a 10 μm-thick silicon backbone layer to enhance the structural stiffness for insertion and precise targeting. However, this non-removable stiff silicon backing negates the flexibility of the polyimide-based electrodes. Therefore, these methods of using stiff insertion devices (either removable or non-removable) restrict the achievable probe designs and limit the functionality and flexibility.

More recently, alternative approaches that utilize dissolvable and biocompatible polymers has emerged for enabling implantation of flexible neural probes. Integration of the biodegradable (and/or dissolvable) polymers provide sufficient stiffness and strength to enable failure-free and precise penetration of flexible probes into the brain. As such, these insertion devices offer attractive advantages over non-dissolvable insertion devices, including retention of probe flexibility and functionality, and reduction of insertion forces and acute inflammation. The biocompatible polymers then degrade or dissolve over a period of time, leaving behind the flexible probe while minimizing the tissue damage. In one approach, the flexible probes are dip-coated with biodegradable polymers [40,42,43]. A range of biodegradable and biodissolvable materials, including polyethylene glycol (PEG) [45], poly(lactide-co-glycolide) (PLGA) [69], tyrosine-derived polycarbonate [43], silk [70], maltose [71], and gelatin [46] have been successfully used for coating flexible neural probes. However, dip-coating methods present challenges in creating needles with controlled tip sharpness and thickness uniformity and limit the needle shapes that can be created. Therefore, it is difficult to achieve the appropriate stiffness and sharpness in a reproducible manner. A recent study introduced the drawing lithography technique, which was shown to improve reproducibility of coating geometries [71]. In an

alternative approach, a set of channels was first created in the probe substrate during fabrication and was then filled with biodegradable polymers for stiffening [72]. However, these designs require a fluidic channel to be filled with biodegradable material to reach the critical stiffness for insertion. This channel then results in a larger implanted footprint, potentially increasing the area of damage in the brain tissue. As such, more advanced biodissolvable delivery vehicles and associated new manufacturing paradigms with high geometric and material capabilities, i.e., design flexibility and suitable materials with the desired mechanical properties, are desirable for successful implementation of flexible neural probes.

To this end, a novel approach was introduced where the ultra-flexible probes were embedded in dissolvable insertion needles that were fabricated by micromolding. Using the micromolding approach enables fabricating insertion needles with desired and favorable geometries. More recent studies used similar techniques to embed or attach the probes to dissolvable or biodegradable delivery vehicles [45-46,73]. Different dissolvable and biodegradable materials, including CMC and its blends, gelatin, and tyrosine-based polymer have been used for the insertion needle.

1.2.2 Insertion characteristics of neural probe delivery vehicles

Damage and trauma caused during the invasive insertion procedure causes mechanical damage to surrounding tissues and the extracellular space which also adversely affects both acute and chronic signal quality. Therefore, it is important to have an optimal needle design that has minimal footprint, appropriate insertion velocity while at the same time sufficient factor of safety to avoid any failure during insertion. Insertion force profile measured during needle penetration into brain provides us with an important insight into the different types of forces involved during the entire insertion process. As suggested in the literature, different attributes of the force profile

are potentially co-related to different scaring mechanisms. For example, large dimpling during the insertion process leads to higher compressive strain which in turn leads to higher risk of hemorrhage [67]. From the same force profile, dimpling force is useful information to analyze/predict the buckling failure of the needle at that moment of insertion. Similarly, other components of force profile such as cutting force, shaft friction force and relaxation time have been shown to have an impact on tissue damage. Hence, accurate measurement and analysis of different force components during needle insertion is an important step to achieve optimal probe deign for minimal tissue damage.

Over the past two decades, a number of research groups have reported the effect of probe geometry on insertion force in brain. The major parameters that have been explored are cross-section area, tip sharpness, tip angle and shank roughness. Some groups [51] used sharpened 50 and 150-micron dia. (10° tip angle) Tungsten probes and determined the maximum force to be 0.99 and 1.65 respectively. Blunt probes of stainless-steel wire with larger cross-sectional areas (200 μm diameter) required two to four times higher force to penetrate tissue than their narrower, 100 μm diameter counterparts [74]. These results are consentient as the larger diameter probe will displace larger volume of material along it insertion track resulting in larger force. [70] showed using a full factorial experiment with wedge silicon probes using three thickness (150, 100 and 50 μm) and three widths (200, 300 and 400 μm), that increase in thickness had more significant influence on increase in penetration force for lower probe widths as compared to larger probe widths. The maximum force increased with increase in width and thickness while other parameters were kept constant. However, the combination effect of width and thickness was unclear from the analysis presented.

Apart from the cross-sectional area of the probe, tip shape of the probe is very important factor during the insertion process. The larger the tip apex angles of the probe, the higher the

penetration force. Probes with opening angles of less than 20° were shown to easily penetrate the dura without dimpling the surface, whereas probes with opening angles greater than 40° to 50° made penetration of the dura difficult [71]. Tip apex angle was shown to be one of the greatest determiners of insertion force for wedge silicon probes. Making the tip angle of the probe smaller, significantly reduced probe insertion forces necessary to penetrate pia [70]. Hosseini et al. [72] used probe having various tip shapes such as wedge, conical sharp and beveled for the force insertion experiments. The metal conical wire had the lowest penetration force (approximately 30% lower), however all the probes had different material and cross-section size making an one-on-one comparison between different tip shapes rather difficult. Moreover, the penetration forces obtained in this study was much higher (13mN-47mN) as compared to other studies discussed previously (<2mN) for similar probe shapes and animal. Sharp et al. [2009] showed that a conical sharp tip has significantly lower dimpling, penetration force and maximum force as compared to a flat punch of the same size (200 μm diameter).

The precise insertion speed to surgically implant a probe is the subject of debate and conflicting results in the literature further confound the selection process. It has been postulated that while rapid insertion can compensate for poor tip design by allowing for penetration in circumstances where geometrical considerations would make penetration prohibitive, slower insertion speeds may be advantageous in allowing time for surrounding tissue to accommodate around the probe, thereby attenuating compressive and tensile forces of surrounding brain tissue [71]. Traditionally, insertion speeds range from slower insertion speeds around 10 μm/s to as high as 2 mm/s. Penetration force for sharp-tipped silicon probes was shown to decrease significantly as insertion speed was reduced within the range from 100 to 10 μm/s [70]. Similar lower insertion forces were observed for stainless steel wires inserted at speeds of 10 μm/s when compared to 1 mm/s [75]. This was hypothesized to be due to the viscoelastic nature of brain

tissue which causes an increase in brain stiffness as insertion speeds increase. However, another reported no significant difference between penetration forces for Parylene coated silicon probes implanted at different insertion speeds in this range [73]. Another study [74] using a round flat probes were shown to increase the insertion forces (235 μm) over a wider range of speed from 100 μm/s to 10mm/s. The physical damage is tissue was seen to increase with speeds as well.

However, other studies seem to indicate that slower insertion speeds cause greater degrees of biological damage. In one study, insertion speeds of 125 μm/s, on the slower end of the range of insertion speeds, actually caused increased vascular damage, independent of tip geometry, as compared to faster insertion speeds of 2000 μm/s in an ex vivo study [Brjohnson et al. 2006]. This is supported by another study, in which specialized electrodes for extracellular pH recordings noted longer periods of acidosis, a witness for tissue homeostasis and the presence of blood along the insertion tract, for slower (50 μm/s) insertions as compared to faster insertions at 0.5 or 1 mm/s [35]. In another study, exploring the same range of insertion speeds, using an electrochemical force sensor to evaluate insertion mechanics, researchers found that although increasing insertion speeds increased axial forces experienced by the probe, they found that the shear forces caused by friction between tissue and probe faces decreased [75.]. This could be a plausible explanation as to why slower insertion speeds are reported to decrease overall forces, but counterintuitively increase vascular damage and cause more disruption to brain tissue homeostasis.

Use of insertion shuttles as well as soluble neural probes which have gained traction over past decade as discussed earlier gives a greater flexibility for design of insertion shuttle as well choosing from wide range of materials including polymers and resins [54,55,62,63]. The stiffness of these polymer shuttles as well soluble probes (1-5 GPa) are 1 or 2 orders of magnitude much lower than that of Si (50 GPa) and tungsten, making them much more vulnerable to buckling and

bending during insertion [79]. Moreover, pyramid shaped shuttles can be potentially used for such applications which cannot be achieved using planar lithography processes used for fabrication of Si probes [70]. Therefore, use of soluble probes which can be attached or bonded to insertion delivery vehicle device offer more flexibility in needle design. For such needle designs and materials, it is even more critical to have the knowledge of penetration forces to ensure good factor of safety as well as chose the right insertion velocity as bio-soluble needle would absorb moisture from the surrounding tissue. One study [76.] showed that at low speeds (100μm/s) the ECM material used as delivery vehicle absorbed moisture causing it to "buckle" in agarose phantom model. This was co-related to non-linear increase in insertion force which wasn not the case at higher speeds.

Despite all these studies there is a lack of fundamental understanding of different types of forces acting on the tissue. Separation of overall forces into its components like cutting force, friction force and elastic deflection force is still not well understood. These forces are extremely critical as they influence different type of injury and trauma mechanism in the brain. In order to have a thorough understanding of the effect of geometry and speed, it is important to have a deeper insight into these different force components and how they vary individually with geometric parameters. Many groups have used the retraction force profile or the drag force to calculate the friction force at different velocities [74]. However, since the needle starts from zero velocity as compared to a steady state velocity during insertion, the effect of stick-slip during transition from static friction to dynamic friction during the acceleration process would be reflected in the obtained friction force values. Moreover, different regions of brain exhibit different mechanical properties and the inhomogeneity of the brain makes it hard to conduct an organized study to have a fundamental understanding of these forces.

Agarose gel has been widely used in literature as a model for brain tissue. A 0.6% (w/w) agarose gel is shown to have similar Young's Modulus (6KPa) as that of brain tissue, as well as shown to have similar mechanical properties [80]. 0.5% is considered a good representation of grey matter and 0.83% for that of pia membrane [76]. 0.6% is used as a good representation of the overall brain stiffness [54]. Some researchers have used 0.8%, 1% and even higher concentrations however there is a general consensus about using 0.6% as an appropriate phantom model[77-79]. Hosseeni et al. [77] conducted insertion experiments using 0.6% agarose gel along with a thin plastic sheet on top and showed them to be a fair representation of brain with dura for insertion force studies. However, another study has shown that agarose and brain tissue are not a good representation while inserting with a blunt round probe [80]. The authors reported to have significant difference between penetration forces obtained from brain and agarose in addition to opposite effect of velocity on forces.

However, there are significant advantages of using a phantom model like agarose gel to conduct comprehensive experimental study to evaluate the effect of geometric parameters and insertion conditions [54,75]. Agarose gel is homogenous unlike brain and can be cast into fixed thickness agar blocks which is hard to do with brain tissue. The insertion forces using a 0.6% agarose gel are of the same order as that obtained from insertion into brain [77]. Moreover, the translucent property of agarose gel enables us to observe the insertion event and correlates the force data measured to the optical observation [81]. Lastly, both materials exhibit similar viscoelastic properties of strain rate hardening as shown in the literature even though they would have different strain hardening parameters [78-79]. Hence, a 0.6% agarose gel is prominently used by several research groups for validation of neural probe design to demonstrate successful insertions and used to mimic force measure during probe insertion, can be considered to conduct

a comprehensive insertion force study using a variety of geometric parameters, insertion conditions and materials.

1.3 Research Objectives

The aforementioned challenges in design, fabrication, characterization, and insertion of the biodissolvable delivery vehicles for precisely and reproducibly implementing the miniature and compliant neural probes to the targeted brain regions uncover the important need for conducting a comprehensive research in this field. In particular, it is necessary to devise a novel manufacturing strategy for accurate and reproducible fabrication of biodissolvable delivery vehicles with diverse geometries and from a myriad of biocompatible and dissolvable polymers, as well as to study the insertion behavior of these vehicles for a broad range of delivery needle designs and insertion conditions towards optimal design of the delivery needle and optimal insertion performance.

In this doctoral thesis research, we propose a novel biodissolvable neural probe delivery vehicle concept for effective, precise, and reproducible delivery of ultra-miniature and ultra-compliant probes to the targeted brain regions. The ***overarching objectives*** of this doctoral research are to devise and evaluate a new manufacturing strategy for accurate and reproducible fabrication of biodissolvable delivery vehicles successfully integrating ultra-miniature with desired geometries; *and* to understand the relationship between the needle design and insertion conditions towards identifying favorable insertion and design parameters.

The **specific objectives** of this research are: **(1)** to devise novel fabrication techniques for accurate and reproducible manufacturing of biodissolvable delivery vehicles (for ultra-miniature and ultra-compliant probes) with diverse geometries and from different biocompatible and dissolvable materials; **(2)** to analyze the effects of design parameters and insertion speeds on

needle insertion forces in agarose phantom gel and brain tissue for non-dissolvable and biodissolvable needles. It is noted that the latter objective also provides important information regarding insertion of non-dissolvable probes, such as the prevailing lithographically-fabricated probe arrays.

1.4 Research Contributions

Our research has resulted in new manufacturing strategies and their assesment (Objective 1) in of their accuracy, reproducibility, and geometric/material capabilities. These novel manufacturing strategies enabled effective fabrication of biodissolvable delivery vehicles with diverse geometries and from a myriad of biodissolvable material compositions. We have demonstrated that ultra-miniature and ultra-compliant neural probes can be integrated into or assemble onto the delivery needles. Furthermore, we conducted a preliminary evaluation of the produced delivery vehicles, demonstrating successful penetration and subsequent dissolution of the fabricated biodissolvable delivery vehicles into the brain tissue and agarose. Importantly, *in vivo* studies performed with our collaborators demonstrated successful dissolution of our biodissolvable delivery vehicles upon effective penetration into living rodent brain.

Next, towards understanding design and insertion parameters on insertion characteristics of biodissolvable delivery vehicles (Objective 2), we designed and constructed a custom experimental setup that enables reproducible insertion of neural probes into brain tissue and agarose. To this end, we designed and constructed a custom load cell that enables accurate measurement of mN-level insertion forces experienced during needle insertions. Subsequently, we conducted a comprehensive experimental study on insertion of delivery needles for measuring insertion forces with different needle designs and insertion conditions. In this study, we used both freshly excised rat brain and agarose gel as the insertion samples. Agarose gel is widely

used in the literature as a tissue phantom for brain. Furthermore, we used a *non-dissolvable* needle material (i.e., VeroWhite resin) to better facilitate the large number of experiments. The obtained results provided previously unrevealed insights related to the insertion characteristics of neural probes and/or their delivery vehicles.

An experimental study with *biodissolvable* delivery needles on both rat-brain tissue and agarose gel is then conducted towards gaining a more relevant understanding for successful implementation of our probes. These studies provided important information on the effects of various geometric parameters, insertion conditions and materials on insertion forces. This information can be used to identify optimal design of probes or delivery vehicles towards withstanding needle failure, preventing tissue damage and mitigating insertion failures. Especially in the case of inserting *biodissolvable* needles into agarose and brain tissue, both of which are water rich environments, a minimum insertion velocity is determined as water absorption during insertion process increases the overall forces.

The ***scientific contributions of this Ph.D. thesis research*** are:

1. Novel micromanufacturing strategies for accurate and reproducible fabrication of biodissolvable delivery vehicles (microneedles) that enable delivery of ultra-miniature ultra-compliant probes into the brain [40-41, 84];
2. Characterization of the developed microneedle manufacturing techniques in terms of accuracy and reproducibility, as well as of geometric and material capabilities [85];
3. A direct assembly approach to integrate the probe and the biodissolvable delivery vehicle to improve yield and expand design space for parametric design studies;
4. A comprehensive understanding on the effects of needle design parameters and insertion conditions on insertion force profiles when inserting non-dissolvable or dissolvable delivery needles into both brain mimetic agarose and excised rodent brain (in preparation, to be submitted to Biomedical Microdevices).

Chapter 2

Fabrication, Design and Characterization of Dissolvable Delivery Needles

Building upon the works in the literature, in this chapter, we describe the design, fabrication and initial evaluation of an ultra-miniature ultra-compliant intracortical probe technology toward addressing the aforementioned challenges of chronic recording capability. The probe wiring, which is made from a platinum core and parylene-C insulation, has micron-scale cross-section and meandered geometry, resulting in very high compliance in both axial and lateral directions. A finite-element analysis is performed to determine the stiffness of the ultra-compliant probes, as well as to compare the strain distribution in the tissue between the ultra-compliant probes and stiff Si probes. Importantly, to enable failure-free penetration and precise positioning of the probes in the brain tissue, the electrodes and wiring are encased in a micromolded dissolvable needle. As described in Figure 2.1, upon insertion, the needle material dissolves away, leaving behind the ultra-compliant ultra-miniature electrodes and wiring. The dissolvable needle can also be used to co-deliver anti-inflammatory agents to the implant site to reduce the chronic tissue response. Our approach decouples electrode and needle designs, thereby enabling selection of both the needle material and the needle design to achieve minimal forces during insertion and rapid dissolution after implantation. To further enhance the success of probe application, an automated insertion device that enables controlling the penetration speed and depth is

constructed. Penetration of the needles into cadaveric brain tissue and dissolution of the needles in an agarose model are then demonstrated.

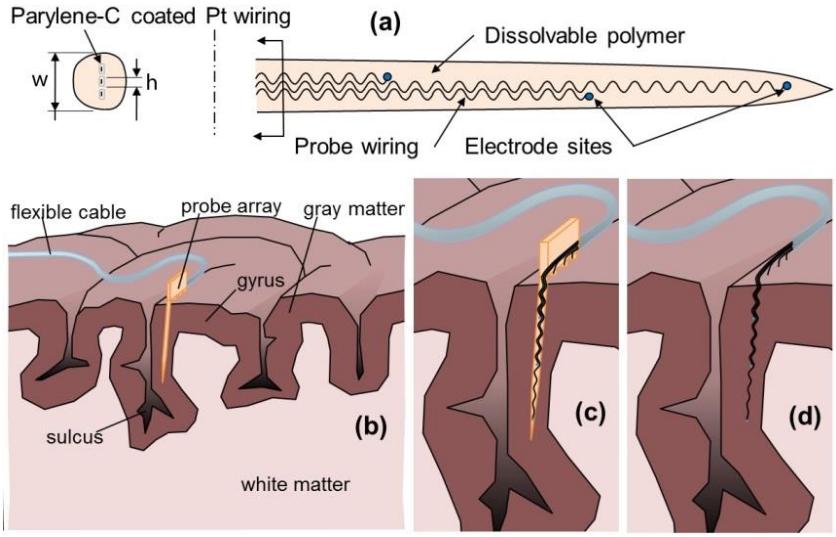

Figure 2.1: The concept of ultra-miniature, ultra-compliant probes: **a.** Probe with multiple electrodes and insulated wires, along with the dissolvable polymer needle; **b.** A probe array is inserted into cortical tissue, with flexible cabling; **c.** Close-up image showing the probe with dissolvable materials; **d.** After dissolution of the needle, only miniature wires remain.
*(Courtesy: Prof. Gary K. Fedder, CMU)

2.1 Materials and Methods

2.1.1 Probe and needle design

The cross-section and the plan view of the probe, including the insulated wiring and the electrode, are given in Figure 2.2. The conductive portion of the wiring is 0.5 μm-thick, 4 μm-wide platinum (Pt). Conformal 1.1 μm-thick layers of parylene-C (Px) encase the Pt as electrical insulation. To attain high compliance along the probe insertion direction (i.e., the probe axis), the wiring is meandered. The meander is composed of circular arcs, including a meander amplitude a_m, a meander radius r_m, a meander period p_m, and a meander angle θ_m, as defined in Figure. 2.2(d). This geometry with the circular arcs is chosen to obtain a smooth stress distribution within the wiring. In this work, the meandered wiring geometry with $r_m = 158\,\mu\text{m}$,

$a_m = 15\ \mu m$, $\theta_m = 113°$ and $p_m = 265\ \mu m$ is selected. A 20 μm diameter disk-shaped Pt electrode, which is insulated with Px at the bottom but exposed at the top, is integrated at the tip of the meandered wiring. The cross-sectional geometry and the meander parameters together dictate the overall compliance of the probe once the insertion needle is dissolved.

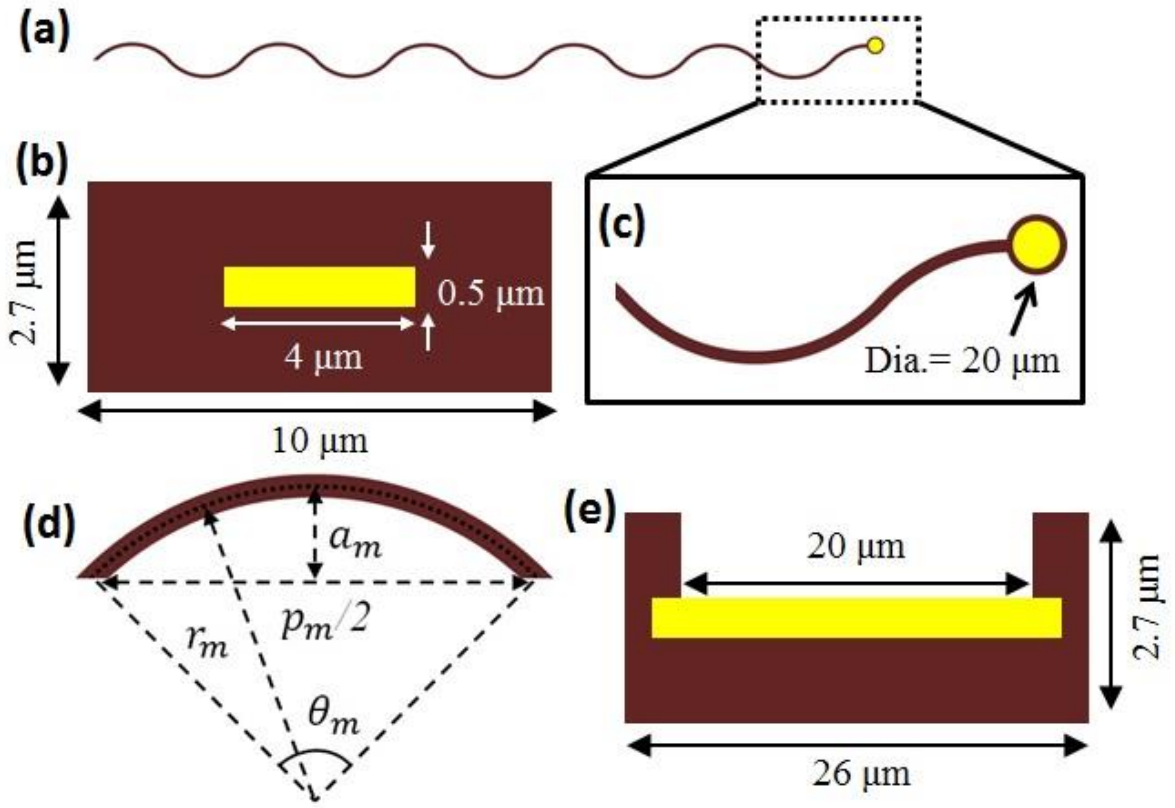

Figure 2.2: Meandered probe design**: a.** The plan view of the meandered wiring of the probe; **b.** The cross-section of the wiring with Pt core and Px insulation; **c.** Zoomed-in plain view of the electrode; **d.** Geometric parameters of the semi-circular arcs used for meandered wiring ($\theta_m = 113°$); **e.** The cross-section of the circular electrode

The generic design of the dissolvable needle that encapsulates the probe is given in Figure 2.3. The needle geometry is characterized by the needle length l_n, needle width w_n, needle thickness t_n, tip angle θ_t, needle-tip radius r_t, and a relief angle θ_r, which can be positive or negative. To increase the factor of safety of the needles against failure during insertion, base fillets with fillet radius r_f are included in the design. Further, to facilitate the handling of the

probe and to protect the connector wiring outside the needle during insertion, a dissolvable tab is included in the design.

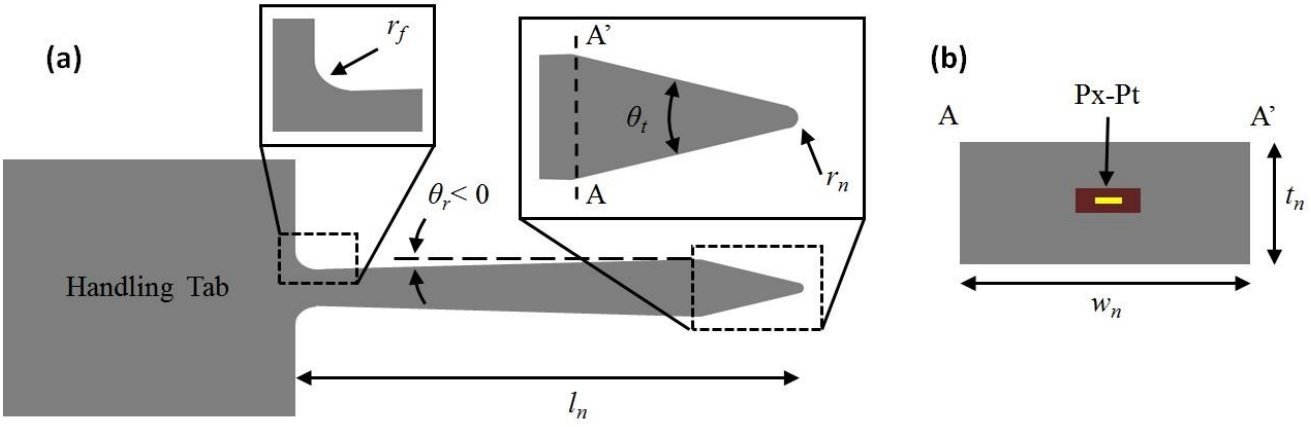

Figure 2.3: Geometric parameters of the dissolvable insertion needle: **a.** The plan view of dissolvable needle; **b.** The cross section of the needle and Px-Pt probe at plane AA'.

2.1.2 Probe-tissue interaction

A three-dimensional finite-element model is constructed to determine the stiffness of the Pt-Px probe, and to compare brain-tissue interaction of the Pt-Px probe with that of a stiff Si probe (COMSOL Multiphysics). The tissue material is modeled as linear elastic with a Young's modulus of 6 kPa and a Poisson's ratio of 0.45 [58]. A total tissue cube volume of 5 mm on a side is chosen. For the calculation of the probe stiffness, the left-end of the probe is fixed, a unit load is applied to the probe tip in each of the three orthogonal directions, and the deflections at the tip are noted to calculate the stiffness. For the static analysis, in which the probe is considered to be pulled from where it is anchored to the bone, all the external coordinates of the tissue volume are fixed. For the dynamic analysis, a motion of prescribed amplitude and frequency are imposed to the tissue through the boundary coordinates in the form of base excitation. Both the tissue and the probes are meshed using tetrahedral elements.

A silicon probe with rectangular cross section (125 μm-wide, 25μm-thick shank, with a taper at its tip) and 1.5 mm length, resembling the geometry of a NeuroNexus probe [30], is considered for the stiff probe. For Si, Young's modulus of 200 GPa and Poisson's ratio of 0.3 are used. For the meandered probes, which are composed solely of Pt and Px layers after the dissolution of the needle material, average material properties of 3.3 GPa Young's modulus and 0.3 Poisson ratio are used. The effective average Young's modulus is calculated based on the equivalent area moment of inertia of the Px (2.8 GPa) and Pt (168 GPa) portions of the cross section. The probe-tissue boundaries are modeled such that the boundary elements are fixed to one another in all degrees of freedom. The convergence with mesh size of the model is verified to ensure the precision of the results.

In both static and dynamic analyses, the left end of each probe is fixed (to emulate attachment to the skull) at 1.5 mm away from the tissue surface[57-58]. The static analysis is performed by imposing an axial displacement of 30 μm (away from the brain tissue) at the fixed base of each probe. For dynamic analysis, responses to axial and lateral motions are studied. For both cases, a sinusoidal motion at 1.2 Hz frequency and 30 μm amplitude is imposed on all the boundary coordinates of the tissue section to represent tissue micromotion.. For each analysis, the strain distribution within the tissue surrounding the electrode is determined.

2.1.3 Wiring, electrode and etch pit fabrication

The Px-Pt probe is made on a silicon handle wafer using standard batch microfabrication techniques. Figure. 2.4 shows the steps in fabrication of the wiring, the electrode, and the etch pit. First, a 1.1 μm-thick Px layer is deposited on a clean 4-inch Si wafer substrate using a vapor deposition system (SCS Labcoter®2 Parylene Deposition System). Second, a 0.5 μm-thick Pt layer is deposited on the Px layer using a sputtering system (Perkin-Elmer 2400-6J). Next, a layer

of photoresist (AZ4210, Merck KGaA) is spin-coated (Solitec Photoresist Spinner) on top of the Pt layer and baked in an oven at 90°C for 20 min. The photoresist is then exposed using a chrome-on-glass mask (on a Karl-Suss MA6 contact aligner) with the desired patterns for the Pt wire and electrode. The photoresist is developed and following an oxygen plasma clean (IPC Barrel etcher), the exposed platinum regions are removed by ion milling (Commonwealth Scientific Ion Mill). The remaining photoresist is removed in acetone with application of ultrasonic vibration. After another oxygen-plasma cleaning step, another 1.1 μm-thick Px layer is deposited onto the wafer (Figure 2.3g). A 20 nm-thick chromium (Cr) layer is then deposited using a sputtering system (Perkin-Elmer 2400-8L) to protect the Px layer during plasma etching. This is followed by deposition, patterning, and exposure of another photoresist layer, and etching the exposed Cr regions. The remaining photoresist and Cr are then removed using a stripper (Microposit™ Remover 1165, Dow) and chromium etchant, respectively. The design includes a set of Px tethers without Pt to suspend the wiring and the electrode over the etch pit.

To ensure that the wiring and the electrode are fully embedded in the dissolvable needle, our approach involves the use of a two-part mold: the bottom portion of the two-part mold is formed on the Si wafer and includes the tethered wires and electrode suspended over an etch pit. The etch pit is of the same geometry as the needles, with a depth of 60 μm, which is close to the half the targeted needle thickness. To create the etch pit, after depositing a 20 nm-thick Cr layer, a photoresist layer is spin-coated, baked and the desired pattern for the bottom molds is exposed. The photoresist is then developed, and following oxygen plasma cleaning, the exposed chromium regions are etched. Deep reactive ion etching (DRIE, STS Multiplex ICP RIE) is then used to create the etch pit. Subsequently, the photoresist and Cr are removed.

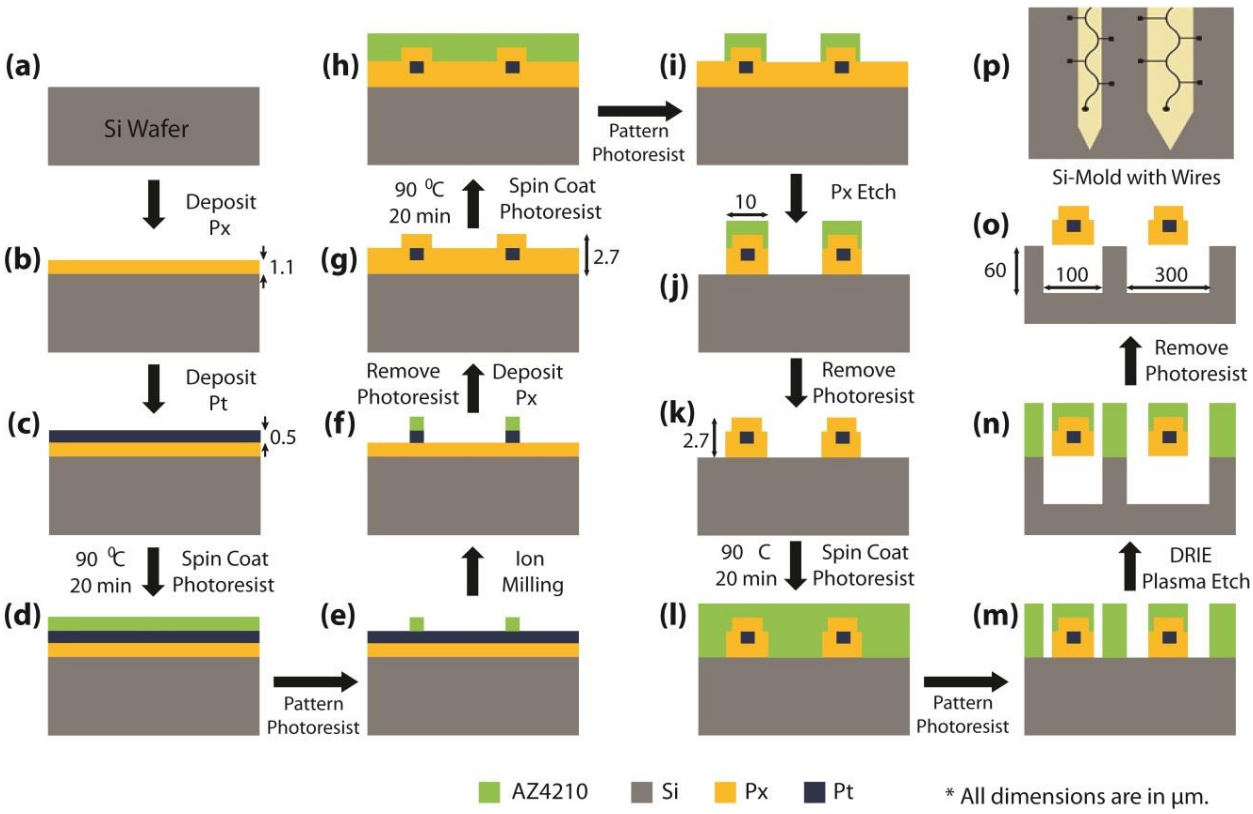

Figure 2.4: The process steps for creating the probe, including the Pt wire and electrode, the Px insulation, as well as the etch pit: **a**. 101.6 mm (4 inch) Si wafer, **b**. 1.1 µm Px layer deposited on the Si wafer; **c** Deposit 0.5 µm Pt layer; **d**. Spin-coat photoresist on top of the Pt layer; **e**. Pattern and develop photo resist for ion milling of Pt; **f**. Ion mill Pt; **g**. Remove photoresist and deposit another layer of 1.1 µm photoresist; **h**. Spin-coat photoresist on top of the Px layer; **i**. Pattern and develop photoresist; j. Etch Px into shape of meandered probe; **k**. Remove photoresist; l. Spin cast another layer of photoresist for DRIE; **m**. Pattern and develop photoresist; **n**. DRIE plasma etch to create etch pit; **o**. Remove photoresist to obtain the Si-mold with probe suspended over etch pit; **p**. Plan view of the Si-mold with probe
* (Dr. Peter J. Gilgunn developed the fabrication process and manufactured Si-molds)

2.1.4 Dissolvable materials for the delivery vehicle

Both the dissolution time/behavior and the mechanical characteristics of the delivery needle depend on the type of dissolvable polymer used for the needle. To demonstrate the fabrication process and its broad material capability, needles are created from carboxymethyl cellulose (CMC, Mw – 90,000 Da, Sigma Aldrich: 419273) and blends of CMC and other sugars, including maltodextrin (dextrose equivalent 16.5-19.5, Sigma Aldrich: 419699), glucose (Sigma

Aldrich: G8270), and sucrose (Sigma Aldrich: S0389). Furthermore, to demonstrate the drug co-delivery capability, CMC needles incorporating an anti-inflammatory drug (Dexamethasone 21-phosphate disodium salt, Sigma Aldrich: D1159) are manufactured.

The dissolvable materials are prepared as hydrogels using the following procedure: Powdered form of the polymer is dissolved in de-ionized water. A 15 wt% solute ratio is used in all material preparations by mixing 1.5 grams of powdered solute with 8.5 grams of deionized water in a glass vial. At this ratio, the prepared materials are in a gel form. The polymers tested in this work included 100% CMC; CMC and 15 wt%, 30 wt%, or 50 wt% maltodextrin; CMC and 15 wt% or 30 wt% glucose; CMC and 15 wt% sucrose, and CMC and 5 wt% or 20 wt% dexamethasone (percentages with respect to total solute amount). When material blends are used, the polymers are mixed in their powdered form before adding the deionized water. After the preparation, the hydrogels are stored at 4°C for 24 h to allow them to homogenize before beginning the molding process.

2.1.5 Fabrication of top mold and needle-mold assembly

A two-part mold is used for molding the dissolvable needles that encapsulate the electrode and wiring. The bottom portion of the mold is composed of the etch pit on the Si wafer with the tethered suspended wires. After fabrication of the top portion of the mold, the two mold portions are assembled together before the spin-casting process that forms the dissolvable needle. The top mold is made from a UV-curable resin (NOA63-2, Norland Products) using a sandwich-molding process, similar to that used in (Zhang et al. 2010). First, a Si master mold is created through DRIE with the same shape and dimensions as the etch pit, as described in the prior section. Additional perforations are created on the edges of the Si mold to support the sandwich molding process.

The master mold is then used to create an elastomer intermediate mold from poly (dimethyl siloxane) (PDMS, Sylgard 184, Dow Corning, 10:1 ratio) with the negative (protruded) shape of the mold, including needle/tab and perforations (see Figure.2.5). Liquid resin is poured on top of this intermediate mold and the mold is placed between two glass slides, which were previously coated with a 20 nm-thick C_4F_8 passivation layer (STS Multiplex ICP RIE). This configuration facilitates removal of the excess resin through the protrusions (from perforations) at the periphery of the elastomer intermediate mold. The same protrusions also support the mold for prescribing the top-mold thickness. The sandwich assembly is then placed under a UV lamp (365 nm for 15 min), allowing the resin to cure. The cured resin top mold, which now includes through features with the shape of the needle/tap, is then demolded.

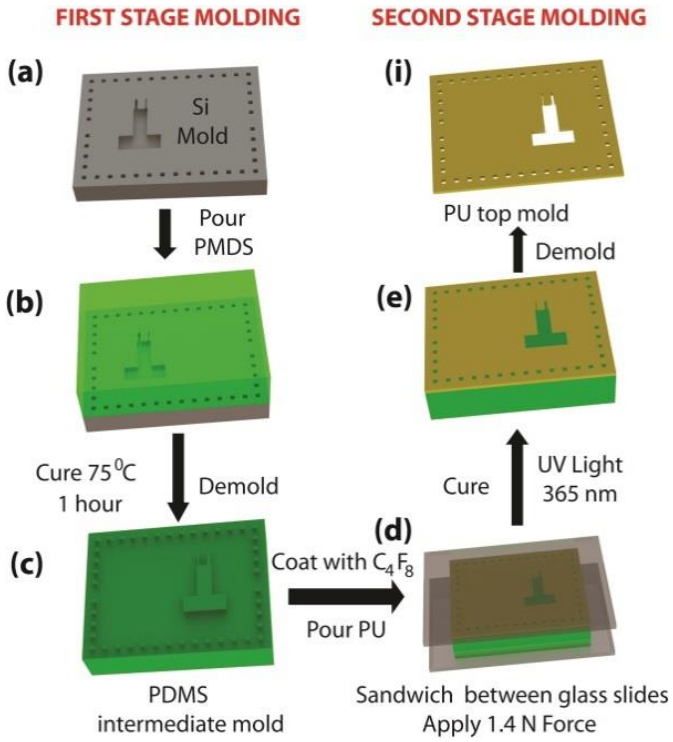

Figure 2.5: Fabrication of the top mold by the sandwich-molding process: **a.** The Si master mold fabricated via the Bosch process; **b.** Mix PDMS (10:1 ratio), de-gas and pour over the Si-master mold; **c.** Cure at 75° C for 1 h and then demold from the master mold; **d**. Pour the UV curable resin over intermediate PDMS mold and sandwich between glass slides to squeeze out excess resin; **e.** Cure using UV light (365 nm) for 15 min and remove glass slides; **f.** Demold resin from PDMS mold to obtain the top mold.

The next step is to assemble the resin top mold with the Si bottom mold that includes the wiring, the electrode, and the etch pit, into a single assembled mold. The resin mold is first trimmed along the edges to remove the peripheral protrusions. The remaining resin top mold is then aligned with the Si bottom mold using a device bonder (Laurier M9A). During the alignment procedure, the edges of the needle shapes are utilized via the use of two high resolution cameras. A 10 N force is applied for 1 min after the alignment to complete the adherence of two layers of the assembled mold.

2.1.6 Molding of the dissolvable needle through spin casting

A solvent-based spin-casting process, previously described in [75], is used to create the biodissolvable delivery vehicles. Briefly, an amount of prepared hydrogel is loaded onto the mold, and the mold is placed inside of the buckets of a centrifuge. This step is followed by centrifuging at prescribed speed and temperature for a period of time to provide both the required force to completely fill the mold shapes, and the air circulation to evaporate the solvent to create the final needles.

An analysis of the spin-casting process is completed to determine the time required for solvent evaporation to reach the desired steady-state material properties for the dissolvable polymers. For this purpose, CMC-only and CMC-15% glucose materials were studied. Materials are prepared as described above with the specific solute ratios. For each material, 10 PDMS molds with targeted final rectangular size of 22 mm by 15 mm by 2 mm were fabricated. 600 mg of the prepared hydrogels were loaded into each mold, and the loaded molds were carefully weighted (Intell Lab^{TM} PM-100) with 1 mg resolution. The loaded molds were then placed into the buckets of the centrifuge (Heraus Multifuge X3R with Swinging Bucket Rotor TX 750). The centrifuge speed was set to 4700 rpm, and the centrifuge temperature was set to 5°C. The room humidity

level was controlled with a humidifier/de-humidifier combination at 40%. The spin-casting process is then commenced, and the weight of each mold is measured in 30 min intervals until a steady-state weight is reached. Another set of points were then measured after 5 h of additional centrifuging to ensure that the steady-state was reached.

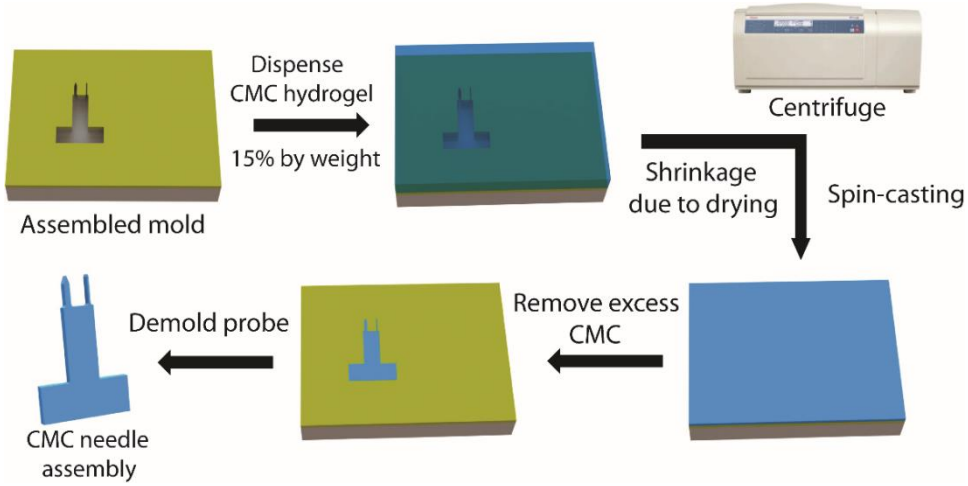

Figure 2.6: Fabrication of CMC needles with encapsulated Px-Pt probe via spin casting in centrifuge at 4700 rpm at 5°C for 10 h.

To fabricate needles that encapsulate the Px-Pt probe, the assembled mold is then placed in a bucket of the centrifuge. Figure. 2.6 shows the steps of the spin casting process. 600 µl of the prepared hydrogel of the dissolvable material of choice is then dispensed over the assembled mold using a syringe. The centrifuge is then rotated at 4700 rpm at 5°C. The duration of spin casting is determined through the analysis described in the previous paragraph. During the casting process, the water in the hydrogel evaporates. The solute that remains becomes a solid polymer matrix that takes the shape of the cavity in the mold and encapsulates the meandered wires. The excess polymer that covers over the needles is removed using a sharp blade (X-ACTO #17) after lightly hydrating the exposed portion of the needle. The hard resin top mold enables limiting the removal of the excess polymer. Any additional moisture introduced during hydration is then removed by centrifuging an additional 30 min using the same conditions as described

above. The fabricated polymer delivery needle assembly is then detached from the mold using tweezers.

2.1.7 Geometric characterization of the fabricated needles

To evaluate the reproducibility of the needles fabricated through the presented spin-casting approach, fabricated needle geometries are statistically characterized for their length, width, and thickness. To measure needle geometries, 80 needles with nominally identical geometries (40 needles each, 100 μm and 300 μm width, with nominal mold dimensions of 1.65 mm length, 135 μm thickness, 40° tip angle, and 0° relief angle) were fabricated. An optical microscope with 10X objective (Carl Zeiss, Axiovert 200, with 1.16 μm/pixel resolution when using the 10X objective) is used with a calibration grating to obtain needle thickness from the side view of the needles. The microscope images were analyzed using the MATLAB image processing toolbox to determine the thicknesses. To characterize the width and the length of the needles, an environmental scanning electron microscope (Quanta 600 FEG) is used obtain high resolution images of each needle, and the obtained images are processed using the MATLAB image processing toolbox. The width and thickness are defined as the mean distance between the edges along the length of the probe, whereas the length is defined as the maximum distance from the tip of the probe to the base of the handling tab. The mean and standard deviation values are obtained from these measurements and compared to their targeted values to check for repeatability.

2.1.8 Mechanical characterization of the dissolvable needle materials

To determine mechanical properties of the dissolvable polymer blends used in this work, bulk polymer sheets (20 mm by 20 mm by 3 mm) are fabricated using the same spin-casting protocol as that used for the needle fabrication. Small tensile (dog-bone) specimens, with a gage length of

10 mm, a gage width of 1 mm, and a thickness of 0.7 mm, are then created from each sheet using mechanical micromilling on a high-precision miniature machine tool. A tensile testing machine (Instron 5490, single-column, 500 N load cell) is then used to determine the Young's modulus, yield stress, ultimate tensile stress, and toughness of each dissolvable polymer blend. The strain rate during the testing is set to 1 mm/min.

To assess the absorption of moisture from the environment, and to determine associated changes in mechanical properties, an additional set of tests is performed. First, the amount of moisture absorption from ambient is characterized. To this end, 10 CMC needles are fabricated. They are then kept in a 120°C oven (Lindberg/Blue M) for 30 min to remove the majority of the remaining moisture after fabrication: For the purpose of this study, the needles are considered to be moisture-free after the completion of the heating process. Subsequently, the needles are exposed to room environment, with ambient conditions of 27°C temperature and 40% humidity. At every 15 min post heating and up to 480 min, the needles are weighed on a 10 μg-resolution scale (Satrorious LE26P micro balance), where the increase in needle weight is considered to be the amount of moisture absorbed by the needles. Another data point is obtained after 2880 min (2 days) to confirm the steady-state absorption level.

To determine the changes in material properties with increasing moisture content, dog-bone shaped samples are prepared from CMC (as described above). Mechanical properties of the material are obtained through tensile tests immediately at the completion of the heat treatment and after 2880 min exposure to ambient, using four samples for each case. 22.5 min of ambient exposure is considered to be a good representation of that experienced during the functional (*in vivo*) implementation of the needles after removal of the needles from hermetic packaging. Another 30 dog-bone samples are tested after exposure to ambient such that the concentration of dog bone samples is same as that of needles at 22.5 min.

2.1.9 The insertion device

Precise placement of the micro-scale probes to the targeted locations within the brain is important for measuring desired signals from a single neuron or a cluster of neurons. Furthermore, the dissolvable needles must be inserted rapidly in a single try to ensure that their tip do not start dissolving and becomes blunt. To address this need, we designed and constructed an automated insertion device, as depicted in Figure 2.7. The device consists of a closed-loop controlled piezoelectric drive (M272.20 from Physics Instrumente, A.G.) that drives a piston with up to 200 mm/s speed within a total of 50 mm travel length, and a custom-made pneumatic chuck that enables holding the insertion needles from their tabs. The insertion device is attached to a standard stereotactic frame.

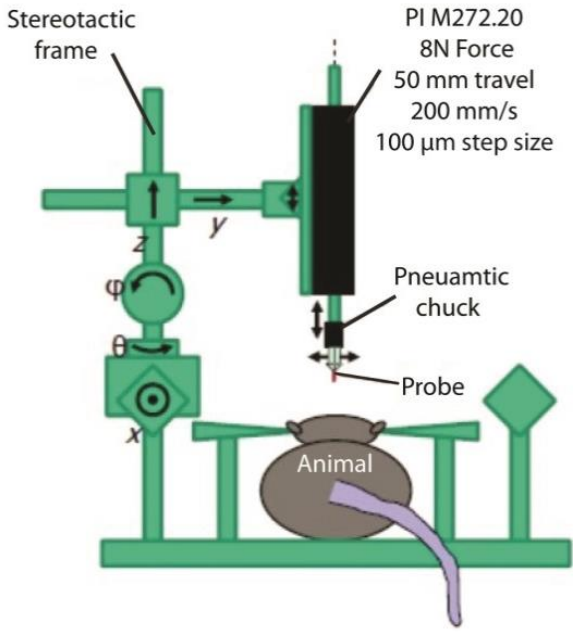

Figure 2.7: Schematic of an automated insertion device mounted on a stereotaxic frame for inserting dissolvable needles into rat brain at prescribed velocity and high positional accuracy. (*Dr. Peter J. Gilgunn designed the insertion device)

The insertion procedure begins with the use of a non-dissolvable poly(methyl methacrylate) (PMMA) reference probe that has the same dimensions as the dissolvable insertion needles,

except with a blunt semi-circular tip to prevent insertion into brain. First, the reference probe is attached to the pneumatic chuck, and lowered down to the brain surface in 10 μm steps. A digital microscope allows determination of the contact with the brain with 10 μm resolution. The contact height is then noted as the position of the brain surface, and the device is retracted from the brain surface. The PMMA needle is then replaced with the dissolvable insertion needles (with the embedded probes). Subsequently, 80 mm/s insertion speed is used to insert the needle to the desired depth. Once the insertion is completed, the chuck is then opened up to release the needle.

2.1.10 Insertion studies on cadaveric brain tissue and agarose gel

To demonstrate the capability of dissolvable needles in penetrating into tissue without failure and to evaluate the progression of their dissolution *in vitro*, dual-shank needle assemblies are inserted into bovine cadaver brain tissue and into agarose gel. Three samples of 20 mm by 20 mm sections of cadaveric brain tissue are prepared and held in a plastic container. The tissue samples are kept in 1X phosphate buffered solution (PBS) with 7.4 pH at 37 °C before the needle insertion. The dura is not removed, and the needles are inserted through the dura. To increase the optical contrast between the tissue material and the needle traces, a dye (India ink, Fisher Scientific: NC9903975) is mixed with CMC when preparing the needles. The needle insertions are performed using the insertion device and the associated procedure. One minute after inserting the dual-shank needles into each sample, the tissue sample is frozen using liquid nitrogen. The frozen samples are sectioned using a microtome to demonstrate that the needles penetrate deep into the tissue. Each section is 50 μm thick, and the sectioning is continued to a depth of 700 μm.

To further observe the progression of dissolution of the needles, CMC-15% glucose needles that encapsulate the Pt-Px probes are inserted in agarose gel using the insertion device. To mimic the mechanical properties of the brain tissue (Chen et al. 2004; Casanova et al. 2014), a

0.6% (wt/wt) agarose gel (Sigma Aldrich: A9539) with PBS 1X with 7.4 pH solution is prepared in PMMA containers. The process of insertion and dissolution are recorded from the side (perpendicular to the insertion axis) using a digital camera (Thorlabs: dcc1654c) with a 12X tube lens (Navitar: 1-50487). The agarose set-up allows the microscope to capture the entire length of the probe, which is essential to visualize the dissolution of the polymer matrix that encapsulates the meandered wires.

2.2 Results and Discussion

2.2.1 Probe stiffness and comparative analysis of probe-tissue interaction

One of the leading causes of chronic failure of neural probes is believed to be the glial scar that forms around the electrodes. An important driver of the glial scarring is understood to be the strain arising from the micromotion, that is, the relative motion between the brain tissue and the probe [29]. To demonstrate the reduction of strains in the tissue-probe interface realized by the presented ultra-miniature ultra-compliant probes as compared to those experienced with stiff probes, a finite-element analysis is performed. The ultra-compliant probes are compared to stiff Si probes. Each probe is embedded in the brain tissue to a depth of 1.5 mm from the tissue surface.

Table 2.1: Stiffness comparison between the Pt-Px and the Si probes.

Direction	**Si Probe (μN/μm)**	**Px-Pt Probe (μN/μm)**
x	1.2×10^{5}	1.4×10^{-2}
y	98.5	2.6×10^{-5}
z	3.7	1.8×10^{-6}

First, we calculated the stiffness of the meandered Px-Pt probes and compare it to that of the stiff Si probe. In each case, the left-end of the probes is fixed, and a total probe length of 3 mm is used. Table 2.1 lists the resulting stiffness values in each of the three directions. This result indicates that the Pt-Px probe is significantly more compliant (6 orders of magnitude or more in all directions) than the Si probe.

Second, a static analysis is performed, where an axial displacement of 30 μm (away from the brain surface) is applied to the fixed end of each probe while keeping all the boundary coordinates of the tissue model fixed. Figure.2.8a and 8b show the displacements and strains for each case. As expected, the entire Si probe is displaced by 30 μm. Since all the coordinates between the probe and the tissue are fixed (no-slip condition) in this model, the tissue experiences considerable local displacement. On the other hand, the displacements of the meandered probe are substantially smaller. This is due to the fact that the majority of 30 μm deflection is accommodated by the flexural displacement of the meandered wiring between the tissue surface and the skull. The displacement values of the electrodes (at the tip of the probe) are 30 μm for the Si probe and 0.2 μm for the ultra-compliant probe. The strain map in the vicinity of the electrodes indicates the same pattern: the maximum strain in the vicinity of the electrode is 37% for the stiff Si probe, as compared to 0.3% for the ultra-compliant probe. The maximum strain for the stiff probe occurs at its tip, whereas for ultra-compliant probe, the maximum strain of 8.4% occurs at the entry point into the brain rather than in the vicinity of the electrode. Thus, micromotion leading to glial scarring is expected to be minimized or eliminated at the electrode region. One comparative metric between the stiff and ultra-compliant probe is the total volume of tissue that experiences strain above a given limit, e.g., 3%. This metric is five orders of magnitude higher for the stiff Si probe compared to the ultra-compliant probe. The meandered geometry is the main reason for this significant improvement in axial response for

static displacements. A similar analysis with application of lateral displacement indicates similar benefits in using the ultra-compliant probe.

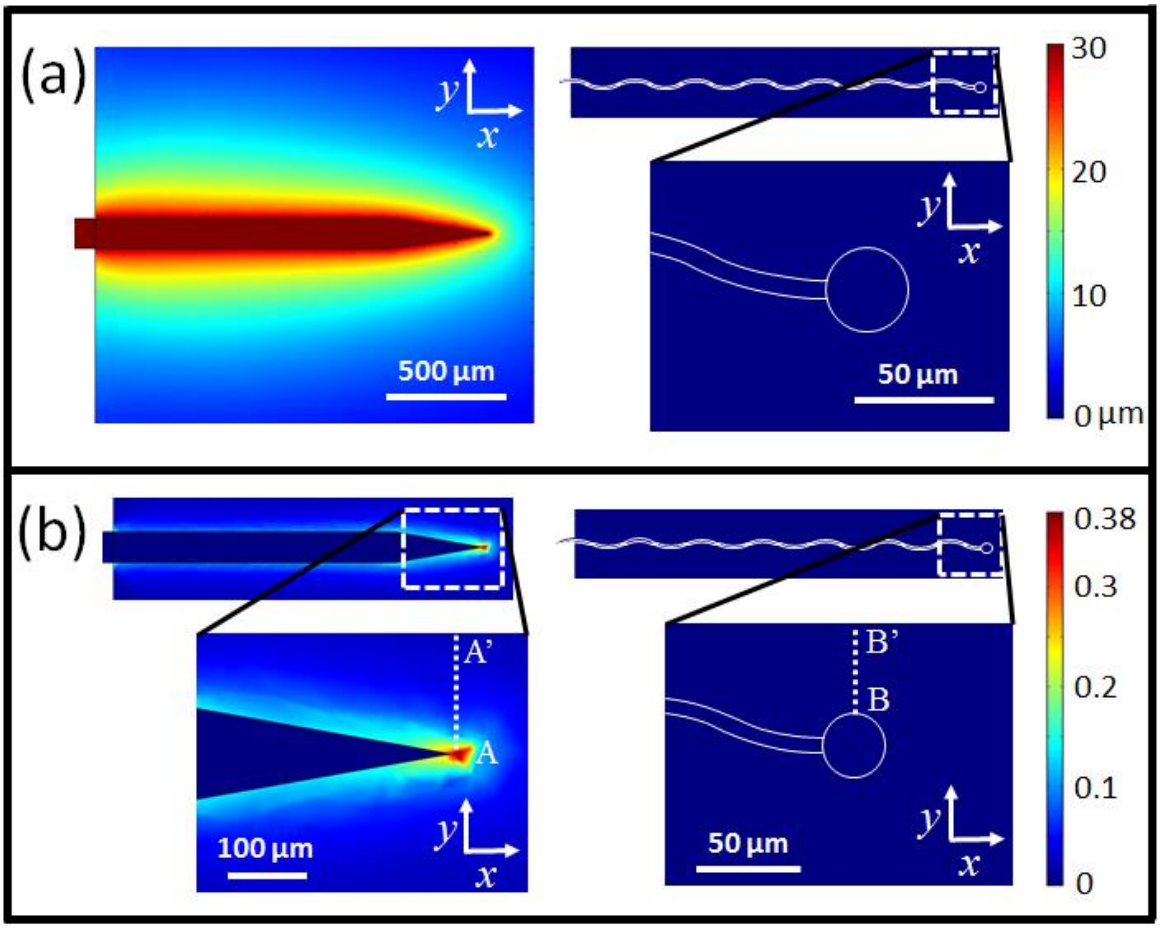

Figure 2.8: Finite-element analysis of the probe: **a**. Displacement profile within tissue when the probe is moved by 30 µm away from tissue. Displacement fields are much higher in case of Si-probe due to high stiffness as compared to meandered probe **b.** Comparison of the von Mises strain field between the Si probe and the meandered probe. AA' and BB' represent the radial distance from electrode sites along the *y*-axis that are used in Figure. 2.10. The boundary of the meandered probe is outlined in white for contrast.

Third, a dynamic analysis is conducted, where the brain tissue is oscillated in the axial (*x*) or one of the two lateral (*y* and *z*) directions. Considering the micromotion of brain [29], a sinusoidal motion with 30 µm amplitude and 1.2 Hz frequency is imposed by uniformly moving all the boundary coordinates of the tissue section. Figure. 2.9a, 9b, and 9c show the von Misses strain distributions in the vicinity of the electrodes for the each of the three cases. The values of maximum strain and of tissue volume with more than 3% strain are given in Table 2. The

maximum strain in the vicinity of the electrode is at least an order of magnitude lower for the ultra-compliant probe than for the stiff Si probe. Similarly, the maximum strain in the tissue is significantly lower when the ultra-compliant probe is used. The largest strain is experienced when the direction of micromotion is aligned with the axis of the probe (i.e., in *x*). Although the maximum strain in the vicinity of the electrode are in the same order of magnitude for the stiff probe, for the ultra-compliant probe, they are dramatically smaller for the lateral micromotion than for the axial micromotion, as expected as the lateral stiffness of the ultra-compliant probe is much lower than its axial stiffness. For the ultra-compliant probe, the maximum strain always occurs at the surface of the brain, whereas for the stiff probe, it occurs at the tip, i.e., where the electrode is located. For all directions of micromotion, the tissue volume with greater than 3% strain is more than five orders of magnitude smaller for the ultra-compliant probes.

Table 2.2: Comparison of dynamic effects of micromotion between the stiff Si probe and ultra-compliant Px-Pt probe in brain tissue.

Micromotion Direction	**Volume Affected ≥ 3% strain (μm^3)**		**Max. Strain at Electrode (%)**		**Max Strain in the Tissue (%)**	
	Si Probe	Px-Pt Probe	Si Probe	Px-Pt Probe	Si Probe	Px-Pt Probe
x	1.13×10^8	631	40	4.5	40	6.5
y	2.0×10^8	5.46	31.3	0.03	31.3	4
z	8.2×10^7	0	16.1	0.001	17.2	1.2

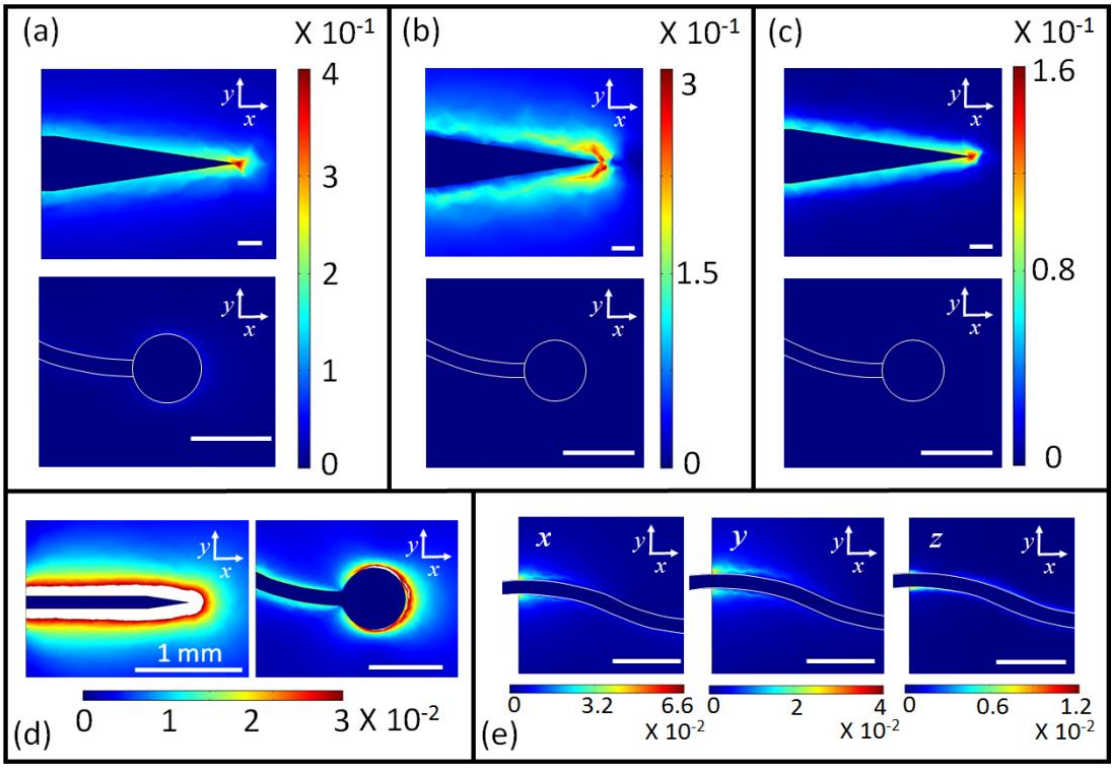

Figure 2.9: Comparison of von Mises strain profile within tissue near electrode site at maximum amplitude of 30 µm at 1.2 Hz for: **a.** Excitation along the *x*-axis (axial); b. Excitation along the *y*-axis (lateral); **c.** Excitation along the *z*-axis (lateral); **d.** Comparison of region with tissue (white color) having more than 3% in the tissue for axial excitation on *x*-*y* cross section; **e** Maximum strain (at the brain surface) for the meandered probe with excitation axis indicated. The boundary of meandered probe is outlined in white for contrast (Scale: 50 µm).

To provide another perspective to the strain distributions, Figures 2.10a and 10b show changes in von mises strain within the tissue along the positive *y* direction (as shown by lines AA' and BB' in Figure. 2.8b) up to 100 µm away from the electrode for static and dynamic cases, respectively, for each of the two probes. For a given location (distance), the strain is calculated by averaging over a 2 µm x 2 µm area around that point in the *x*-*y* plane. The plots indicate that for the static case, the strain for meandered probe is at least two orders of magnitude lower than that for the Si probe. Similarly, for the dynamic case, the strain for the meandered probe is at least an order of magnitude lower than that for the Si probe.

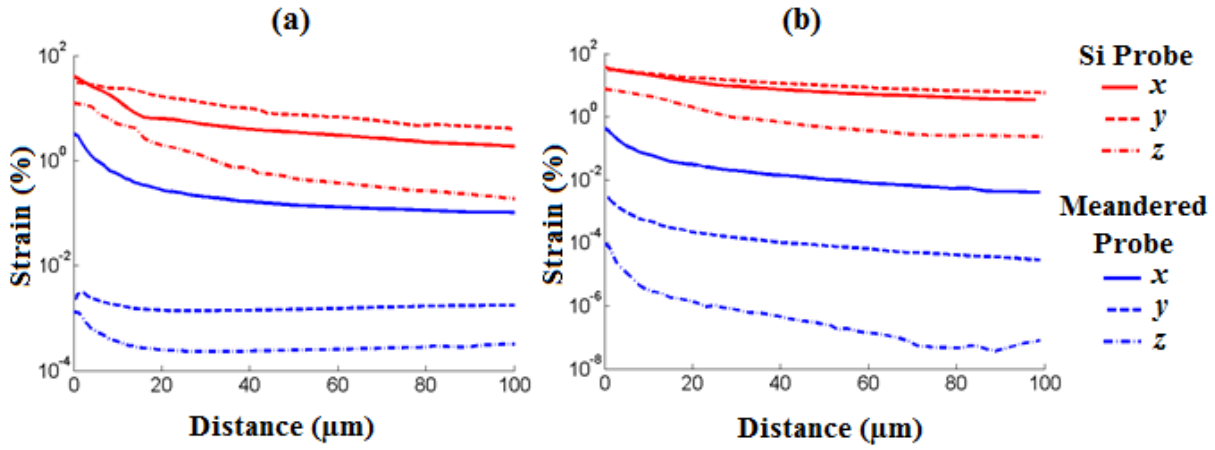

Figure 2.10: Comparison of von Mises strain profile within tissue along the *y* direction at the electrode site (the origin indicates the electrode surface) **a.** Strain distribution for the static case, where a displacement of 30 µm applied along the *x*, *y* or *z*-axis; **b.** Strain distribution for the dynamic case, where a base excitation of 30 µm amplitude at 1.2 Hz is applied along the *x*, *y* or *z*-axis. *X*, *Y* and *Z* indicate the imposed displacement or excitation direction.

2.2.2 Fabricated probes and insertion needles

Probe design

Images of a fabricated dual probe, while still on the Si wafer, are given in Figure 2.11. Figure 2.11a shows the plan view of the entire probe, including the handling tab and the connector wires. Figure 2.11b and 2.11c show magnified SEM images of the probes on the Si wafer, where the output cable (on the handling tab portion), Pt electrode, meandered wiring within the needle portion and the Px tethers are all visible. The etch pit is later used as the bottom mold during fabrication of the insertion needle. The Px tethers are designed to suspend the wiring and the electrode on top of the etch pit until the completion of the molding process. The circular electrode is recessed from the tip by 150 µm to prevent damage to the electrode during insertion. The output cables include 4-channel stress-relieved Pt cables with Px insulation.

Many works in the literature suggest that probes with high compliance (approaching that of the cortical tissue) significantly reduce foreign body response. Towards minimizing the

mechanical mismatch between the cortical tissue and the probes, the probes are designed with micron-scale wiring (2.7 μm x 10 μm cross section), including a 500 nm thick Pt core and the surrounding parylene-C insulation layer.

Although smaller cross-section and parylene-C construction increases the lateral (bending) compliance of the probes, for a straight probe, the tethering forces (and associated displacements) along the axial direction of the probe would transfer directly to the electrode. As such, considerable strains on tissue/electrode interface would be experienced due to tethering forces and micromotion, thereby causing sustained damage to the surrounding tissue. In order to minimize the interfacial strains between the electrode and the tissue, the probes presented here feature meandered wiring, resulting in significant increase in effective axial compliance of the probes. Our design and fabrication approach provide capability to select the meander parameters. For this work, meandered wiring is created by joining piecewise circular arcs.

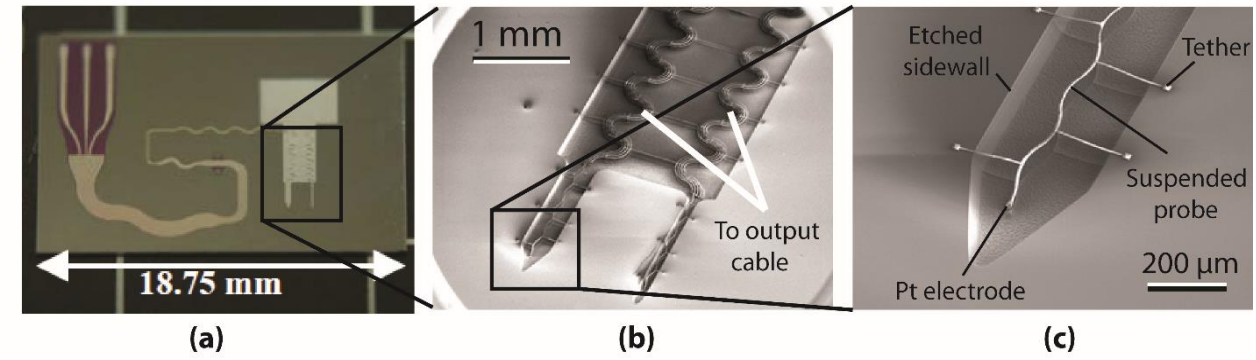

Figure 2.11: Fabrication of the probes: **a** Si bottom mold with suspended dual-shank probe, etch pit and output cables; **b** A SEM image showing the mold of the one wide and one narrow needle with suspended probes; **c** A SEM image of the meandered probe suspended over the wide (300 μm) needle etch pit showing Px tethers and the Pt electrode at the tip**.**

Based on the literature, reduced reactive tissue response is experienced when the electrode dimension is commensurate with that of the neurons [42]. However, a sufficiently large electrode site size is required to ensure low enough impedances such that the action potentials can be

measured with high signal-to-noise ratio. To strike a balance between these two needs, the disk-shaped electrode is designed to have a 26 μm diameter, with a 20 μm circular section of exposed Pt and surrounding Px insulation. Although one electrode is demonstrated per each needle, multiple electrodes at different locations with the same or independent wiring can be designed in these size needle pits.

Dissolvable insertion needle

An ideal insertion needle is of minimum volume and dimensions that will enable failure free penetration and precise positioning of the probe and is made from a material that dissolves in a very short period of time without any harmful by-product that could cause tissue damage. The molding approach described here enables creating probes with optimal geometries to strike a balance between strength and material amount. As a demonstrative example, dual insertion needles (following the dual-probe design) are fabricated on a single handling tab using the spin-casting based fabrication process. Both needles are designed to be $l_n = 1.65$ mm long and $t_n = 135$ μm thick, with a $\theta_t = 40^o$ tip angle, $r_f = 150$ μm fillet radius, and $\theta_r = 0^o$ relief angle. The widths of the small and large needles are 100 μm and 300 μm, respectively, which are chosen to evaluate different needle dimensions, as well as to enable direct comparison to the state-of-the-art commercial microwire probes (AM System, Carlsborg, WA). Furthermore, to demonstrate the capability of fabricating different needle and array designs, we created three- and five-needle needle arrays, including varying needle width (from 100 μm to 300 μm) and needle lengths (from 1.4 to 2.8 mm).

Figures 2.12a-12d show ESEM images of sample needles fabricated using the spin-casting approach (without the embedded electrodes) from different dissolvable materials, including CMC, CMC-15% glucose, CMC-15% sucrose, CMC-15% maltodextrin. As seen in these

Figures, dual-probe needles are successfully fabricated, each dual-probe including a 100 μm- and a 300 μm-wide needle, both attached to a single handling tab. The versatile needle-fabrication process described here (the spin-casting based micromolding approach) enables fabrication of needles and needle arrays with varying, complex geometries, and thus, can facilitate optimization of the insertion vehicle designs. It is noted here that the authors have already demonstrated the viability of narrow CMC needles (100 μm) to dissolve in brain tissue *in vivo* over a period of 12 weeks [63]. Early time points from histology showed that CMC needles absorb moisture and expand after insertion. Later time points (4 weeks) showed closure of wound and neuronal cell bodies within the original needle tract. At 12 weeks, activated microglia was absent and neural regeneration was observed at the implant site.

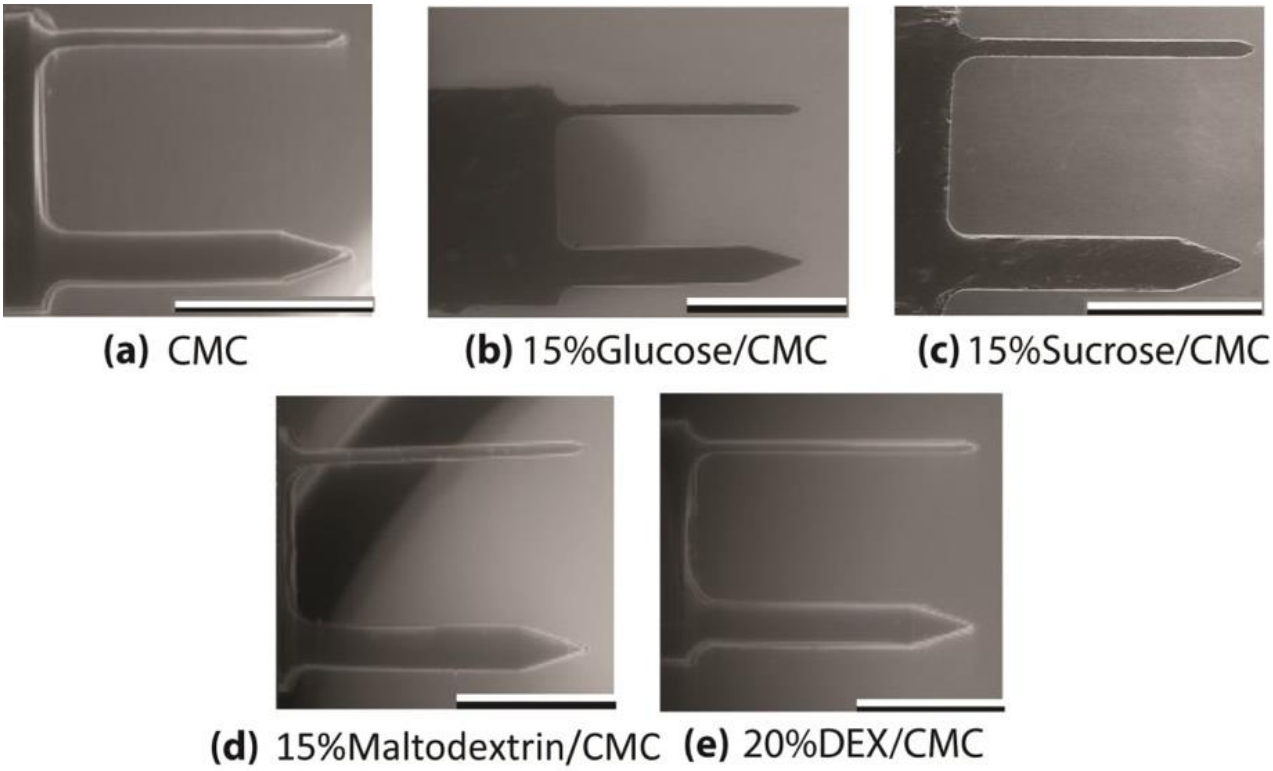

Figure 2.12: ESEM images: **a** CMC; **b** CMC-15% Glucose; **c** CMC-15% Sucrose; **d** CMC-15% Maltodextrin; e CMC-20% DEX (Scale: 1 mm).

The dissolvable needles can also be used as a platform to co-deliver drugs or biologics, such as drugs to subside inflammation or enhance neural regeneration [76]. To demonstrate this capability, needles with dexamethasone (DEX) as a sample anti-inflammatory drug were created: Figure 2.12e shows a sample dual-shank needle made from CMC-20% DEX. In other works, dissolvable materials are used to deliver small molecules, large molecules, as well as viral vectors to living tissue *ex vivo* and *in vivo* using microneedle arrays fabricated through spin-casting [77,78]. One important benefit of this approach is that the entire process is conducted at the room temperature, thus allowing maintaining bioactivity.

The presented approach further enables creating 2D arrays of needle-encased probes. If desired, each probe in a 2D array can have a different design. Figure. 2.13 shows sample CMC needles in three- and five-array configurations with different widths and lengths.

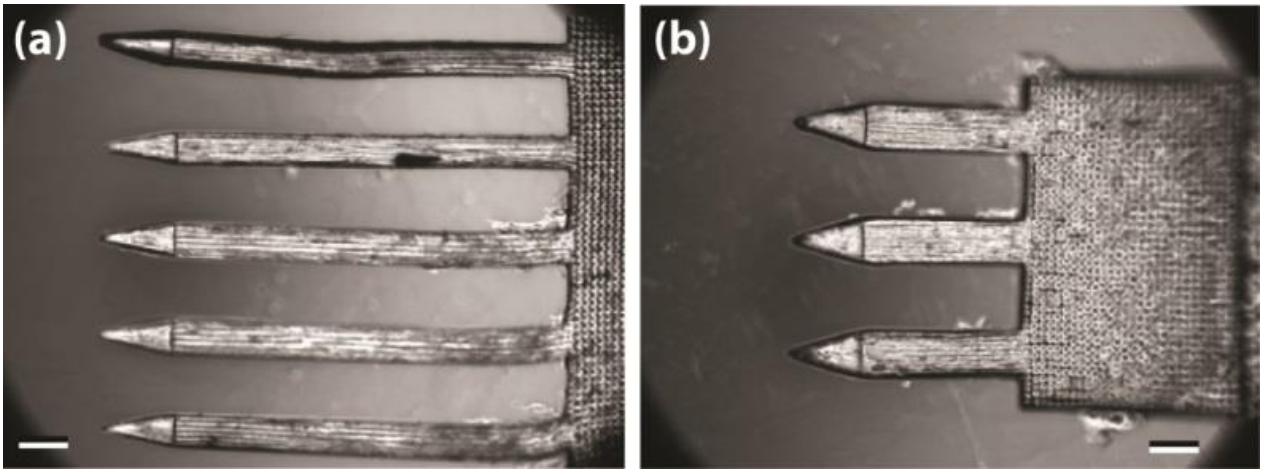

Figure 2.13: Geometric flexibility of spin casting: **a**. 5 shank array (length: 2.8 mm, width: 200 μm) **b**. 3 shank array (length: 1.4mm, width: 300 μm) (Scale: 300 μm).

Integrated probe and insertion needle

A sample dual-shank probe encased in the dissolvable delivery needle is shown in Figure 2.14. Figure 2.14b shows nano-CT images (Xradia UltraXRM-L200) of the needles, where the Pt wiring and the electrode can be seen inside the dissolvable material.

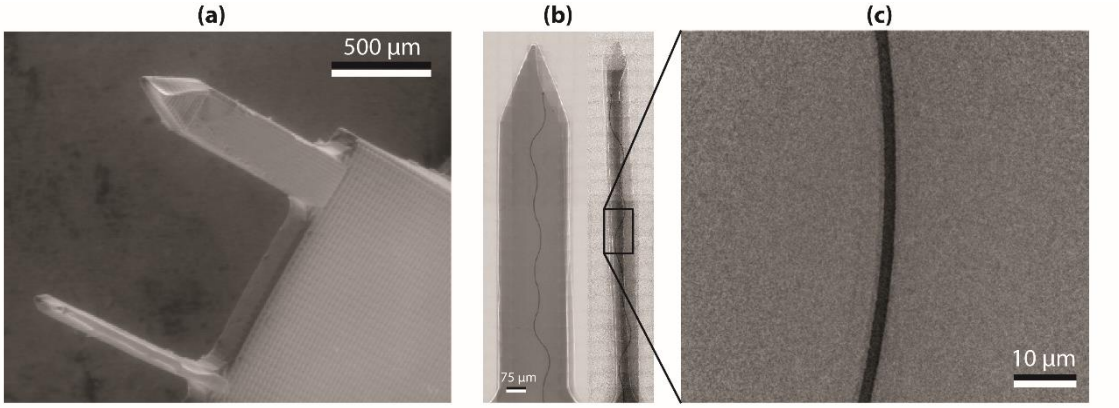

Figure 2.14: ESEM images: **a**. An ESEM image of CMC dual-shank needle; **b**. Nano CT image of wide and narrow needle showing the Pt wire and CMC matrix. The electrode is at the tip of the Pt wire; **c** Zoomed in Nano CT image showing the Pt wire within CMC polymer matrix**.**

A unique advantage of the approach presented in this work is that both the geometries and material selections for the probe and the needle are decoupled, thereby enabling optimization of each without limitations imposed by the other. This facilitates designing insertion needles with advantageous geometric features, as well as minimizing needle volume and increasing the needle strength through design. For instance, we included fillets where the needles merge with the handling tab to considerably increase the factor-of-safety against needle failure during insertion. Similarly, the tip region is tapered at a desired angle to minimize penetration forces while providing tip strength during penetration (Bjornnson et al. 2006). The handling tab is also designed to facilitate handling during fabrication process and attachment of the needle to the insertion device for precise application of the probes. The process allows each of these needle geometry parameters to be fully controllable.

2.2.3 Needle fabrication and evaluation

Spin-casting process

During solvent-based spin casting, a critical parameter is the time it takes for the completion of the molding process, i.e., the centrifuging time. This is the amount of time for the initial

hydrogel to form into a solid needle with the desired shape and minimal moisture content. This amount of time depends on the material type, initial solute concentration, initial loading volume, centrifuging parameters (speed, temperature), humidity and temperature of the fabrication environment, as well as the mold shape. Although a comprehensive study of all those parameters are beyond the scope of the current work, a sample analysis of centrifuging time for two materials (CMC and CMC-15% glucose) is presented here, while keeping all the other parameters constant.

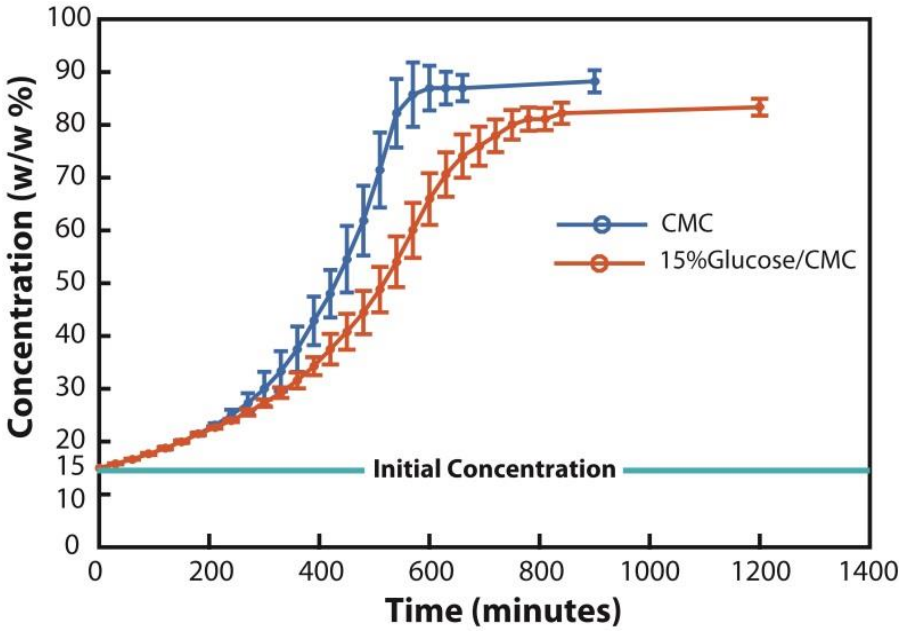

Figure 2.15: Solvent evaporation of CMC and Glucose/CMC concentration.

Figure 2.15 shows the change in solute concentration when centrifuging sheets of CMC and CMC-15% glucose blend. The solute concentration is calculated as $R = m_s/M_c$, where m_s is the mass of the solute (15% of 0.6 grams, which is equal to 90 mg) and M_c is the measured weight at each time point t. Initially, $M_c = M_i$, the initial total weight of the hydrogel (600 mg). As such, at time zero, the concentration begins at 15%, which is the initial solute concentration of the hydrogels. The error bars indicate one standard deviation (±σ) from the average for 10 different molds at each time point. It is seen that the initial drying rate of CMC and CMC-15% glucose

blend is similar up to about 240 min. Above 25% concentration, water is evaporated from CMC faster than that from CMC-15% glucose blend. The concentrations for the pure CMC and for CMC-15% glucose blend reach a steady state at approximately 10 h and 13 h, respectively. At steady-state, CMC has a concentration of 88%, and the CMC-15% glucose blend has a concentration of 82%. The steady-state solute concentration is strongly dependent upon the dissolvable material and the other parameters, especially the humidity and temperature of the centrifuge and the laboratory environment.

Reproducibility and accuracy of needle geometries

When the solvent-based spin-casting approach is used, the volume of material reduces considerably from its hydrogel form to its final solid form due to the evaporation of the solvent. As a result, the final part is generally smaller than the mold cavity. However, the shrinkage is generally repeatable for a given set of process parameters and mold geometry, and thus, mold designs can be modified to obtain desired needle dimensions reproducibly.

To determine the geometric accuracy and reproducibility of needle geometries, a study is performed. The length, thickness, and width of 40 pairs of CMC needles are measured. Table 3 provides the average values and standard deviations for each of the measured parameters for both the narrow and the wide needles. The width (w_t), thickness (t_t) and length (l_t) of the mold cavity and those of the fabricated needles ($w_n, t_n,$ and $l_n,$ respectively) are given. The variations in width are larger for the narrow needles (~5.5% of the average) as opposed to that for the wide needles (~1.7% of the average). In the thickness dimension, both the wide and narrow needles show similar variations, reaching up to 7%. On the other hand, the variations in the length dimensions are below 2%. The difference between the mold dimensions and the measured value for each parameter includes both the effect of process uncertainty and the shrinkage arising from

the solvent-based molding approach. The width values larger than the mold dimensions are seen in some cases due to the variations on the resin top-mold dimensions. The squeegee step also contributes significantly to the uncertainty of the thickness dimension. Nevertheless, it is seen that the needles can be obtained with a sufficient level of precision for both narrow and wide needles.

Table 2.3: Needle-geometry parameters of the molds and from the fabricated needles.

	w_t (µm)	w_n (µm)	t_t (µm)	t_n (µm)	l_t (µm)	l_n (µm)
Narrow CMC needle	100	98.7±5.2	135	143.6±9.3	1650	1,547.9±19.0
Wide CMC needle	300	293.1±4.2	135	136.4±7.9	1650	1,533.2±12.2

2.2.4 Mechanical property of needle materials

The dissolvable insertion needles are required to penetrate the tissue without failure and reach the desired depth precisely without considerable deflection. However, the size and material amount of the needle should be minimized to ensure rapid dissolution and to minimize immune reaction. To satisfy these competing needs—of stiff, high strength needles yet with small size—the properties of dissolvable needle materials must be determined. We performed a set of tensile tests to obtain elastic modulus, ultimate tensile strength, and maximum strain of various needle materials used in this work.

A critical point to consider here is that the dissolvable materials readily absorb moisture from air when exposed to the room environment. Water absorption depends on the material, relative humidity of the environment, time of exposure, as well as the needle geometry (commonly, to the surface area per volume). Importantly, the water content of the needle materials strongly affects their mechanical properties.

As an example, for water absorption of needle materials, Figure. 2.16 shows the change in water content of CMC needles when exposed to the room environment (27 °C and 40% humidity). The needles are taken out of the oven (after heating to complete the drying after centrifuging) at time $t = 0$. It is seen that there is a rapid moisture absorption, which reduces the concentration of the needles in an exponential manner. Interestingly, the steady-state value of 87% concentration is very similar to that obtained at the steady-state of the spin casting process (88%).

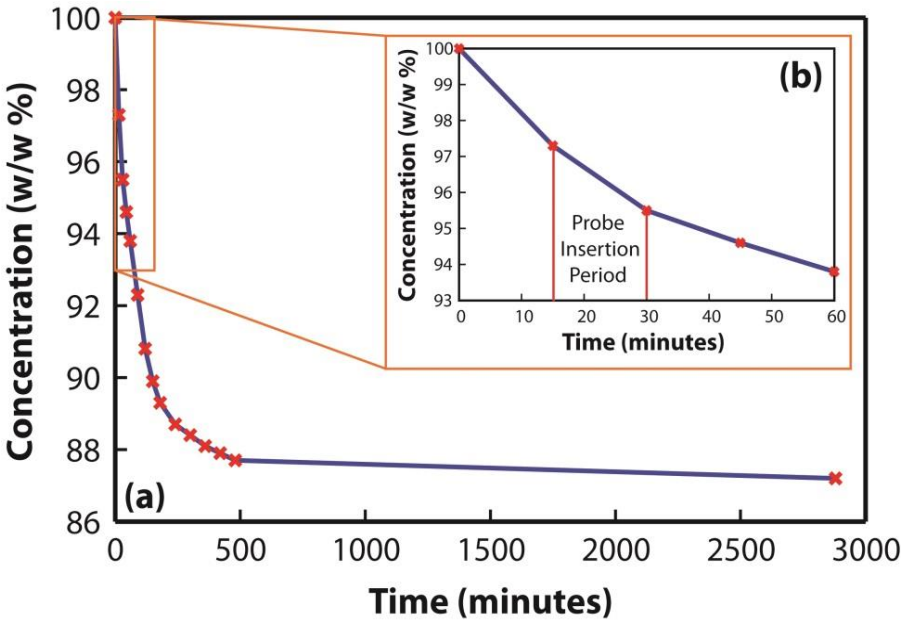

Figure 2.16: Change in water content of CMC needles when exposed to the room environment: **a.** Concentration of CMC probe in ambient conditions at different time points post sterilization at 120 °C. CMC absorbs water after it is exposed to ambient environment; **b.** Concentration of CMC probe during the first 60 min post sterilization.

To determine the effect of moisture content on mechanical properties, the CMC specimens are tested at three concentration levels, including 100% (fully dry), 87% (steady-state) and 96.5% (implementation). Considering the insertion procedures for *in vivo* application, the time from removing the needles from hermetic packaging to the completion of the needle insertion to cortical tissue is assumed to be between 15 to 30 min, or 22.5 min on average. At that time point,

the concentration of CMC is approximately 96.5%. The mechanical properties of the CMC tensile specimens are measured at 100%, 87%, and 96.5% concentration from 4, 4, and 30 samples, respectively. The tensile test data is presented in Figure 2.17.

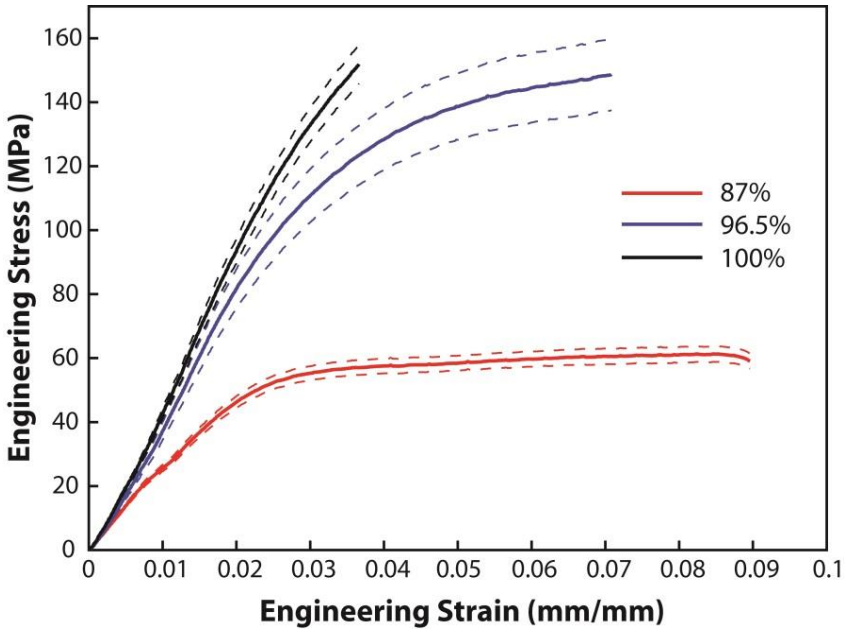

Figure 2.17: Stress-strain plots of CMC at three concentrations:100% (when sterilized at 120°C), 96.5% (22.5 min post sterilization) and 87% (steady-state concentration). Average values for each concentration level are represented with solid lines and the total range of data is indicated by bands around the average.

As expected, it is seen that increased moisture content reduces the Young's modulus and ultimate tensile strength, while increasing the maximum strain of the material. The average values of Young's modulus for the 100%, 96.5% and 87% samples are 5.27±0.22 GPa, 4.05±0.30 GPa, and 2.55±0.13 GPa, respectively. Similarly, measured average tensile strength values of 100%, 96.5%, and 87% samples are 152±6.2 MPa, 148±15.8 MPa, and 65±2.3 MPa, respectively. The maximum strain values for 100%, 96.5%, and 87% samples are 3%, 7%, and 9.2%, respectively.

A set of tensile tests are also conducted for different dissolvable material blends at 96.5% concentration. Figure 2.18 shows the average tensile test results for CMC and four CMC blends

over four samples for each material. Table 4 tabulates the Young's modulus, ultimate tensile strength, and maximum strain values for each material. CMC has the highest Young's modulus, whereas CMC-15% glucose has the highest tensile strength, while exhibiting a Young's modulus value that is very close to CMC-only material. Blending with sugars increases the brittleness of the material.

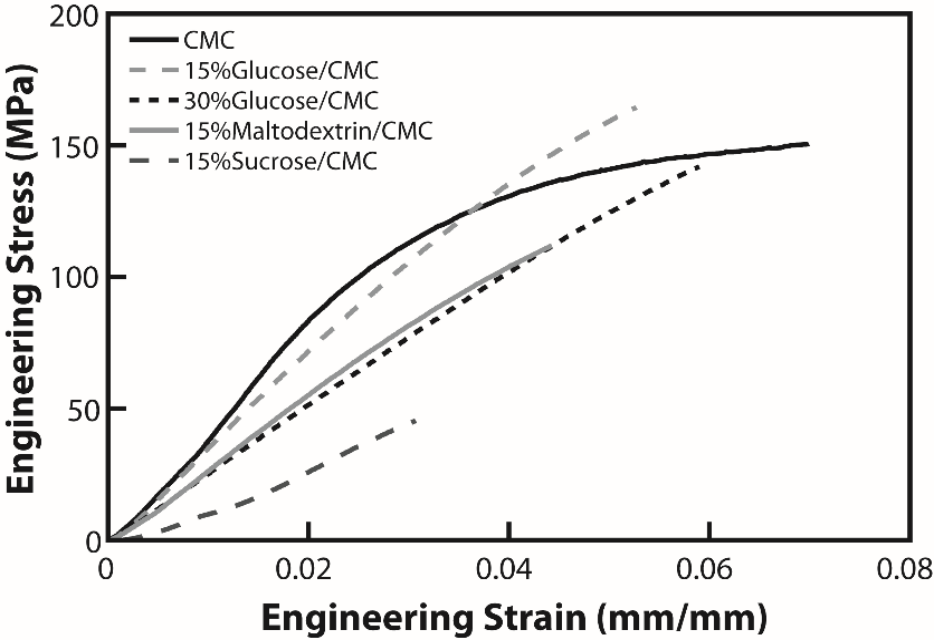

Figure 2.18: Stress-strain plots for CMC and CMC blends at 96.5 % concentration.

Table 2.4: Average material properties of CMC and CMC-sugar blends.

Material	Young's Modulus (GPa)	UTS (MPa)	Maximum Strain (%)
CMC	4.05	148	7
CMC-15% Glucose	3.7	165	5.3
CMC-30% Glucose	2.9	142	5.9
CMC-15% Maltodextrin	2.7	115	4.5
CMC-15% Sucrose	1.4	46	3.1

2.2.5 Insertion and dissolution of needles

To demonstrate that the dissolvable needles can penetrate brain tissue without failure, the 1.65 mm-long dual-shank needles are inserted into bovine cadaver brain tissue sections. Figure 2.19 provides a cross-section image of the brain tissue at approximately 700 μm from the tissue surface at one minute after the insertion of the dual-shank CMC needles (with the dye). Dashed lines in the figure indicate the original cross-section of the needles. It is seen that both the narrow and the wide needles penetrate to this depth without failure. These preliminary results indicate that the needles are successfully inserted without failure (to a depth of at least 700 μm) and they began dissolving inside the tissue.

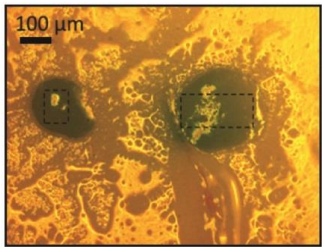

Figure 2.19: An image of the cross section of cadaveric brain tissue at 700 μm depth one minute after insertion of dual-probe needles. The stained area mainly reflects the distribution of rapidly-dissolving dye (with its small—700 Da—molecular weight) into the intercellular space.

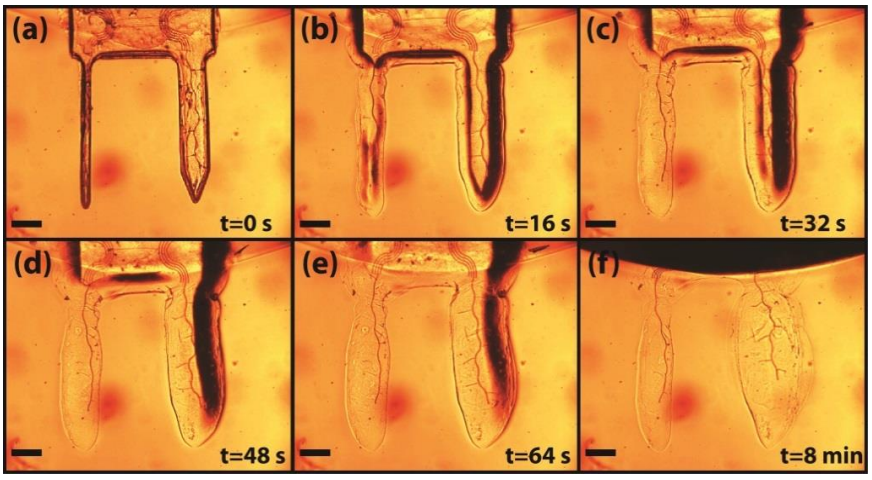

Figure 2.20: Dissolution testing in agarose gel. The images are taken at six different time points, **a** t = 0 s; **b** t= 16 s; **c** t = 32 s; **d** t = 48 s; **e** t = 64 s; **f** t = 8 min. CMC starts absorbing water immediately and forms a hydrogel (Scale: 300 μm).

To observe the dissolution behavior of the needles with the embedded wired probes, a CMC dual-shank needle is inserted into agarose gel using the insertion device. Snapshots of needles and the wiring are seen in Figure 2.20 for six different time points up to 8 min. It is seen that needle dissolution commences immediately after insertion, and rapidly progresses. The needles are seen to swell by absorbing water from agarose gel. At the time point of 8 min, the dissolution is nearly completed. In general, the dissolution behavior and dissolution speed of the dissolvable needle will be different when inserted into agarose gel from when inserted into living tissue. For instance, water availability is considerably higher in agarose gel than that in the brain tissue. However, such "accelerated" dissolution test may be used for comparative evaluation of different needle materials.

2.3 Summary and Conclusions

In this chapter, we present a neural probe with meandered geometry and 2.7 μm by 10 μm cross-section Px-Pt wiring. As evidenced by finite-element analysis, the Pt-Px neural probe provides "ultra-compliance" and "ultra-miniaturization" that greatly reduces tissue strain upon micromotion of the external probe cabling or intrinsic bulk motion of the brain tissue, when compared to conventional Si probes. The very high compliance could significantly reduce the foreign-body response of brain tissue for chronic BMI applications. The micromolded biodissolvable insertion vehicle in the form of a needle that encases the probe enables the probe to penetrate into the tissue. Co-development of the design and fabrication processes for the probe and the dissolvable needle led to successful molding of the needle around the probe. The CMC-sugar materials are strong enough to allow failure-free mechanical insertion into brain tissue at

needle sizes down to 100 μm in width. The dissolution of the needles in agarose gel occurs within minutes, though the CMC is not immediately dispersed into the agarose media.

Specifically, we conclude that,

- These ultra-compliant probes can be successfully fabricated using standard batch microfabrication techniques and the proposed spin-casting process enables reproducible fabrication of dissolvable needles that encase the ultra-compliant meandered probes
- The needles facilitate mechanically failure-free penetration of the probes into brain tissue and dissolve after implantation
- The fabrication process enables needle geometries to be dictated for optimal insertion parameters
- Two-dimensional needle-encased probe arrays with diverse needle geometries can be readily realized and can also be used to co-deliver drugs, such as anti-inflammatory agents
- Ultra-compliant meandered probes significantly reduce strain from micromotion in brain tissue as compared to stiff probes. Overall, the presented ultra-miniature ultra-compliant probes show great promise toward addressing the challenges of performing stable chronic recordings from and stimulations to the brain.

Although the presented ultra-miniature ultra-compliant probes show great promise toward delivery of subcellular size probes, only 2D shaped needle designs can be fabricated using a planar molding approach. Additionally adhesion between the Si-surface needs to be carefully curated to ensure wires do not delaminate from Si-mold. In chapter 2, we present the methods and modification made to current process to overcome the challenges.

Chapter 3

Direct Bonding Method

The previous chapter presented an accurate and reproducible novel fabrication approach for integration of ultra-compliant, ultra-meandered probes with a biodissolvable delivery vehicle. The CMC needles and the needles created from CMC combined with other lower molecular weight sugar-based materials were shown to have sufficient mechanical strength to penetrate both the brain tissue and phantom agarose gel to deliver the ultra-miniature probes to the targeted location. Despite these promising results with the sugar-based delivery vehicles, the approach presented in Chapter 2 still needs further improvements, especially in the step of integrating the ultra-miniature probes with the dissolvable delivery vehicles. Specifically, the approach still requires an etch-pit as for the integration of probe and delivery vehicle. However, this etch-pit is the major contributor to the yield loss. Furthermore, delamination during the lithography process to create the etch-pit also contributes to the yield loss. Delamination of the probes during the assembly of the resin top mold with the bottom mold is also challenging, possibly resulting in yield loss. Moreover, complications occur at the interface where the probe transitions from being suspended over the etch-pit to directly resting on the Si-surface during the spin casting process. Specifically, due to the shrinkage of dissolvable material away from the etch-pit walls during drying , the wire encapsulated in the molded needle handling tab exerts undesired strains onto the connecting wire, which results in physical damages in the insulation layer and in the wire.

Due to the potential problems with the existing probe and delivery vehicle integration because of poor performance of etch-pit in ensuring symmetric integration within the delivery vehicle, the fabrication approach is modified to eliminate the necessity of an etch-pit and to improve the process yield by eliminating the aforementioned shortcomings.

3.1 Modification of the Fabrication Approach

3.1.1 Fabrication and molding on Si-molds without etch-pits

Reliable integration of probe to CMC required some amount to hydrogel material to flow underneath the Px layer, such post spin-casting and drying it creates mechanical interlocking between the two. Isotropic etching of Si can create 2 μm undercuts as it doesn't etch away and affects the Px-layer or the UV curable resin that was used for the top mold. The Px-layer can act as a mask the Si-substrate underneath which can assist in creating undercut during isotropic etching using XeF_2. In the overall scheme of the fabrication approach to creating the Si-mold, all the steps for creating the Px-Pt wire and electrode on the Si-surface are same as described in section xx of the previous chapter. Thereafter, isotropic etching is done to create small undercuts that would be sufficient for the hydrogel to flow and grips onto probe post drying. The isotropic etch was performed using XeF_2 (Xactix, SPTS, Newport, UK), using 3 etch cycles (1 cycle: 60s, 3mT XeF_2 partial pressure, 2mT N_2 partial pressure).

The undercuts provide a necessary mechanical interlocking with CMC during the molding step to ensure probes are successfully integrated with CMC delivery vehicle which at the same time eliminating the necessity for having a probe suspended over etch with is a far more complicated and expensive process, and has much higher yield loss. Once the Si-molds with undercuts is fabricated, the subsequent fabrication steps remain unchanged as described in Chapter 2 and also shown here in Figure 3.1. Explaining briefly, the Si-mold is assembled with

the resin mold and spun-cast to achieve probe and biodissolvable needle integration. This method significantly improved the yield at each step from the fabrication of Si-mold to, assembly with PU mold as well as successful molding of functional CMC delivery devices. Figure 3.1 also shows the fabricated probe with the modified Si-probe. The assembly and molding process is similar to that described in Chapter 2.

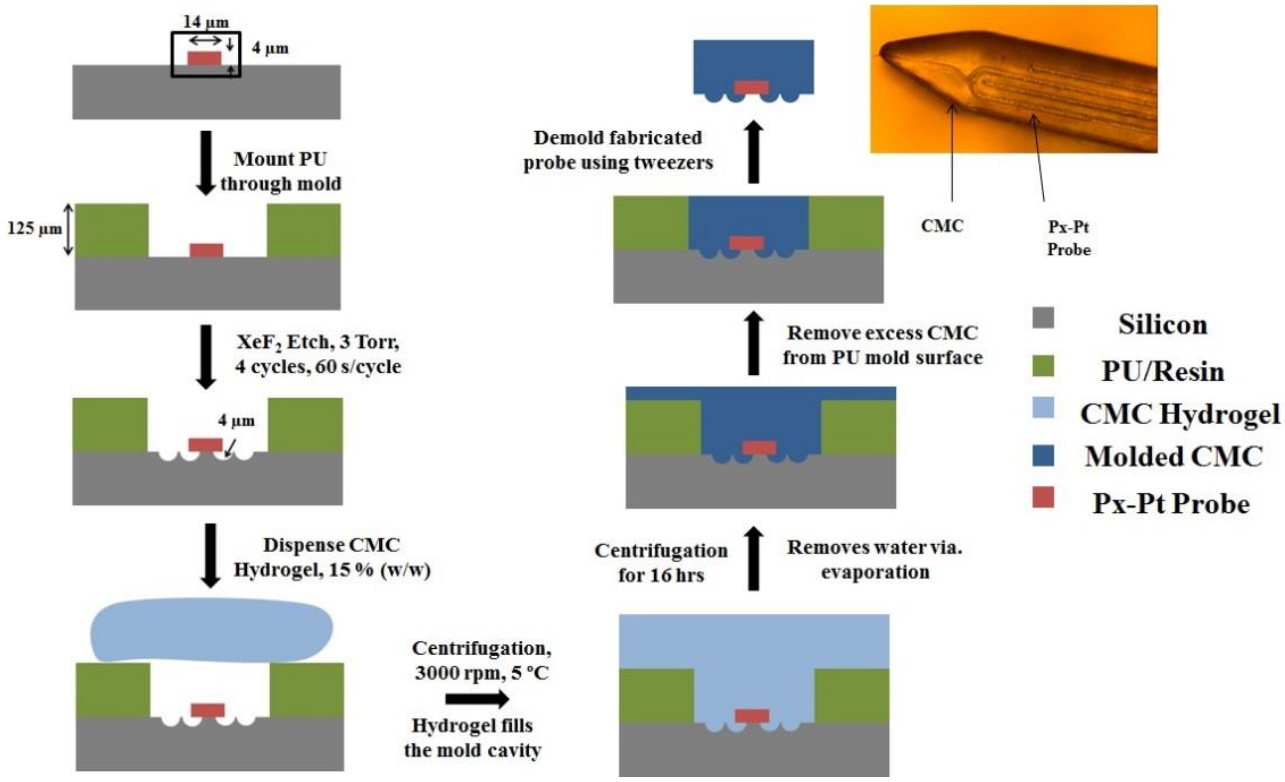

Figure 3.1: A Method to integrate the Px-Pt probe with the CMC delivery vehicle using isotropic XeF_2 etching to create 2 µm undercuts. The mold assembly and spin casting process are same as described previously in Chapter 2.

3.1.2 Spin casting on the sacrificial materials

The delivery vehicles fabricated via. the previous process was found to have poor insulation properties due to leakage at Px-Px interface that is formed during two different Px-deposition steps. Thermal annealing in vacuum was determined as a viable method to improve the encapsulation characteristics of Px, however, this led to an increase in adhesion between the Px

and Si-substrate that undermined the peeling process. The transfer process step that eliminates the peeling process and transfers the probe on to a glass substrate coated with an adhesive sacrificial layer was determined to be viable methods to integrate the probe with CMC needles while at the same time enhance the Px encapsulation properties. BGL that is soluble in IPA was used as a sacrificial adhesive material as it CMC is insoluble in IPA as well it's mechanical and material properties are not affected by the BGL solvent. The fabrication process for integrating the probe along with transferred probe (transferred from Si to Glass substrate) is shown in Figure 3.2 shows the assembly and molding process remain the same as described previously with an additional step of IPA treatment to release the CMC-probe integrated device from the glass that dissolves away the BGL.

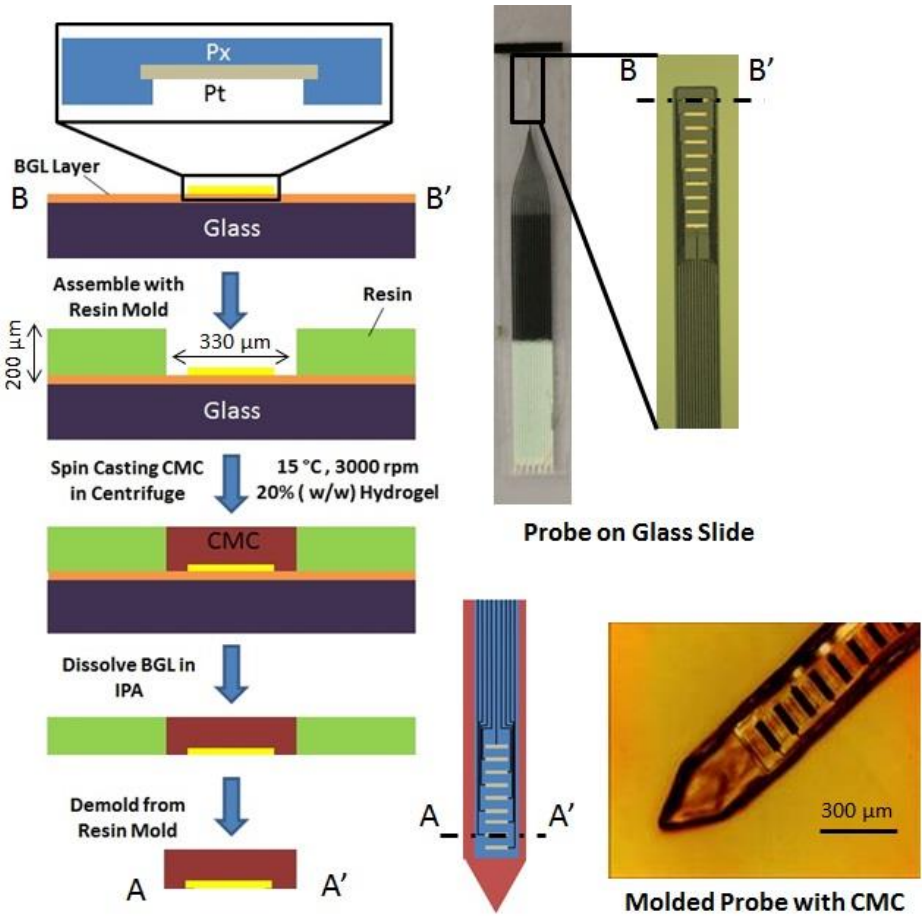

Figure 3.2: Integration of probes via CMC molding and using BGL as sacrificial layer.

3.1.3 Direct assembly process

The integrated CMC-probe delivery devices fabricated via. molding the probe on sacrificial BGL coated glass slides were found to have two primary drawbacks:

a) **Delamination of probe from CMC needle**: Unlike the previous method where molding was done with Si-substrate that either encapsulated the probe with CMC with the help of etch pit, or mechanical interlocking due to undercuts present beneath the Px-Pt probe, the method described in the previous section doesn't mechanically constraint the probe from delamination. Instead it relies largely on surface adhesion and friction at the interface of CMC-Px interface walls to adhere the probe to the CMC matrix. This adhesion is very weak and leads to delamination of probe from the delivery vehicle causing significant yield loss. Moreover, residual stresses developed during Pt-deposition causes the Px-Pt probe to bend out of plane, thereby facilitating delaminating of probe from the molded needle.

b) 2) **Poor insulation post molding step**: Electrochemical Impedance Spectroscopy (EIS) tests carried out on fabricated CMC-probe devices showed that insulation properties were still poor despite the vacuum annealing treatment of the probes prior to transfer and molding. It was observed via EIS measurements that the probe has different insulation characteristics before and after molding with CMC which was primarily attributed to the physical damage caused to Px due to residual stresses occurring during the solvent casting of CMC. Figure 3.3(a) shows the micro-cracks caused to such residual stress during the molding stage and Figure 3.3(b) shows the results from EIS analysis show no difference in impedance between the exposed electrodes and insulated wire.

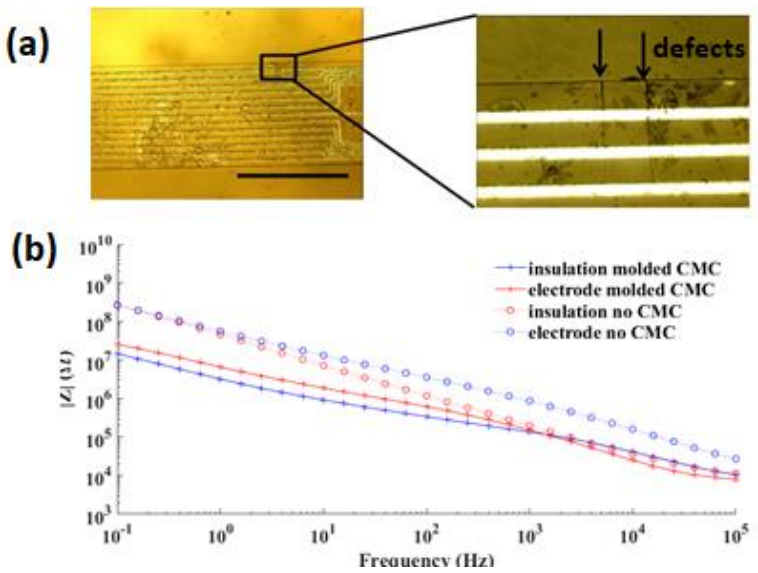

Figure 3.3: (a) Microcracks on Px probe when CMC is molded directly on the Px-Pt Probe, **(b)** EIS measurements shows poor insulation property for probe integrated with CMC and comparison with that of probe without CMC.
(*Mats Forssell conducted EIS measurements)

To address the aforementioned challenges, a new direct needle-probe assembly bonding technique was developed to improve the adhesion between the probe and the CMC needle. To overcome the adhesion challenge between the CMC polymer matrix and Px probe as discussed in the previous section, O_2 plasma was used to treat parylene-C in order to make parylene-C more hydrophilic. Droplet tests were performed with DI water to ensure hydrophilicity was maintained for sufficient time in order to perform the direct-bonding process which requires 15-30 mins post activation.

The CMC Needle is contained in a PDMS holder and a thin layer of 15% gelatin liquid is cast in the centrifuge for 2 min over the CMC/glucose needle. 15% gelatin is heated to 50° C is ensure it is in liquid state. The PDMS holder along with the coated CMC/glucose needle is mounted on the vacuum chuck in the device bonder, aligned with the probe using the camera alignment system, and then bonded together. The assembly is heated to 80° C for 1 hr, under a

constant load of 20N (500MPa). The PDMS and glass slide assembly is then cooled down to room temperature and placed in IPA bath to release the bonded probe-needle assembly from glass slide.

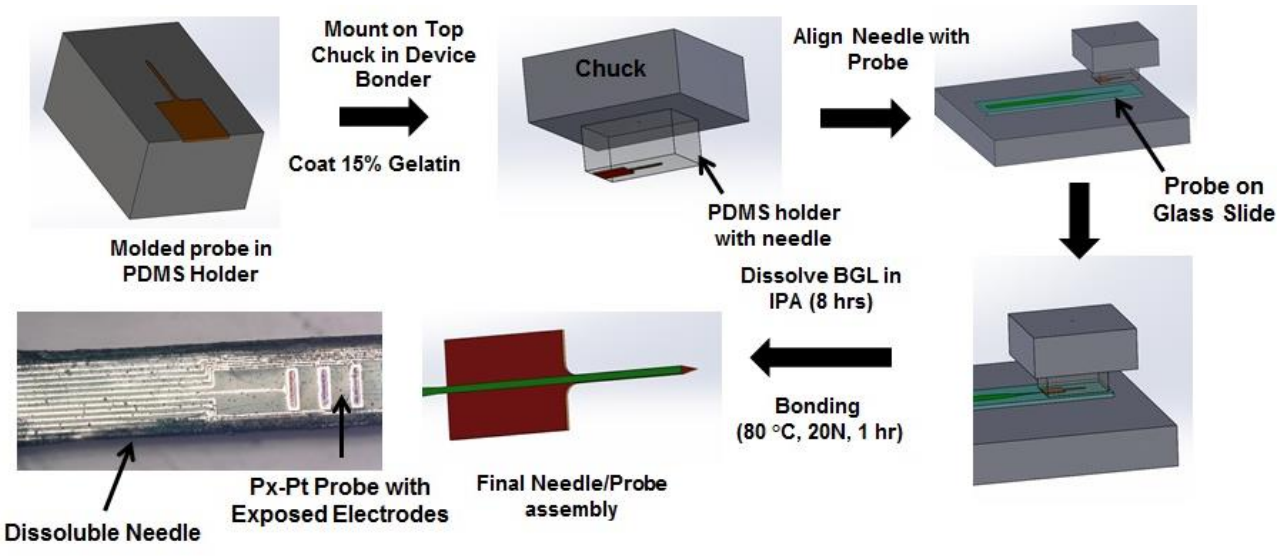

Figure 3.4: Direct low-stress bonding of Px-Pt probe to CMC delivery vehicles using plasma treatment on probe to increase its hydrophilicity and gelatin as adhesive layer.

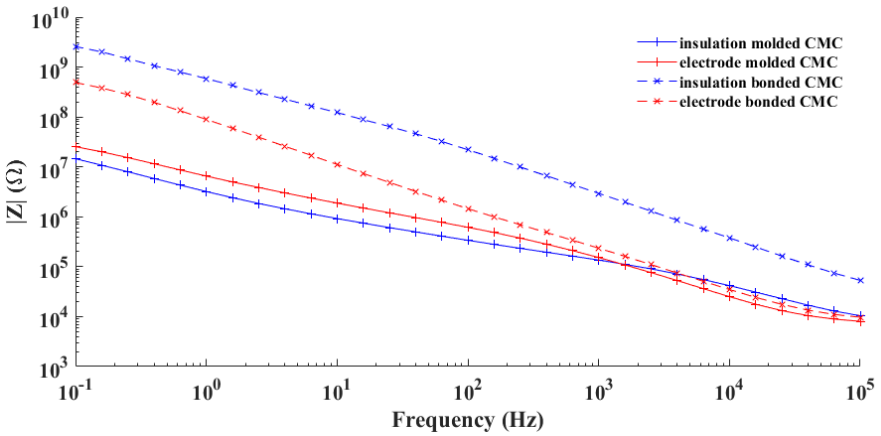

Figure 3.5: EIS measurements showing improvement in insulation properties following low stress bonding process. A plot shows comparison between self-test loop (isolated) and the electrodes for both, bonded and molded probes integrated with CMC.

The O_2 plasma treatment enhanced the adhesion between the CMC/Glu (85/15) needle and Px-Pt probe as similar bonding method performed without plasma treatment lead to delamination

of probe from CMC/glucose needle. Repeatable and reproducible bonding could between the probe and the delivery vehicle could be achieved using this method with improved adhesion and eliminates the necessity of molding CMC/Glu directly over the probe. EIS tests performed on the fabricated devices demonstrated improved encapsulation properties which as shown in Figure 3.5 which was observed as a major drawback of the direct-molding approach.

Advantages of the direct-assembly approach are:

1) The process removes any manual intervention to integrate probe with the needle which is a primary challenge as seen in literature. Most research groups manually transfer the flexible probe to another substrate such a as a PDMS/PMMA mold in order to integrate with biodissolvable polymer via. molding or integrate with shuttles using biodissolvable adhesives such as Poly(ethylene) Glycol (PEG).
2) The direct assembly approach can be used to assemble 2D array probes under similar conditions (force is varied depending upon the surface area). An example for same is shown in Figure 3.7. Hence, the process is scalable and could further be explored on wafer level scale to improve the scalability of the process.
3) Lastly and more importantly, the process decouples the fabrication of delivery vehicles from the fabrication of probes which gives larger flexibility for design of both the delivery vehicle (geometry and material) as well as design of probes. So as compared to the planar process which limits the tip geometry to wedge tip only amd sharp tip geometries cannot be realized with that approach, the current process offers larger flexibility in design of such needle. The decoupled process also allows for integration of sharp needles with probes directly expanding the design space to optimize needle geometry for a wide range of geometries such as the high aspect ratio needle (15:1) shown in Figure 3.6.

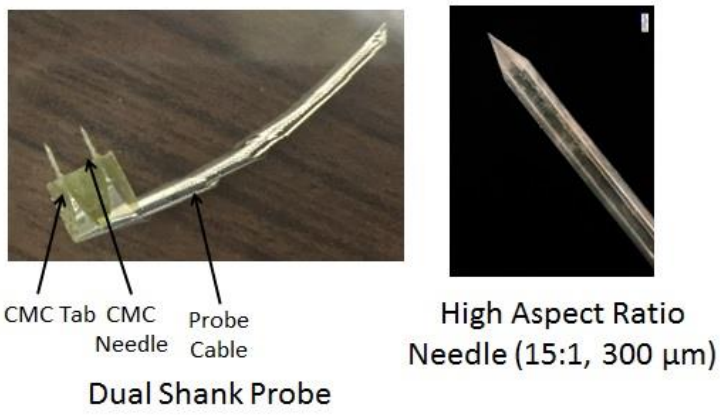

Figure 3.6: Dual shank probe fabricate by direct bonding method. A high aspect ratio needle with pyramid tips is fabricated to show the benefits of the decoupled approach.

3.2 Summary and Conclusions

This chapter presented an improved approach to integrate the compliant probe with the CMC delivery vehicle. Three different methods were tried to progressively address the drawbacks of the previous method.

First, Si-molds were created without etch-pits by replacing the DRIE process with the isotropic XeF_2 etching to create miniature undercuts below the Px-Pt probe, followed by spin-casting to integrate the probe with delivery vehicles. Although this method improved the yield up to 70%, the poor Px-Px interface created during the Si-mold fabrication required annealing, which increased the surface adhesion of the probes to the Si-substrate.

Next, the annealed Px-Pt probes were transferred to BGL (a sacrificial material soluble in IPA) coated glass slides and CMC was molded using the same spin-casting approach. IPA was dissolved to release the probe-CMC needle assembly from the glass substrate. Electrical impedance spectroscopy (EIS) analysis showed that molding CMC directly over the miniature probes resulted in poor insulation properties due to defects caused by strains resulting from the shrinkage of CMC during drying.

Finally, a direct assembly method was developed to ensure defect-free integration of probes with the CMC delivery vehicle. A pre-molded CMC needle was directly bonded with the Px-Pt probe by using a thin gelatin layer as an adhesive and treating the Px-Pt probe with oxygen plasma for improved adhesion. EIS analysis showed improved insulation properties, confirming the integrity of Px insulation for reliable measurements. The direct assembly method increases the design space for both the needle and probe design since they are fabricated separately. To show the flexibility of the direct method, the method was demonstrated with fully 3D pyramid head needles with relatively sharper tip geometries as compared to wedge heads.

The specific conclusions of this study are listed as follows:

- Si-molds with etch-pits result in yield loss since the probes move to the bottom surface of the molded CMC during the centrifugal spin-casting process.
- Process yield can be improved by creating 2 µm undercuts using isotropic etchin. However, this results in poor insulation which requires annealing of the Px-Pt probe which increases its adhesion to Si-substrate.
- Molding of CMC over sacrificial BGL layer results in defects on the Px-Pt probe, which leads to poor insulation.
- The direct assembly method integrates the probes with the CMC delivery vehicles while ensuring the integrity of the Px insulation layer.

The direct assembly of the probes with the delivery vehicles shows great promise to expand the design space and explore different delivery vehicle geometries. One of the key considerations during the design process is the impact of geometric parameters and insertion velocity on tissue-needle interaction forces.

Chapter 4

Insertion Force Analysis

A fundamental understanding of the mechanical interaction between delivery vehicles of the subcellular-sized neural probes and brain tissue is critical for successful insertion of those neural probes. Specifically, the delivery vehicle-brain tissue interaction forces must be probed for different designs and insertion conditions to enable optimal design of delivery vehicles and to identify favorable insertion parameters for failure-free application. Furthermore, it could be possible to correlate these interaction forces with ensuing tissue damage [81]. As such, it is necessary to conduct a comprehensive study to understand the effects of delivery vehicle design (i.e., geometry and material) and insertion (i.e., speed) parameters on insertion forces.

This chapter presents a systemic study to provide insight into delivery vehicle-brain tissue interaction mechanics. Specifically, an experimental study is conducted to evaluate the effects of geometric parameters and materials of the delivery vehicles, as well as of the insertion speed on the insertion forces during interaction with an established brain tissue phantom (0.6 w/w% agarose) and with freshly excised rat brain tissues. To accurately and reproducibly measure the insertion forces, a custom-made force measurement system is developed. First, non-dissolvable delivery vehicles (i.e., needles) are used on the established brain phantom to investigate the effect of geometric parameters and insertion speeds. Subsequently, favorable geometries are identified based on the results obtained with the non-dissolvable needles to perform insertion studies with

dissolvable needles. The same subset of designs is then used to conduct insertion experiments on the rat brain tissues. The findings presented in this chapter could help identify favorable designs and insertion speeds for delivery vehicles of ultra-miniature neural probes.

4.1 Experimental Methods

4.1.1 Experimental setup

Accurate and reproducible measurement of delivery vehicle-brain tissue interaction forces poses certain challenges due to relatively low force magnitudes (<100 mN). Specifically, the existing force measurement systems fail to provide sufficient space, resolution, and sensitivity for reliable insertion studies on brain tissue [86].

To enable reliable measurement of the axial component of external forces acting on neural probe delivery vehicles, a custom-made force measurement system is developed. First, a flexure-based sensor with a symmetric cross-beam structure is designed using COMSOL multiphysics modeling software to achieve sufficient sensitivity and high natural frequency. Aluminum 6061 is chosen as the sensor material since there are commercially-available thin aluminum shims (<1 mm thickness). The geometric parameters of the sensor are determined based on the COMSOL simulations and are shown in Figure 4.1. Specifically, the width, length, and thickness of each beam are identified to be 1 mm, 37.5 mm, and 0.625 mm, respectively, Furthermore, a 10 mm x 10 mm platform is also included in the design to enable attachment of the delivery vehicle or brain tissue. Ultimately, the compliance of 0.5 μm/mN and natural frequency of 370 Hz are achieved with this particular beam design. The designed sensor is then accurately fabricated through mechanical milling technique and calibrated using predetermined weights and its stiffness was determined to be 2.18 mN/μm.

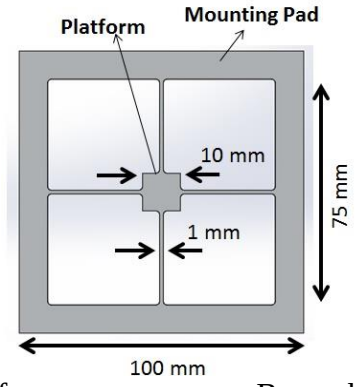

Figure 4.1: Flexural beam design for force measurement. Beam thickness is 0.625 mm.

Next, the custom-made insertion force measurement system is constructed to accurately and reproducibly measure forces during application of the delivery vehicles in the brain tissue or brain tissue-mimetic phantom. As shown in Figure 4.2, the set-up consists of three major components: **1. A flexure-based sensor, 2. A non-contact displacement sensor (i.e., laser interferometer), and 3. A three-axis precision motion stage.**

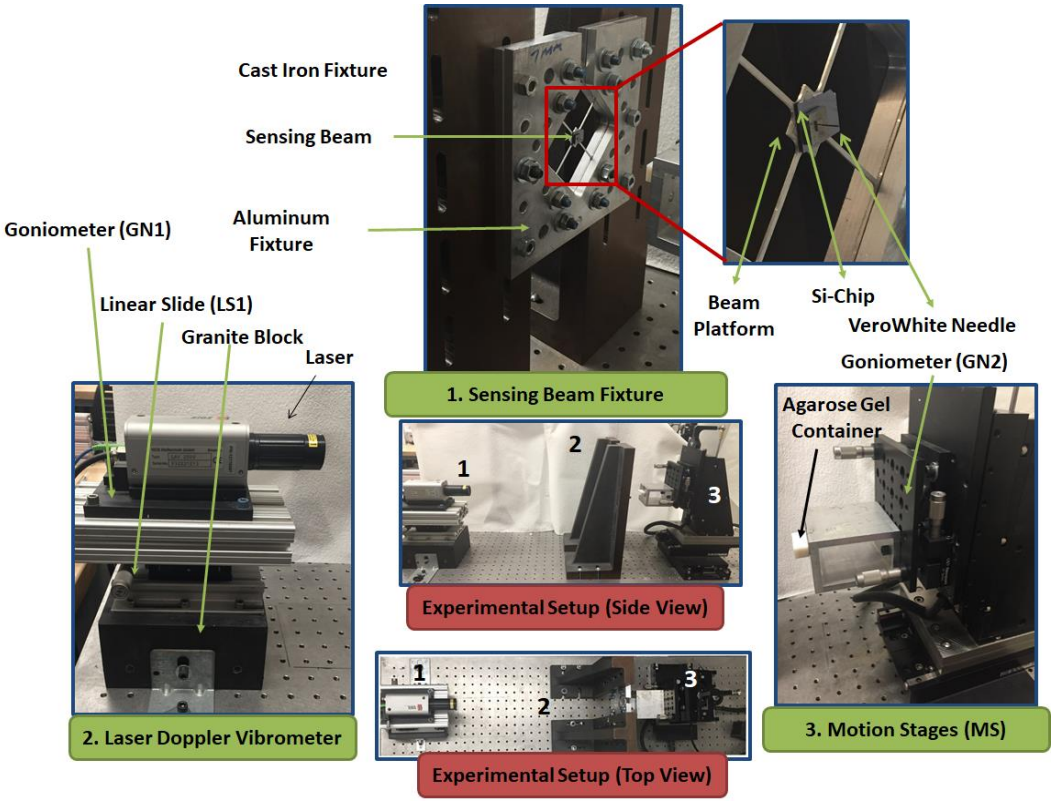

Figure 4.2: Experimental setup for the insertion force measurements.

(i) **A flexure-based sensor:** The fabricated flexure-based sensor is fixed between two aluminum frames with a thickness of 6.25 mm through its mounting pad, thereby making only the beams to deflect when a force is applied to the center of the platform. The fixed sensor is mounted to two cast iron blocks in a vertical position. The delivery vehicle (i.e., the needle) is attached to a silicon (Si) chip or wafer that enables the alignment and then the needle-Si-chip assembly is mounted onto the platform face. To ensure reliable displacement measurements, a reflective tape is attached to the other side of the platform.

(ii) **A non-contact displacement sensor**: A laser interferometer (SIOS Meßtechnik GmbH) is used to measure the deflection of the calibrated flexure-based sensor during insertion studies. To enable the alignment and focus of the laser, the displacement sensor is mounted on a goniometer which is attached to a linear slide. The entire setup is mounted onto a granite block to dampen out external vibrations.

(iii) **A three-axis precision motion stages:** A three-axis precision slides is used to provide brain tissue phantom or brain tissue with a constant linear velocity during insertion experiments. The tissue model is mounted on an aluminum frame. The aluminum frame is mounted onto a goniometer, and a Si-chip is attached to the aluminum frame for the alignment purpose.

4.1.2 Experimental design

To study the effects of geometric parameters and materials of the delivery vehicles, as well as of the insertion speed on the insertion forces, the experiments are performed with both non-dissolvable and dissolvable needles on both the brain tissue phantom (0.6 w/w% agarose) and excised rat brain tissues. First, an extensive study is performed with non-dissolvable needles on

the brain tissue phantom to provide a basis for experimentation and to investigate the effect of a wide range of geometric parameters. Next, a subset of design parameters is identified to conduct the insertion experiments with dissolvable needles on the brain tissue phantom. Finally, the same set of design parameters is used for the insertion studies with both non-dissolvable and dissolvable needles on excised rat brain tissues.

Insertion experiments with non-dissolvable needles on the brain tissue phantom

To conduct the insertion experiments with non-dissolvable needles, high-aspect ratio needles are fabricated from an ultra-violet(UV) light curable resin (VeroWhite) using a hybrid manufacturing technique that combines micromilling with a two-stage molding method (Figure 4.3). Briefly, Poly (methyl methacrylate) PMMA mastermolds with a single needle are created using mechanical micromilling technique. The micromilled PMMA needles are then utilized in a two-stage molding process to first fabricate the negative PDMS molds which are then utilized to produce the final VeroWhite needles that are used for the insertion tests.

To fabricate PMMA mastermolds, two different cutting tools (i.e., tapered and straight end-mills) are used during micromilling process. The tip region of the needles is created using tapered single crystal diamond milling tools, where the angle of the needles is dictated by the angle of the diamond tool (i.e., 15° and 22.5° half angle). After creating the tips, a tungsten-carbide square end-mill with a diameter of 1 mm is used to manufacture the needle shanks. The total length of the needle is 4.5 mm.

The fabricated PMMA mastermolds are then used to create the Polydimethylsiloxane (PDMS) production molds through elastomer micromolding. The PMMA mastermolds are mounted in a petri-dish and a 10:1 PDMS mixture (base: curing agent) is poured on top of them, degassed, and cured for 1 hour at 80^0C. The molds are cooled down and the cured PDMS molds are demolded

from the PMMA mastermolds to obtain the production molds which are essentially negatives of the mastermolds with needle-shaped wells.

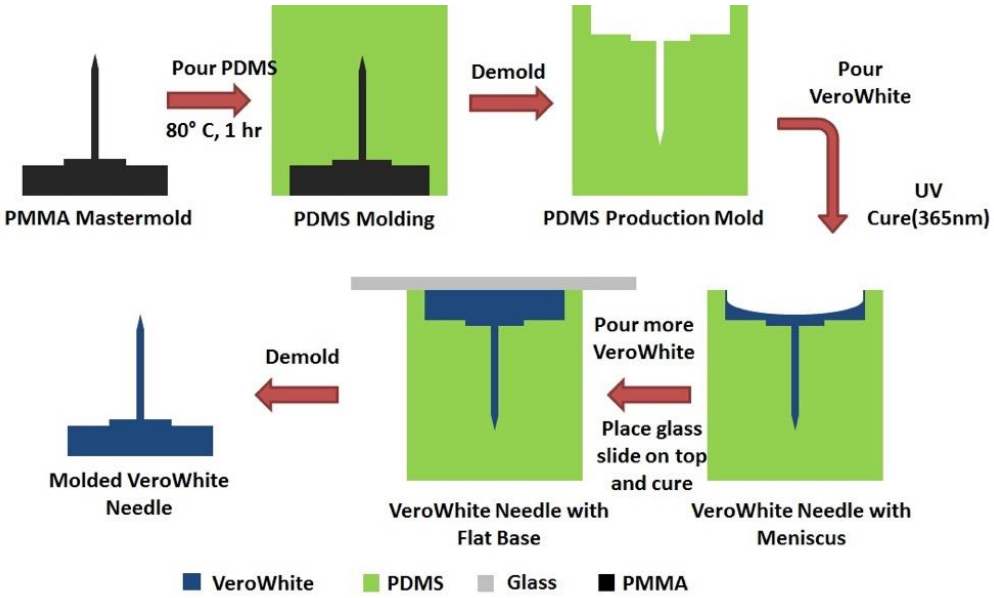

Figure 4.3: A two-stage molding approach for fabrication of VeroWhite needles.

The manufactured PDMS production molds are then used to fabricate the positive VeroWhite needles. To this end, 0.2g of uncured UV-curable resin VeroWhite is poured into the PDMS molds and centrifuged at 2000 rpm for 5 mins to ensure the uncured resin flows into the narrow region of the mold including the tip region. The resin is cured under the UV light with a wavelength of 365 nm to form the needle shape. Next, additional 0.1g of UV-curable resin is poured into the PDMS molds and a glass slide is placed on top of the mold to create a uniform flat surface at the base. The resin is further cured from the top side for 10 mins and cooled down at room temperature for 10 mins before demolding the final VeroWhite needles. The fabricated VeroWhite needles are characterized using an optical microscope and their geometric parameters were measured to verify the targeted dimensions before the insertion experiments.

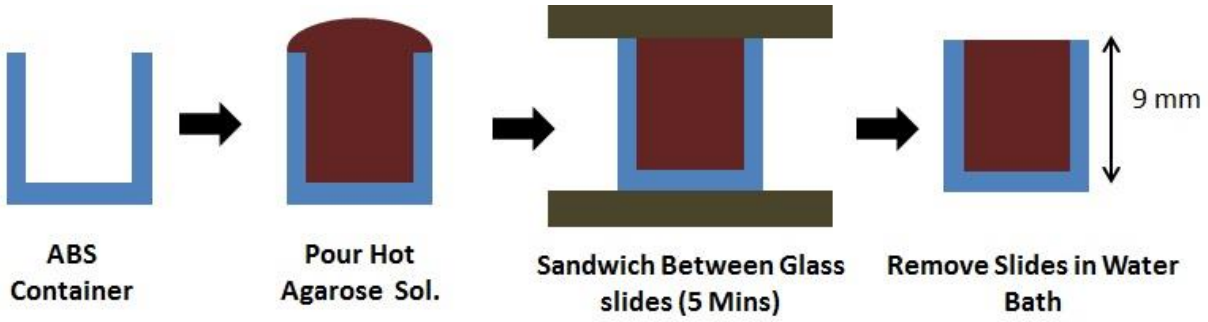

Figure 4.4: A procedure for repeatable preparation of agarose gel.

To reproducibly prepare the brain tissue phantom, a procedure shown in Figure 4.4 is followed. First, 0.18g of agarose powder is mixed with 29.82g of deionized (DI) water to prepare a 0.6% (w/w) concentration agarose solution. The prepared agarose solution is poured into an ABS container with the intended floating (Figure 4.4). The top surface of the ABS container with the excessive agarose solution is covered with a glass slide to squeeze out the additional agarose solution and to prevent any further evaporation from the surfaces, as well as to dictate a smooth and flat surface. Next, the glass slide is removed, and the ABS container is attached to the 3-axis slides to perform the insertion tests. This method leads to uniform and reproducible preparation of agarose gels for conducting a large set of insertion experiments with brain tissue phantoms.

Subsequently, a comprehensive study is performed using non-dissolvable VeroWhite needles on a brain tissue phantom (0.6%) to investigate the effects of different design parameters and insertion conditions on axial components of the insertion forces. Specifically, the following experiments are designed to gain a complete and through understanding of different geometric parameters and insertion speeds on the delivery vehicle-brain tissue interaction forces:

Effect of geometric parameters: The effects of ***cross-section area and type, apex angle, and tip type and radius*** are probed through the insertion experiments. To understand the effect of *cross-section area*, the experiments were performed with pyramid tip needles (30° apex angle and 6 μm tip radius) with varying square cross-sections (160 μm x 160 μm, 210 μm x 210 μm,

260 µm x 260 µm, and 310 µm x 310 µm). To study the effect of *cross-section type*, three different shaft cross-sections (square, rectangular, and circular) with pyramid or conical tips (30° apex angle and 6 µm tip radius) while keeping the needle cross-section area (or shank volume) constant are included for the insertion experiments. To demonstrate the impact of *tip type*, pyramid and wedge tips with (30° apex angle and 6 µm tip radius), as well as flat tips (a punch geometry) are used, and the cross-section area of the needles is chosen to be square 210 µm width. To investigate the effect of *apex angle*, two different apex angles (30° and 45°) are used with pyramid needles with 6 µm tip radius and 210 µm x 210 µm square cross-section shaft. To evaluate the effect of *tip radius*, two different tip radii (6 µm and 15 µm) are used with pyramid (30° apex angle) and square cross-section (210 µm x 210 µm) needles.

Effect of insertion speed: The effects of ***insertion velocity*** are studied for varying insertion speeds (i.e., 0.3 mm/s, 1 mm/s, 5 mm/s, 15 mm/s, and 25 mm/s). These insertion speeds parameters are used for all the experiments with non-dissolvable and dissolvable needles on both the brain tissue phantom and excised rat brain tissues.

The design of experiments matrix for the insertion studies are listed in Table 4.1.

Table 4.1: Design of experiments matrix for the insertion studies with non-dissolvable needles.

Experiment Design (Repetition: N=3)						
	Tip Type	**Tip Apex Angle (°)**	**Tip Radius (µm)**	**Cross-Section Area (μm^2)**	**Cross-Section Type**	**Insertion Speed (mm/s)**
Cross-Section Area	Pyramid	30°	6	160µm*160µm	Square	0.3 mm/s, 1 mm/s, 5 mm/s, 15 mm/s, 25 mm/s All five insertion velocities are tested in each case
				210µm*210µm		
				260µm*260µm		
				310µm*310µm		
Tip Type	Pyramid	30°	6	210µm*210µm	Square	
	Wedge	30°	N/A			
	Flat	N/A	N/A			
Apex Angle	Pyramid	30°	6	210µm*210µm	Square	
		45°	6			
Tip Radius	Pyramid	30°	6	210µm*210µm	Square	
			15			
Cross-Section Type	Pyramid	30°	6	210µm*210µm = C	Square	
	Conical		6	π*235μm^2 = C	Circular	
	Pyramid		6	165µm*265µm = C	Rectangular	

To evaluate the reproducibility of agarose gel formed and repeatability of the insertion force measurements, 30 different insertion experiments are conducted using a single needle design and insertion speed. Specifically, square cross-section VeroWhite needles with a width of 210 μm and with sharp pyramid tips (30° apex angle and 6 μm tip radius) are inserted into 0.6 w/w% agarose gel at the speed of 15 mm/s. These 30 experiments are divided into 6 different sets of experiments so that only 5 experiments are conducted on a single sample of agarose gel. The other experiments are repeated 3 times to evaluate the reproducibility of the results.

Insertion experiments with dissolvable needles on the brain tissue phantom

To perform the insertion experiments with dissolvable needles, high-aspect ratio needles are fabricated from a biodissolvable material composition (85%CMC and 15%Glucose) using the hybrid manufacturing technique described in Figure 4.3. Briefly, the PDMS production molds are manufactured as outlined in the previous section. Hydrogel form of the dissolvable material with the concentration of 15 w/w% is prepared by dissolving the powder form of dissolvable materials into DI water and 0.3g of the prepared hydrogel is dispensed into each PDMS mold. PDMS molds are spun using a centrifuge at 15°C, 3000 rpm for 10 minutes and then placed in an oven at 80°C for 1 hour, to form the CMC/Gluc needles.

Subsequently, an insertion study with a subset of geometric parameters used with non-dissolvable needles is performed to evaluate the effect of dissolvable material on insertion forces at varying insertion velocities (i.e., 0.3 mm/s, 1 mm/s, 5 mm/s, 15 mm/s, and 25 mm/s). Specifically, the dissolvable needles with wedge and pyramid tips, with 30° apex angle, 6 μm tip radius, and 210 μm x 210 μm square cross-section area are used. The design of experiments matrix for this insertion studies is listed in Table 4.2.

Table 4.2: Design of experiments matrix for the insertion studies with dissolvable needles.

Experiment Design (Repetition: N=3)						
Needle Material	**Tip Type**	**Tip Apex Angle (°)**	**Tip Radius (µm)**	**Cross-Section Area (μm^2)**	**Cross-Section Type**	**Insertion Speed (mm/s)**
CMC/Glu (85/15)	Pyramid	30°	6	210µm*210µm	Square	0.3 mm/s, 1 mm/s, 5 mm/s, 15 mm/s, 25 mm/s All five insertion velocities are tested in each case
	Wedge	30°	N/A			

<u>Insertion experiments with both non-dissolvable and dissolvable needles on the brain tissue</u>

The same subset of parameters used with dissolvable needles on brain tissue phantom is used with both non-dissolvable and dissolvable needles on the rat brain tissue. Specifically, insertion experiments with the brain tissue are conducted using only two different needle designs. The design of experiments matrix for the brain insertion studies are listed in Table 4.3.

Table 4.3: Design of experiments matrix for the insertion studies with brain tissue

Experiment Design (Repetition: N=3)						
Needle Material	**Tip Type**	**Tip Apex Angle (°)**	**Tip Radius (µm)**	**Cross-Section Area (μm^2)**	**Cross-Section Type**	**Insertion Speed (mm/s)**
VeroWhite	Pyramid	30°	6	210µm*210µm	Square	0.3 mm/s, 1 mm/s, 5 mm/s, 15 mm/s, 25 mm/s All five insertion velocities are tested in each case
	Wedge		N/A			
CMC/Glu (85/15)	Pyramid	30°	6			
	Wedge		N/A			

Of all the structures of the brain, the cerebral cortex has a relatively large volume and a homogenous texture [83]. Regardless of the insertion depth and the electrode type, most of the neural electrodes or needles that are reported in the literature are inserted in the brain through the cerebral cortex[86] . For these reasons, the cerebral cortex is chosen as the target insertion area in this study. Specifically, six insertion sites, 2 mm away from the vertical center line (i.e., the location of the M1 cortex), are chosen as the target insertion sites (Figure 4.5a). Since our preliminary experiments showed different force behaviors in the brain tissues extracted from the

skull from those obtained in the brain tissues with the skull, the experiments are conducted on the brain tissues remain in the skull to better represent the *in vivo* insertion conditions (Figure 4.5b).

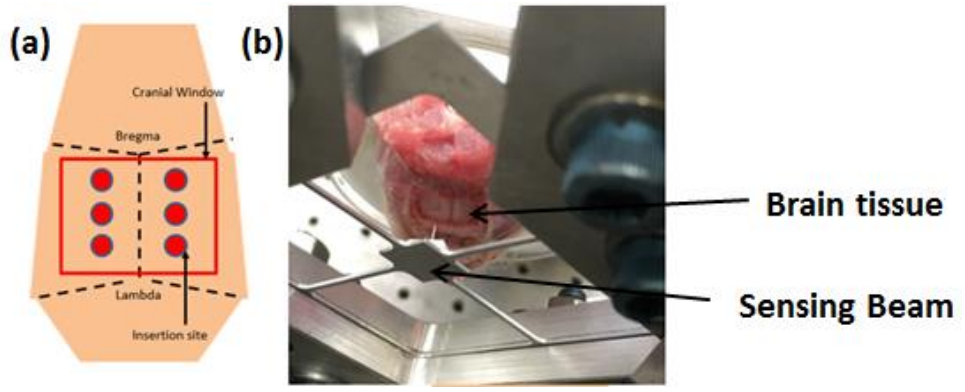

Figure 4.5: Preparation of the rat brain tissue.

4.1.3 Alignment of the needle

The alignment of the needle with respect to the insertion velocity direction is of utmost importance to accurately measure the axial component of the insertion forces, as well to ensure successful insertion of the delivery vehicle. To elaborate, a small misalignment of 1 degree will result in an additional 62 μm kill zone in the tissue, which is about 30% width of the delivery vehicle with a width of 210 μm. As such, it is critical to align the needle axis with respect to insertion velocity direction using precision engineering techniques. The precision alignment procedure developed in this study includes three steps:

a. **Measurement of the needle orientation with respect to the Si-wafer**: The misalignment characterization of needle orientation with respect to the Si-chip is performed using an optical microscopy (Alicona InfiniteFocus G4, 20x optical objective piece with a 100nm vertical resolution), which is equipped with a rotational stage with an angular resolution of 0.001°. Prior to the alignment procedure, the needle is coated with Pt (10 nm thick) to improve the quality of the images, and then attached to the Si-chip (9 mm x 13 mm) using an adhesive tape. The samples with the silicon base (to which the

needle is mounted) is clamped to rotational stage with 30^{o} tilt angle to visualize both the Si surface and the needle face simultaneously. 3D optical measurements are then obtained for two orientations with 90° angular difference, while rotating along the needle axis. These measurements capture two adjacent side surfaces of the needle and enable measurement of angles between the Si wafer and needle surface in two orthogonal directions, which are used for compensation in the subsequent alignment steps (Figure 4.6).

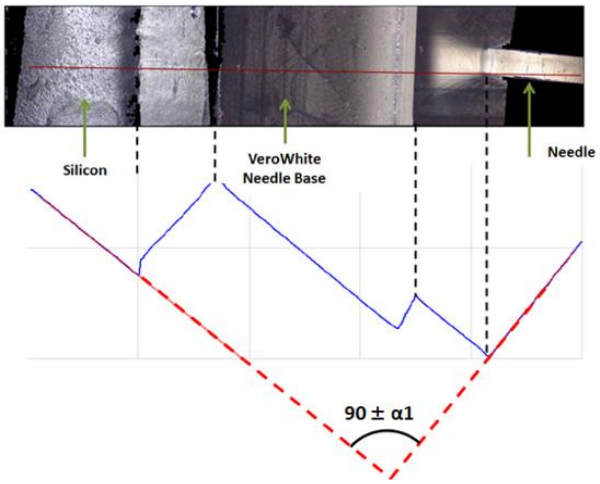

Figure 4.6: Measurement of the angular misalignment between the needle and Si-wafer using a focus variation optical microscopy.

b. Alignment of laser interferometer to the Si-chip: The Si-chip with the needle is mounted onto the sensing beam using a reference edge on the Si-wafer such that the angles measured in the previous step can be used in the subsequent alignment procedure. The smooth surface of the Si-wafer enables the alignment of the interferometer using the linear slide and goniometer. The alignment method involves changing the yaw and pitch of the goniometer to focus the laser to the surface of the Si-wafer (i.e., a maximum signal to noise ratio). The alignment is verified by moving the laser beam laterally using the linear slide to observe that the signal strength is maintained, thereby assuring that the

laser beam is perpendicular to the surface of the Si-chip. After completing the alignment, the goniometer position for the laser interferometer is retained for the last step of the alignment procedure (Figure 4.7).

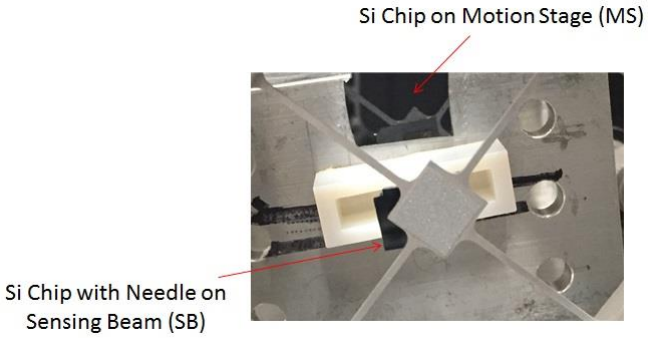

Figure 4.7: Si-chip with a pre-mounted needle on the sensing beam and another Si-chip on stage for alignment of laser.

c. Measurement of misalignment between the laser beam and *z*-axis motion of stage: Another Si-chip is mounted onto the goniometer of the needle to provide for the alignment purpose. The motion stages are moved in *x* and *y* direction such that the laser is focused on the on the Si-chip. A similar procedure explained in the previous step is executed by varying the yaw and pitch of the goniometer of the needle such that the strength of the signal obtained from the interferometer is maximized. The alignment is again confirmed by moving the linear slide of the interferometer laterally.

To measure the angle between the laser beam and the *z*-axis motion, the stage is moved in *x* and *y* directions separately to determine two orthogonal angles between the laser beam and the z-axis motion. The process is repeated until the angular misalignment is within 0.005°. The two angles are noted and along with the misalignment calculated in Step 1, both are which are used in the following steps to compensate for the overall misalignment.

d. **Misalignment correction using 3-axis motion stage:** The overall misalignment between the needle shaft and the *z*-axis motion of the stages is calculated from the previous steps. These final angles are used to obtain the orientation of a composite motion to the motion stages in *x*, *y* and *z* directions as explained in step 3 to ensure that motion is along the direction of needle as shown in Figure 4.8.

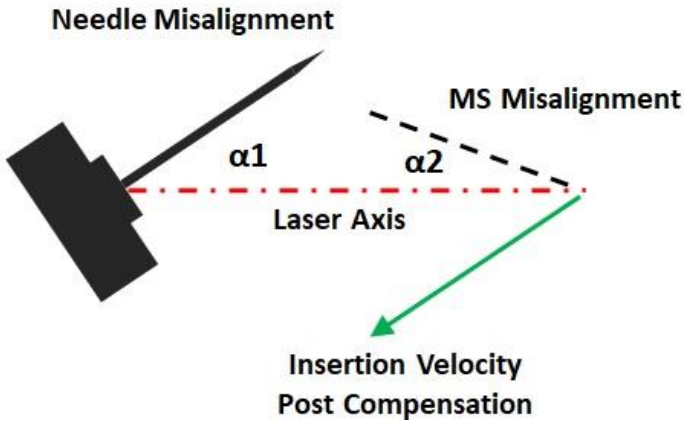

Figure 4.8: Misalignment correction using composite velocity motion of motion stages.

4.1.4 A typical insertion force profile

To describe the physical events that occur during the insertion process, a typical insertion force profile is shown in Figure 4.9. The overall force can be divided into three domains:

Dimpling: This is an initial event of the insertion force signature, where the forces increase before penetrating the tissue/phantom model. The dimpling force is due to the elastic properties of the tissue model and can be identified from pre-puncture forces in the insertion data. There are two main parameters associated with this domain: Dimpling (*PD*) and puncture force (*PF*). This initial event ends with the strain release in the tissue, which is characterized by the drop in the insertion force ER_P. The rate of increase in the insertion force in this domain is characterized by K_P. These parameters in the pre-puncture phase are mainly controlled by the tip geometry as well as by the elasticity of the tissue.

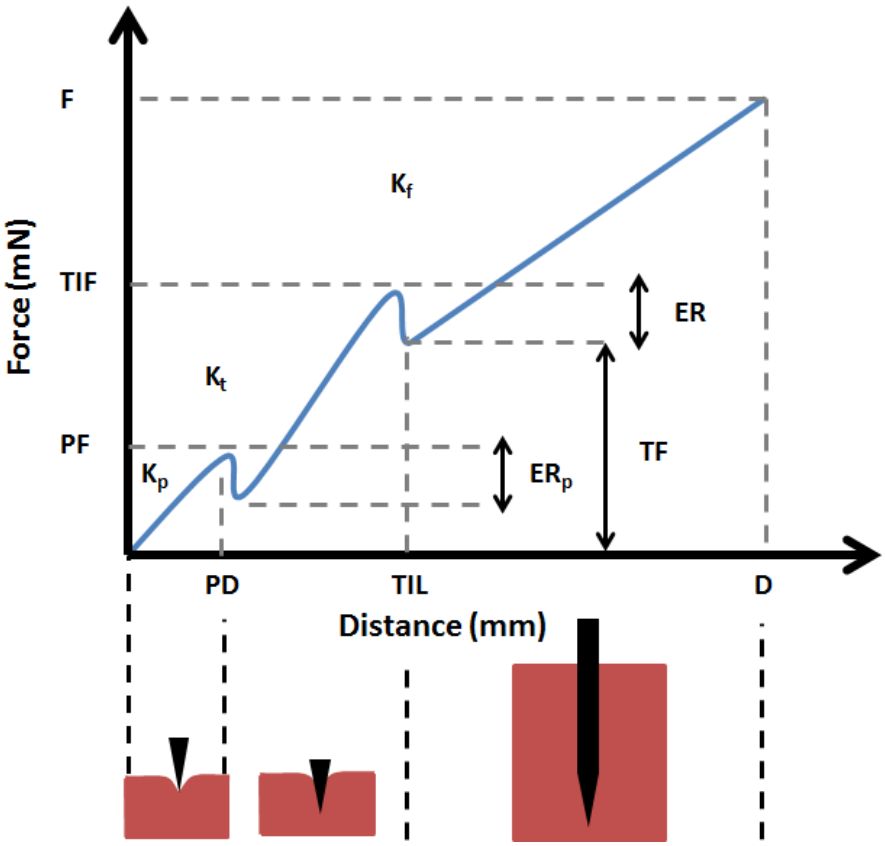

Figure 4.9: A typical insertion force profile during the interaction of the delivery vehicle with the brain tissue model.

Tip insertion: In this phase, the force increases as the needle tip penetrates the tissue. The tip displaces the tissue along its track and the rate of increase in cross section is proportional to the insertion depth. Hence, similar tip geometries with different shaft sizes are expected to follow the force profiles until the entire tip in within the tissue. Parameter K_T indicates the rate of increase of force in this domain of the force profile. *TIF* and *TIL* represent the force and displacement levels when the entire tip is completely immersed into the tissue. Tip insertion length is required to calculate the secondary dimpling (*SD*), which is calculated by subtracting the tip head length from from *TIL*. The *SD* observed in the case of sharp needle designs (pyramid and conical tip types), is larger than *PD*. Similar to *PD*, *SD* causes elastic deformation of the tissue during tip

insertion, and is an important parameter. In the case of wedge and flat tip types, *SD* is absent due to relatively high *PD* and elastic recovery (ER_P)

Shaft insertion: This is the region where the shaft enters the tissue and the forces increase linearly primarily due to the increase in friction force along the needle shaft length. Before this phase, a second drop in the force could be observed, which is shown in the Figure 4.8 as *ER*. This represents a secondary release in strains immediately after the entire tip enters the tissue.

The total tip force is characterized by *TF* and represents the total force acting on the tip region. This includes the shearing force required penetrate the underlying tissue as well as the friction and normal forces acting on the surfaces of the tip. The last parameter in this domain is the friction force which is characterized by the slope K_F as friction per unit length.

4.2 Results and Discussion

4.2.1 Non-dissolvable and dissolvable needles

Accurate fabrication of delivery vehicles is paramount to conducting reliable insertion experiments. Non-dissolvable VeroWhite and dissolvable CMC/Gluc needles with accurate dimensions are fabricated using the hybrid manufacturing technique described in Section 4.1.2. Figures 4.10 and 4.11 show the produced non-dissolvable and dissolvable needles, respectively. The geometric characterization of the produced non-dissolvable needles resulted in less than 2% and 3%, from the targeted dimensions of the measured width and apex angle (40 samples). The mean tip radius is 6.96 μm and has 21% variation (st. dev: 1.45 μm, see Figure 4.10b). Due to relatively higher mean than the targeted value (i.e. 6 μm), only needles within 1 μm of the targeted value (5 μm – 7 μm) were chosen for the insertion experiments. The overall acceptance rate based on these criteria is 62.5% while the remaining needles are discarded due to relatively blunt tips. The shrinkage for the dissolvable CMC/Glu needles is found to be less than 10%.

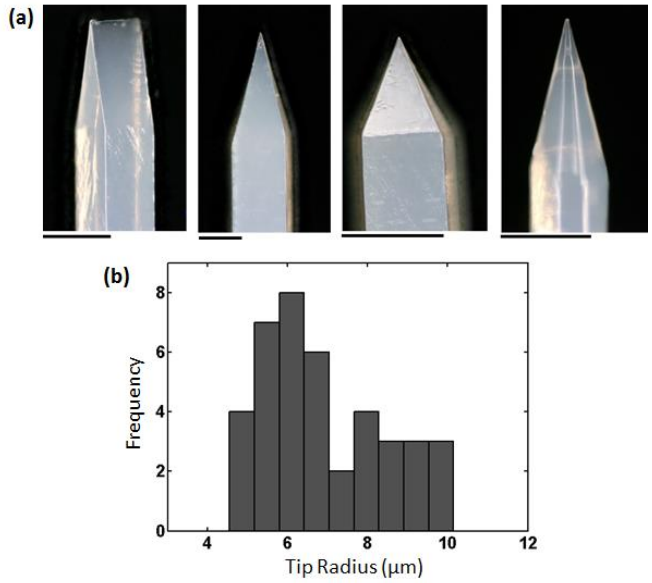

Figure 4.10: **(a)** Fabricated VeroWhite needles using a two-stage molding approach: Wedge, pyramid 30°, pyramid 45° and a 30° circular needle with conical tip. (Scale bars correspond to 250 μm). **(b)** Statistical distribution of tip radius for the fabricated VeroWhite needles

The relatively large variation in tip radius is attributed to the UV-curing and wear of production mold after demolding process. Variations in other parameters are mainly caused by shrinkage during the curing/spin-casting process. The shrinkage is minimal during UV-curing of the VeroWhite needles, since there is negligible evaporation (i.e., volume loss) during the UV-mediated cross-linking process. Conversely, there is relatively large shrinkage during fabrication of the dissolvable CMC/Gluc needles due to the evaporation of the water during the spin casting process. This shrinkage is found to be repeatable and consistent with the results reported in the literature [85-88].

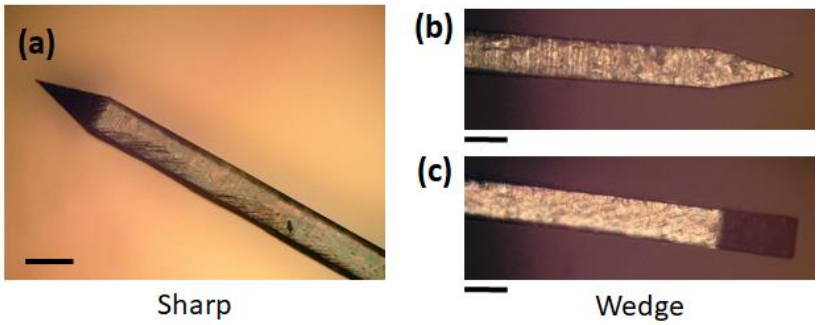

Figure 4.11: The fabricated CMC/Gluc needles. Scale bars correspond to 200 μm. **(a)** Sharp needles, **(b)** Front view and **(c)** Side view of wedge needles.

4.2.2 Repeatability analysis

To evaluate the reproducibility of the insertion force measurements, the experiments are performed using a non-dissolvable VeroWhite needle (210 µm width, 30^o angle, 6 µm tip radius) on the brain tissue phantom agarose gel at 5 mm/s insertion speed. Figure 4.12a shows a sample force profile. The parameters associated with the pre-penetration event is shown in Figure 4.12b. The initial penetration force and dimpling are found to be 0.28 mN and 120 µm, respectively. The rate of force incease K_P (stiffness of the tissue) is determined to be 2.39 N/m. The elastic recovery ER_P is determined to be 0.035 mN. These results suggest that the developed sensor is capable of detecting pre-penetration events with relatively low force magnitudes and can be effectively used to identify the parameters associated with the dimpling phase of the insertion.

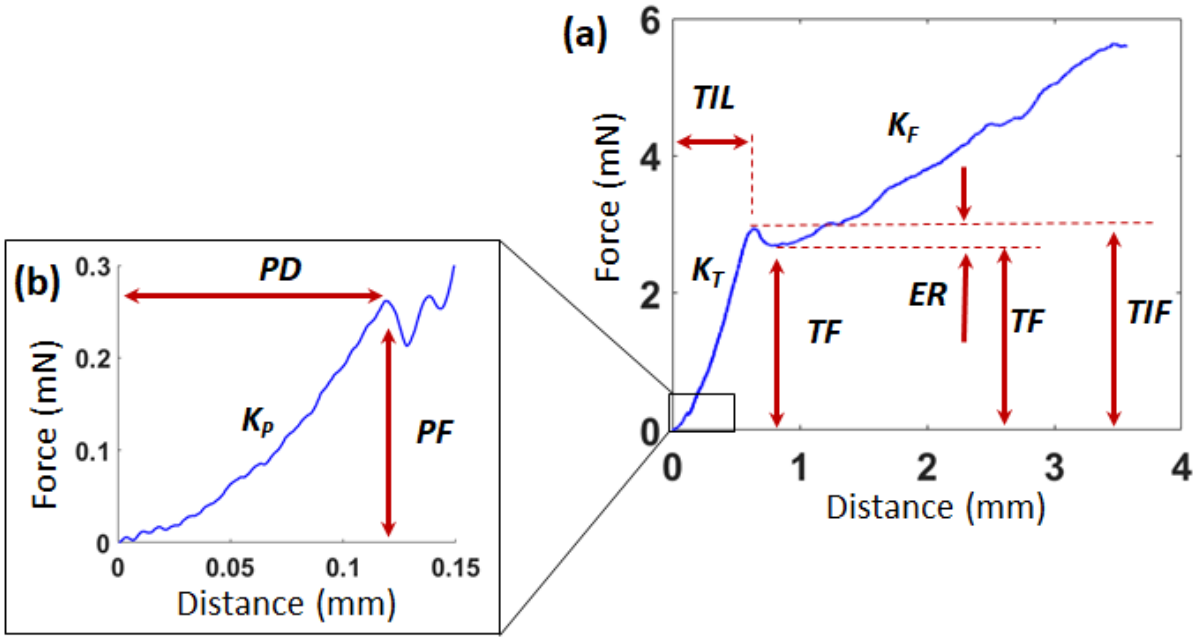

Figure 4.12: An experimentally obtained insertion force profile in agarose gel at 5mm/s. **(a)** The entire insertion force profile and **(b)** The force signature during up to the penetration.

The next phase is the tip insertion into the tissue model. In this phase, the rate of force increase is defined by K_T, which is determined to be 5.48 N/m and the complete tip immerison

(*TIL*) is observed at 621 μm, where the corresponding force *TIF* is 2.9 mN., The *TIL* parameter is used to calculate the secondary dimpling by subtracting it from tip length ,which is found to be 239 μm.

After the tip is completely immersed into the tissue, the force drop *ER* is measured to be 0.25 mN which is higher than ER_P. The final phase is the steady-state tip cutting in which the total tip force *TF* is obtained to be 2.68 mN, and the friction force per unit length K_F is found to be 1.21 N/m.

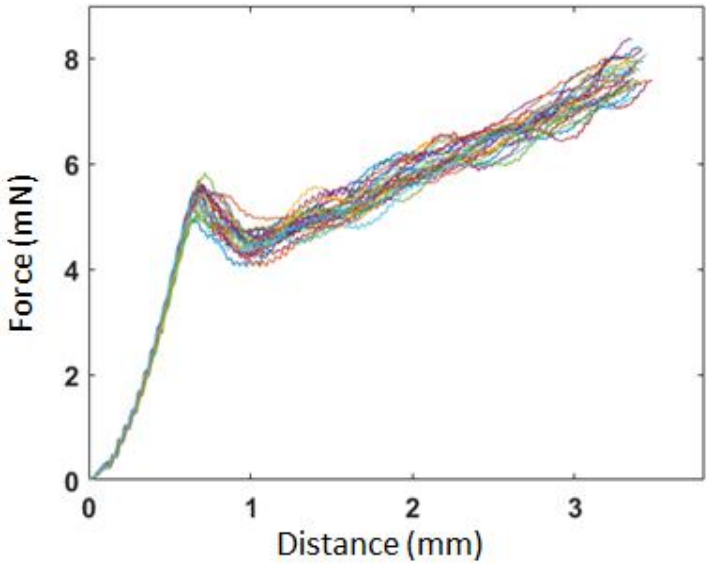

Figure 4.13: Repeatability analysis with 30 different insertion experiments.

The insertion force profiles obtained for all the 30 experiments are shown in Figure 4.13. The important parameters are extracted for all the experiments to evaluate the reproducibility of the insertion force measurements. The mean and standard deviation of each parameter are listed in Table 4.4. It is seen that the maximum percentage standard deviation (deviation/mean) of 30.1% is observed for *ER*. The other parameters with relatively high standard deviations (>5%) are K_F (8.9%) and K_P (5.9%). Based on these experiments, it is determined that sufficient levels of repeatability are observed for most of the parameters to reliably conduct insertion experiments.

Table 4.4: Reproducibility analysis of parameters with non-dissolvable needles on agarose.

	PF (mN)	*PD* (µm)	K_P(N/m)	K_T (N/m)	*TIF* (mN)	*TIL* (µm)	*ER* (mN)	*TF* (mN)	K_F (N/m)
Average	0.32	108	2.87	10.27	5.41	0.69	0.97	4.45	1.36
St. Dev	0.016	5	0.17	0.29	0.21	0.016	0.29	0.20	0.12
St. Dev (%)	5	4.6	5.9	2.8	3.9	2.4	29.9	4.6	8.9

4.2.3 Force analysis associated with the VeroWhite needles into agarose gel

Effect of insertion speed

To study the effect of insertion velocity, the experiments are performed using a VeroWhite needle with a specific design (210 µm width, 30^o angle, 6 µm tip radius) on the brain tissue phantom agarose gel at varying insertion speeds (0.3 mm/s, 1 mm/s, 5 mm/s, 15 mm/s, and 25 mm/s) with three repetitions and the insertion forces are measured. The results are plotted in Figure 4.14. In general, the overall forces increase with increase with increasing insertion velocity, which is consistent with the viscoelastic strain hardening behavior of the agarose gel reported in the literature [82]

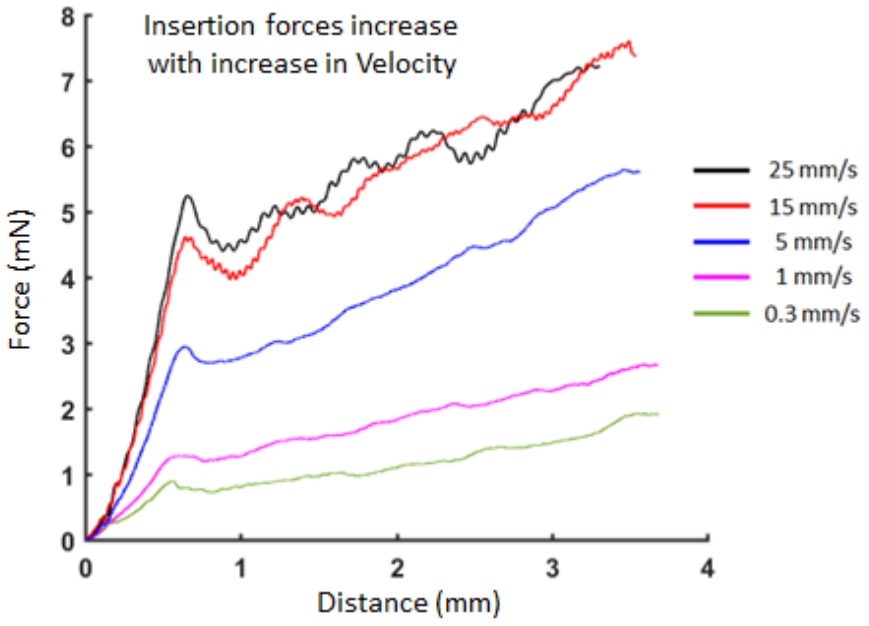

Figure 4.14: The effect of insertion speed on the insertion forces.

Effect of cross-section size

To study the effect of cross-section, the experiments are performed using square cross-section VeroWhite needles (30^{o} angle, 6 μm tip radius) with varying widths (160 μm, 210 μm, 260 μm, and 310 μm) on the brain tissue phantom agarose gel at varying insertion speeds (0.3 mm/s, 1 mm/s, 5 mm/s, 15 mm/s, and 25 mm/s) with three repetitions and the insertion forces are measured.

Figure 4.15 shows a sample insertion force plot with varying cross-sections at the speed of 5mm/s to show the effect of size on the overall force profile. As expected, the force profiles follow one another until the tip is fully immersed into the tissue.

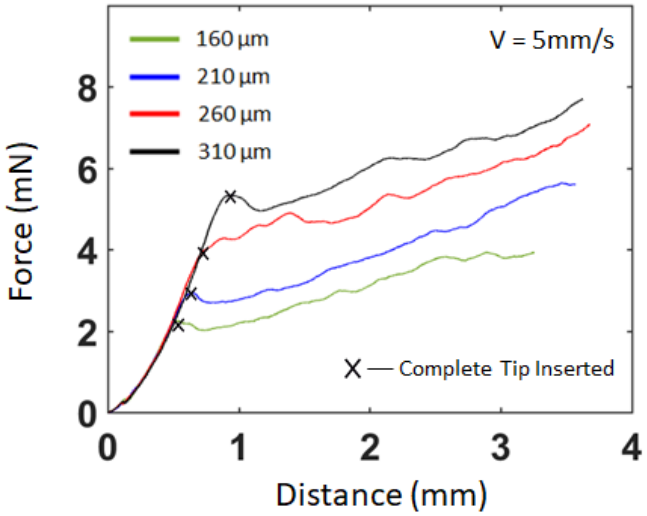

Figure 4.15: The effect of cross-section size on the insertion forces at different insertion velocities for the square cross-section needles.

A comprehensive analysis of the effect of cross-section size and insertion speed on different parameters of the insertion forces is performed and the results are shown in Figure 4.16.

Domain 1-Analysis of dimpling: Figures 4.16a, 4.16b, 4.16c show the results of analysis associated with the Domain 1. The dimpling decreases as the insertion speed is increased. Specifically, there is 33% reduction in dimpling when the insertion speed is increased from 0.3mm/s to 25 mm/s, which corresponds to about 60 μm reduction. The stiffness parameter

represented by K_P in this domain also increases with increasing speed because of viscoelastic strain hardening behavior of the tissue, which also increases the puncture/penetration force *PF*. Furthermore, there is a negligible change in dimpling with different cross-section area, which is expected since the dimpling is controlled by the tip geometry, which is same for all the designs considered in this study.

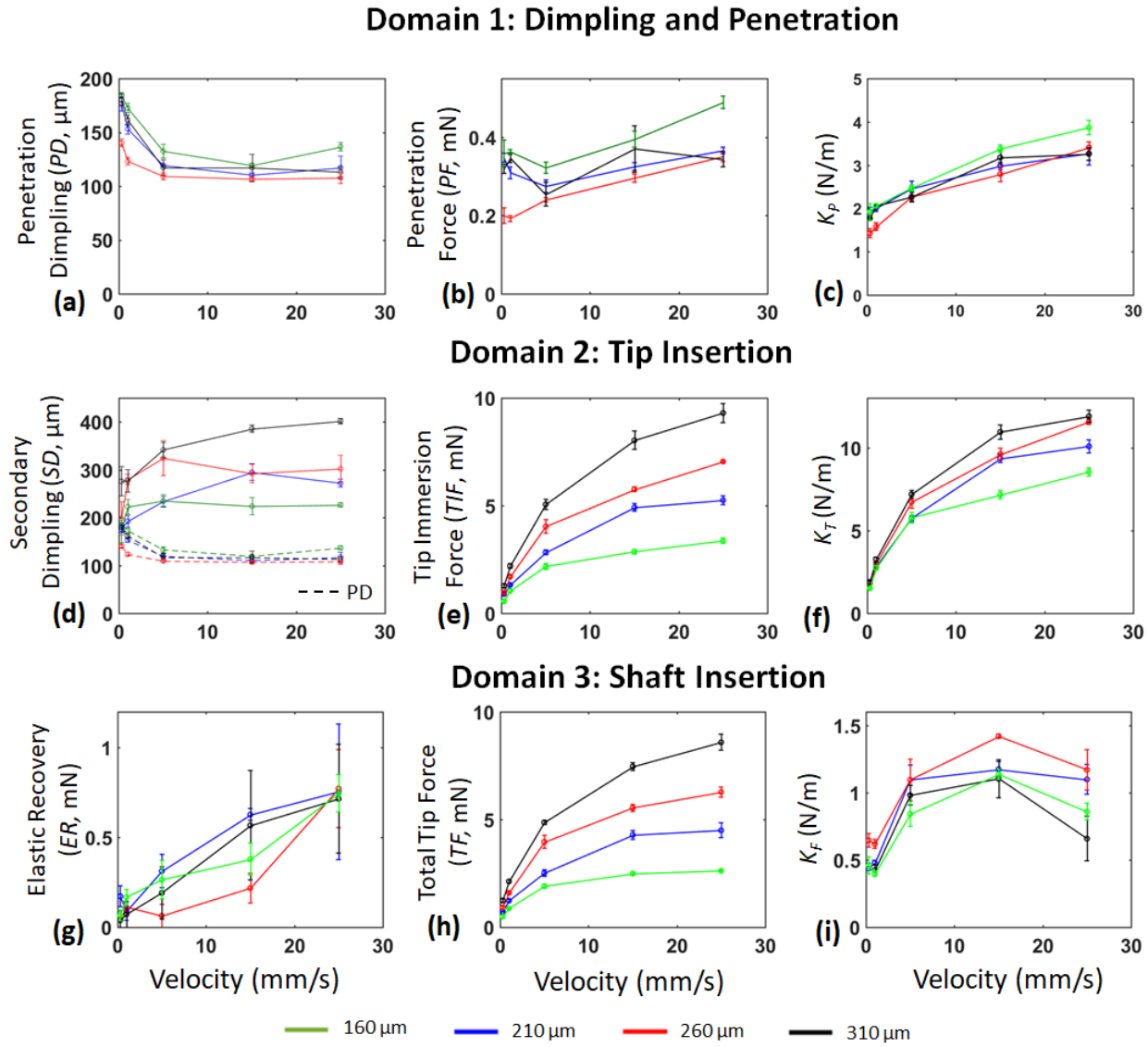

Figure 4.16: The effect of cross-section size and insertion speed on different parameters of the insertion forces with the square cross-section needles. **(a)** Penetration dimpling (*PD*), **(b)** Penetration force (*PF*), **(c)** K_P (stiffness), **(d)** Secondary dimpling and comparison with *PD* (*PD*s are the dashed lines), **(e)** Tip immersion force (*TIF*), **(f)** K_T (rate of force increase during tip insertion), **(g)** Elastic recovery (*ER*), **(h)** Total tip force (*TF*), **(i)** K_F (friction force/length).

Domain 2-Analysis of tip insertion: Figures 4.16d, 4.16e, 4.16f show the results of analysis associated with the Domain 2. As expected, the tip cutting forces are proportional to the cross-section area and have an increasing trend, and in turn, the *TIF* increases with increasing cross-section area. The other two parameters *SD* (Figure 4.16d) and K_T (Figure 4.16f) also show mainly increasing trends with increasing speed and cross-section area. The observed increasing trends of the insertion force parameters in this phase are expected due to the increasing displaced area with relatively larger tips and strain hardening of the tissue. It is noted that *SD* is found to be larger than *PD*, which is shown with the dashed lines in Figure 4.16d.

Domain 3-Steady-state shaft insertion: Figures 4.16g, 4.16h, 4.16i show the results of analysis associated with the Domain 3. As indicated by the repeatability analysis in Section 4.3.2., elastic recovery (*ER*, Figure 4.16g) shows relatively large variation with respect to other parameters. In general, *ER* increases with increasing speed, whereas there is no clear trend in the change of *ER* with varying cross-section area. Tip forces (*TF*s, Figure 4.16h) are proportional to the speed and shows an increasing trend due to the strain hardening of tissue. Furthermore, while *TF*s are comparable to friction forces when relatively smaller size needles (< 250 μm) are used, they are relatively larger than friction forces, especially when relatively larger needles (> 250 μm) are used at high velocities (>5 mm/s). K_F, which is an indicator of the friction force, is found to increase when the cross-section size is increased from 160 μm to 260 μm. However, the further increase in the cross-section area (e.g., 310 μm) results in negligible changes in K_F. It is also seen that, when the friction force increases up to the insertion speed of 15 mm/s, whereas it decreases when the speed is increased from 15 mm/s to 25 mm/s for the all the cross-section sizes considered in this study.

Effect of tip radius

To study the effect of tip radius, the experiments are performed using square cross-section VeroWhite needles (30^o angle, 210 µm width) with varying tip radii (6 µm and 15 µm) on the brain tissue phantom agarose gel at varying insertion speeds (0.3 mm/s, 1 mm/s, 5 mm/s, 15 mm/s, and 25 mm/s) with three repetitions and the insertion forces are measured. Figure 4.17 (a) shows the insertion forces obtained when using the needles with 15 µm tip radius at varying insertion velocities. At relatively low velocities (0.3mm/s and 1mm/s), tissue dragging is observed due to the blunt nature of the needles. The favorable insertion conditions should be identified to avoid the tissue dragging. Figure 4.17 (b) shows the insertion forces obtained with the needles with both 6 µm and 15 µm tip radii. As expected, there is a larger dimpling with increasing tip radius.

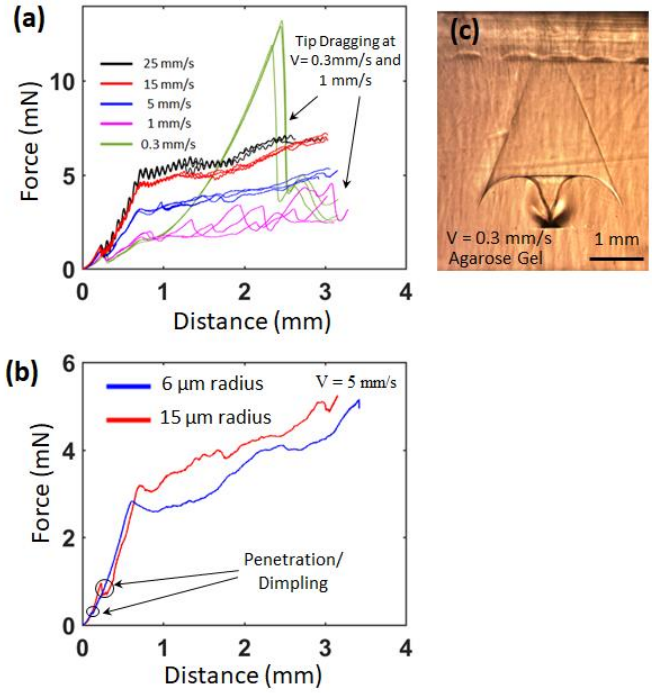

Figure 4.17: Insertion forces at different velocities with 15 µm diameter needle tip. **(a)** Insertion force profile for VeroWhite (210 µm, pyramid tip, 30^o angle and 15 µm tip radius) needle into agarose gel all insertion velocities, **(b)** Insertion force comparison between 15 µm and 6 µm tip radius at insertion speeds of 5 mm/s, **(c)** An image showing tissue dragging at insertion speed of 0.3 mm/s (The needle was retracted from agarose).

A comprehensive analysis of the effect of tip radius on different parameters of the insertion forces is performed and the results are shown in Figure 4.17.

The tip radius mainly controls the dimpling phases. Both the primary and secondary dimpling amounts increase with increasing tip radius (Figure 4.18a). Specifically, the *PD* and *SD* amounts with the relatively blunt needles are approximately 2 times higher than that with the sharper needles. Similarly, K_P increases when the relatively blunt needles are used due to the increased strain hardening effect at relatively larger surface of the blunt tips (Figure 4.18b).

The tip radius significantly affects the elastic recovery post penetration (ER_P, Figure 4.18c). The difference between sharp and blunt tips could be as large as 12-fold increase with relatively blunt needles at higher speeds.

The tip radius also affects the tip forces (*TF*), especially at relatively low speeds (Figure 4.18d). While the difference is as large as 80% between the forces obtained with sharp and blunt tips at low speeds, this difference is negligible at relatively high insertion velocities (>1mm/s), which is attributed to the difference in the cutting mechanisms at low and high velocities for the blunt needles.

The penetration forces (*PF*) are directly affected by the tip radius (Figure 4.18d). Specifically, *PF* with the blunt needles are approximately about 3 times higher than those with the sharp needles. *PF* is still significantly (i.e., 4.2 times) lower than total *TF*.

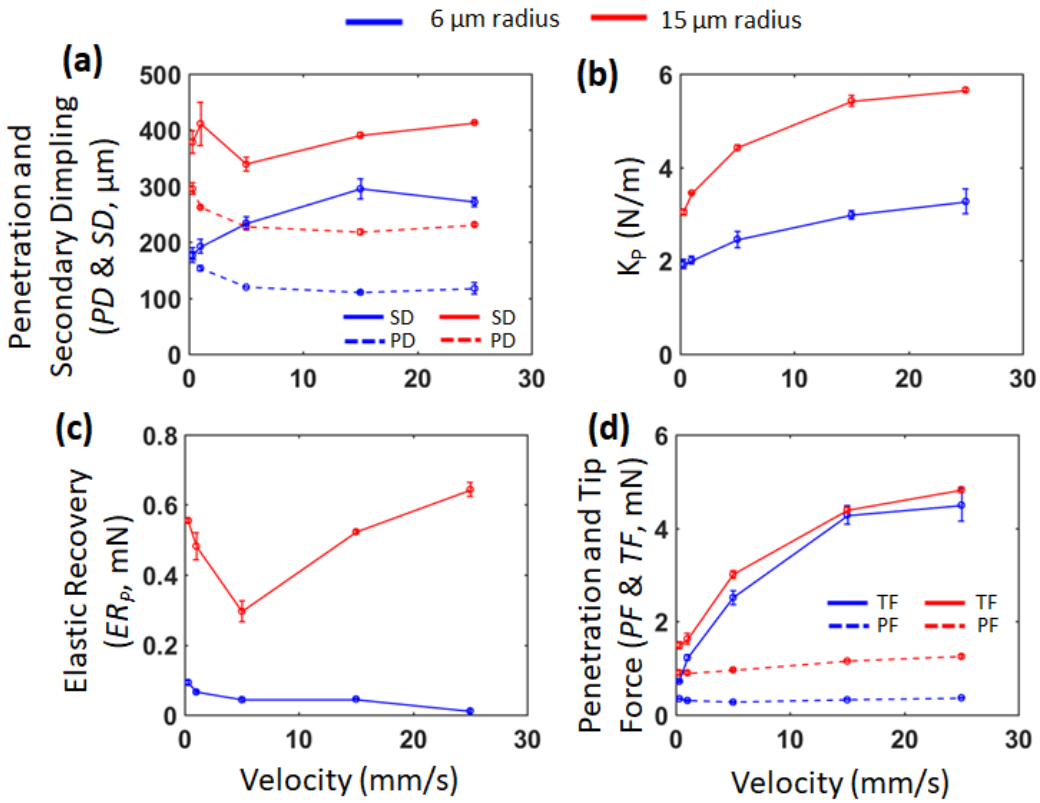

Figure 4.18: The effect of tip radius on different parameters of the insertion forces. **(a)** Primary dimpling (*PD*) and secondary dimpling (*SD*) (*PD*s are the dashed lines), **(b)** K_P (stiffness), **(c)** Elastic recovery (ER), **(d)** Penetration force (*PF*) and tip forces (*TF*) (*PF*s are in dashed lines).

Effect of apex angle

To study the effect of apex angle, the experiments are performed using square cross-section VeroWhite needles (210 µm width, 6 µm tip radius) with varying tip angle (30 ^{o} and 45^{o}) on the brain tissue phantom agarose gel at varying insertion speeds (0.3 mm/s, 1 mm/s, 5 mm/s, 15 mm/s, and 25 mm/s) with three repetitions and the insertion forces are measured. Figure 4.19a shows the insertion forces obtained when using 45^{o} needles at varying insertion velocities. The tissue dragging is observed at velocities lower than 1 mm/s. Figure 4.19b shows the insertion forces obtained with the needles with both 30^{o} and 45^{o} apex angle. As expected, the penetration and tip cutting forces are largely affected by the apex angle.

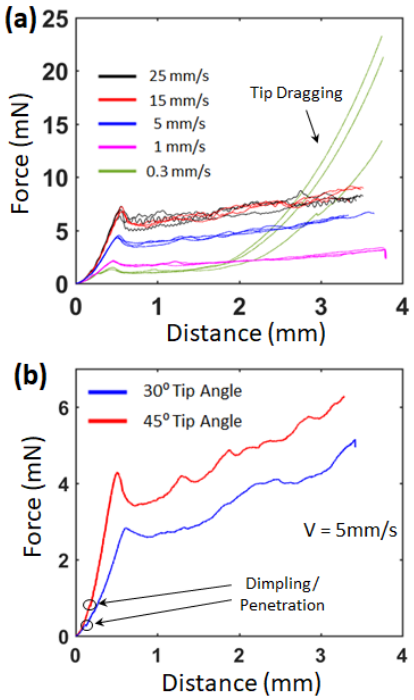

Figure 4.19: The effect of apex angle on different parameters of the insertion forces. (a) Insertion force profile for VeroWhite (210 µm, pyramid tip, 45° angle and 6 µm tip radius) needle into agarose gel all insertion velocities, (b) Insertion force comparison between 45° and 30° tip angle at insertion speeds of 5 mm/s.

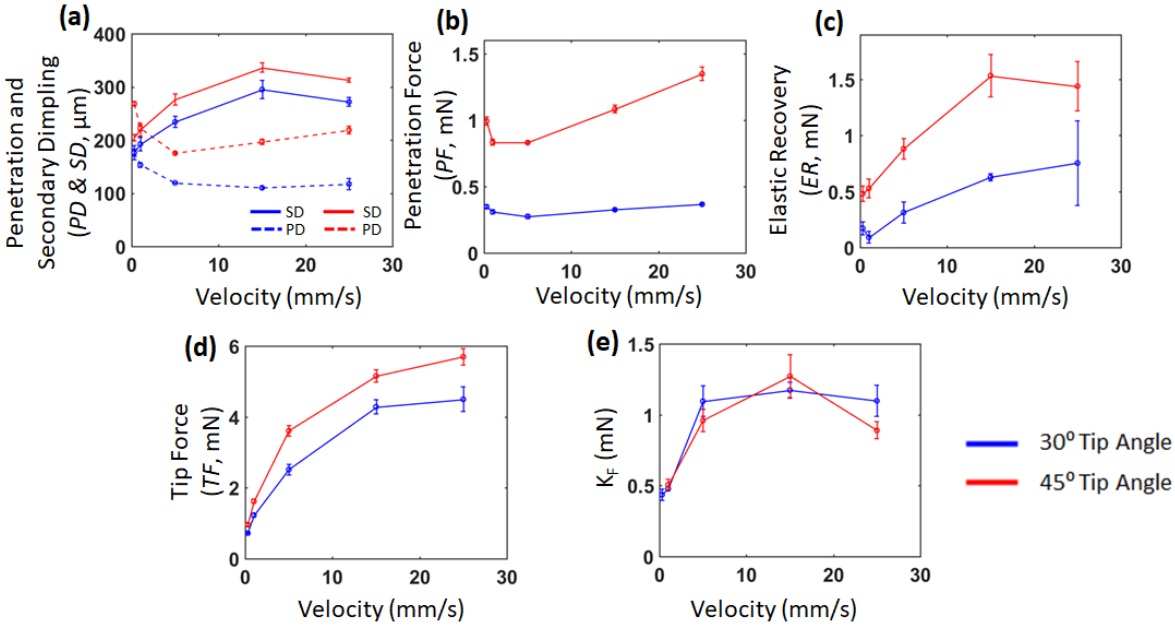

Figure 4.20: The effect of apex angle on different parameters of the insertion forces. **(a)** Penetration dimpling (*PD*) and secondary dimpling (*SD*) (*PD*s are dashed lines), **(b)** Penetration force (*PF*), **(c)** Elastic recovery (*ER*), **(d)** Total tip force (*TF*), **(e)** K_F (friction force/length)**.**

A comprehensive analysis of the effect of apex angle on different parameters of the insertion forces is performed and the results are shown in Figure 4.20. The apex angle significantly affects the first and secondary dimpling amounts. Both *PD* and SD increase with increasing apex angle (Figure 4.20a), and the increase in *PD* is relatively larger.

The penetration forces (*PF*) increase with increasing apex angle (Figure 4.20b). Specifically, the *PF* obtained with the 45^o needles is approximately 2.5 times higher than those obtained with the 30^o needles. Furthermore, the rate of increase in *PF* with increasing speed is larger with the 45^o needles, thereby indicating the dependence of strain hardening on the apex angle. The increased strain hardening effect with increasing apex angle was reported in the literature as strain rate being directly proportional to tangent of the tip angle (tan(α)), as well as insertion speed [49]. That would result in higher strain rates for higher tip angle at the same velocity. This also increases the ER with increasing apex angle (Figure 4.20c).

The tip forces (*TF*) are also affected by the apex angle. There is more than 30% increase in *TF* when the apex angle is changed from 30^o and 45^o (Figure 4.20d) due to the strain hardening effect.

The change in friction force with varying apex angle is negligible (Figure 4.20e). This is expected since the shanks of the used needles have the same surface area.

Effect of tip type

To study the effect of tip type, the experiments are performed using square cross-section VeroWhite needles (210 μm width) with varying tip types (pyramid with 30° apex angle and 6 μm tip radius, wedge with 30° angle and 6 μm tip radius, and flat) on the brain tissue phantom agarose gel at varying insertion speeds (0.3 mm/s, 1 mm/s, 5 mm/s, 15 mm/s, and 25 mm/s) with three repetitions and the insertion forces are measured.

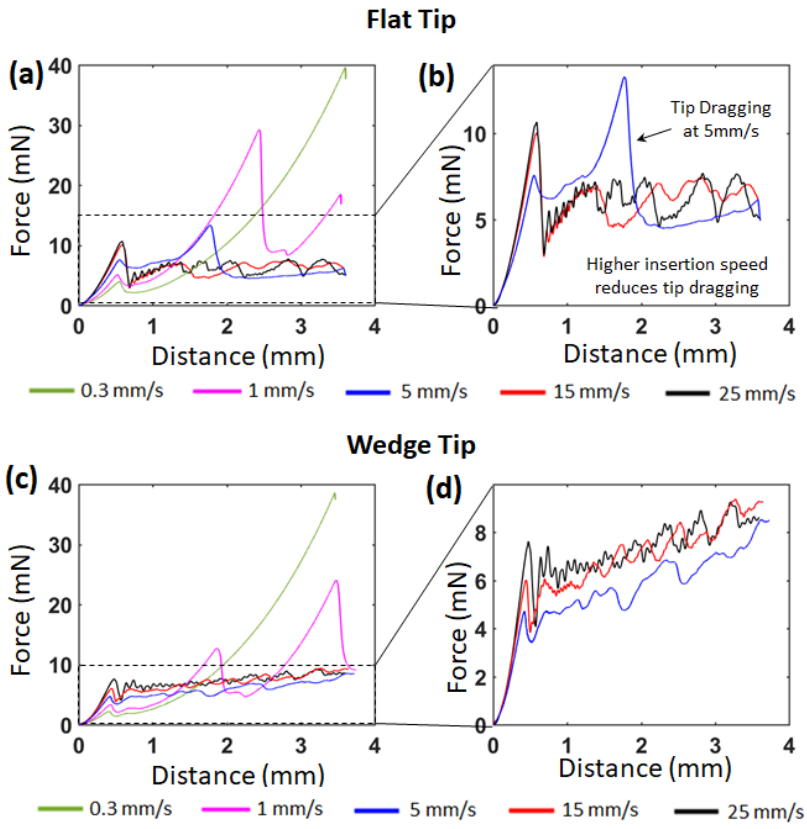

Figure 4.21: The effect of tip type on the insertion forces at varying insertion speeds. **(a)** Insertion force profile for VeroWhite (210 µm and flat tip) needle into agarose gel all insertion velocities, **(b)** Zoomed in forces for flat needles at 5, 15 and 25 mm/s **(c)** Insertion force profile for VeroWhite (210 µm, wedge tip and 30° angle) needle into agarose gel all insertion velocities, **(d)** Zoomed in forces for flat needles at 5, 15 and 25 mm/s. Tissue dragging and subsequent release is represented by cyclic oscillations.

Figure 4.21a and 4.21b show the insertion forces with the flat needles at different insertion speeds. The insertion forces are relatively lower at higher speeds despite the higher strain hardening effect (Figure 4.21a). The frequency of cyclic oscillation observed in the forces decreases with increasing speed (Figure 4.21b). These oscillations represent the repeated dragging event and resulting release of the tissue model. Similar conclusions can be drawn for the wedge type needle (Figures 4.21c and 4.21d).

A comprehensive analysis of the effect of tip type on different parameters of the insertion forces is performed and the results are shown in Figure 4.22.

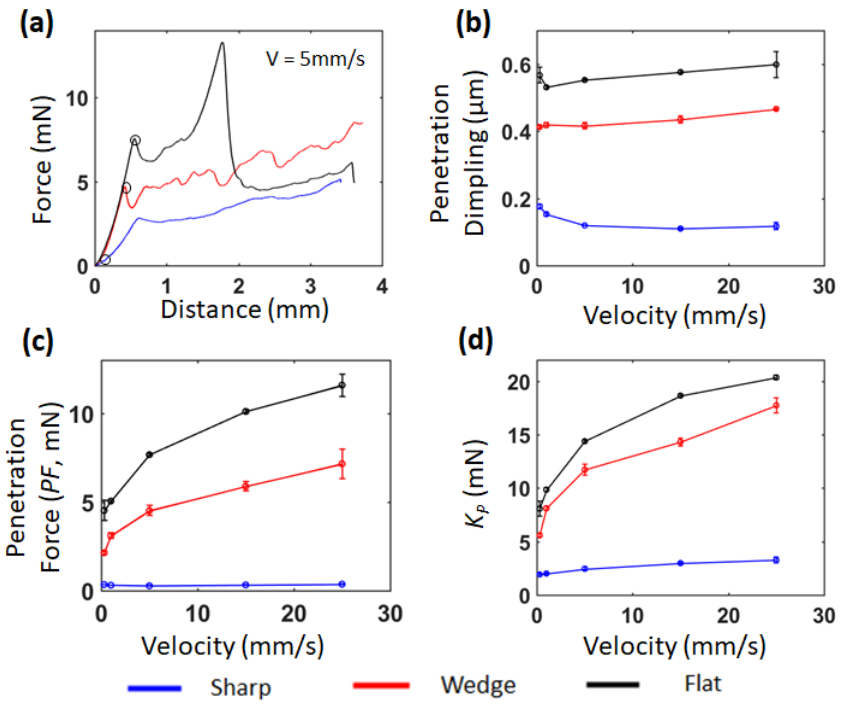

Figure 4.22: The effect of tip type on different parameters of the insertion forces. **(a)** Insertion force comparison between sharp, wedge and flat tips at insertion speeds of 5 mm/s **(b)** Penetration dimpling (*PD*), **(c)** Penetration force (*PF*), **(d)** K_P (stiffness).

The tip type affects the dimpling and penetration forces and the blunt tips (i.e., the wedge and flat tips) result in relatively higher dimpling and penetration forces due to increase in surface area at the tips (Figures 4.22a, 4.22b, and 4.22c).

The stiffness parameter K_P also increases with tip bluntness (Figure 4.22d). Furthermore, the increase in K_P with increasing speed is 69%, 217% and 151% for the sharp, wedge and flat tips, respectively. Unlike the sharp tip design, flat and wedge tips have unsteady tip and friction forces caused by tissue dragging (and subsequent release), and are not compared to *TF* and K_F obtained from the sharp tip insertion experiment.

Effect of cross-section shape

To study the effect of cross-section shape, the experiments are performed using VeroWhite needles (constant cross-section area (or shank volume), 30° apex angle, 6 μm tip radius) with varying cross-section type (square (210 μm), circular (235 μm diameter) and rectangular (160 μm

x 240 µm)) on the brain tissue phantom agarose gel at varying insertion speeds (0.3 mm/s, 1 mm/s, 5 mm/s, 15 mm/s, and 25 mm/s) with three repetitions and the insertion forces are measured.

An analysis of the effect of cross-section shape on different parameters of the insertion forces is performed and the results are shown in Figure 4.23.

The secondary dimpling SD is affected by the cross-section shape. Specifically, *SD* with the circular shape is 27% and 6.5% lower than the *SD* with the square shape at 5 mm/s and 25 mm/s, respectively (Figure 4.23a).

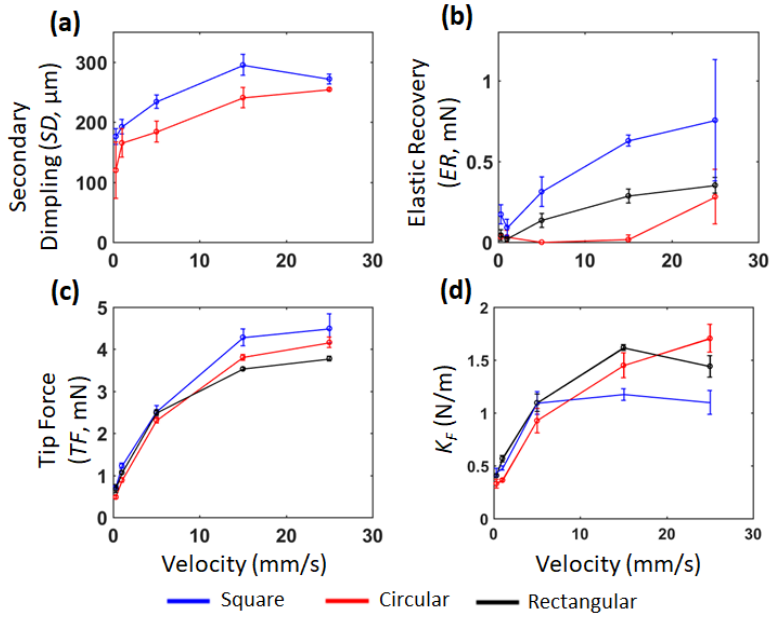

Figure 4.23: The effect of cross-section shape on different parameters of the insertion forces. **(a)** Secondary dimpling (*SD*), **(b)** Elastic recovery (*ER*), **(c)** Total tip force (*TF*), **(d)** K_F (friction force/length).

The elastic recovery is also a function of cross-section type (Figure 4.23b). The square needles exhibit larger *ER* than circular- (38 times higher at 15mm/s) and rectangular (2.3 times higher at 15 mm/s) needles. This suggests that the circular and rectangular cross-sections have smoother transition from tip region to the shank of the needle as compared to the square-shaped needles

The the tip and friction forces are not strongly affected by the cross-section type, especially at lower speeds. For instance, circular and rectangular designs have lower tip forces as compared to the square needles at higher velocities, whereas there is negligible difference at lower velocities (Figure 4.23c). In the case of friction forces, circular design has higher friction forces at higher velocity and neglibile difference at lower velocity(Figure 4.23d).

4.2.4 Force analysis associated with the CMC/Glu needles into agarose gel

To study the effect of dissolvable material, the experiments are performed using square cross-section CMC/Glu needles (30° apex angle, 210 μm width, 6 μm tip radius) on the brain tissue phantom agarose gel at varying insertion speeds (0.3 mm/s, 1 mm/s, 5 mm/s, 15 mm/s, and 25 mm/s) with three repetitions and the insertion forces are measured. Both the sharp and wedge needles are used for these experiments. The insertion forces obtained with the dissolvable needles compared with those with the non-dissolvable needles from the previous section.

Sharp Needles

Figure 4.24a shows the effect of insertion velocity on insertion forces for dissolvable pyramid tip needles. The obtained insertion force profiles are similar to those with the non-dissolvable needles at relatively high velocities (>5 mm/s), whereas they significantly vary at low speeds (Figures 4.24b and 4.24c). For instance, at the insertion speeds of 0.3 mm/s and 1 mm/s, the dimpling and puncture forces are significantly higher than those obtained with the non-dissolvable VeroWhite needles. Furthermore, unlike non-dissolvable needles, when the dissolvable needles are used at relatively low speeds (<5 mm/s), there is large elastic release. This is attributed to the blunting of the dissolvable needles as they penetrate to the aqueous environment at low speeds, thereby increasing the surface area of the tips. The blunt tips result in relatively higher puncture forces and dimpling at low insertion velocities (Figure 4.24). On the

other hand, at higher velocities, the entire insertion event is so fast that the needle absorbs negligible moisture, thereby behaving similar to the non-dissolvable needles. These findings should be considered to mitigate the drawbacks of high dimpling and puncture force due to the blunting of tip sharpness. For example, based on these results, a minimum insertion velocity of 5mm/s can be used with the dissolvable needles with 6 μm tip radius to avoid blunting of the needle tips.

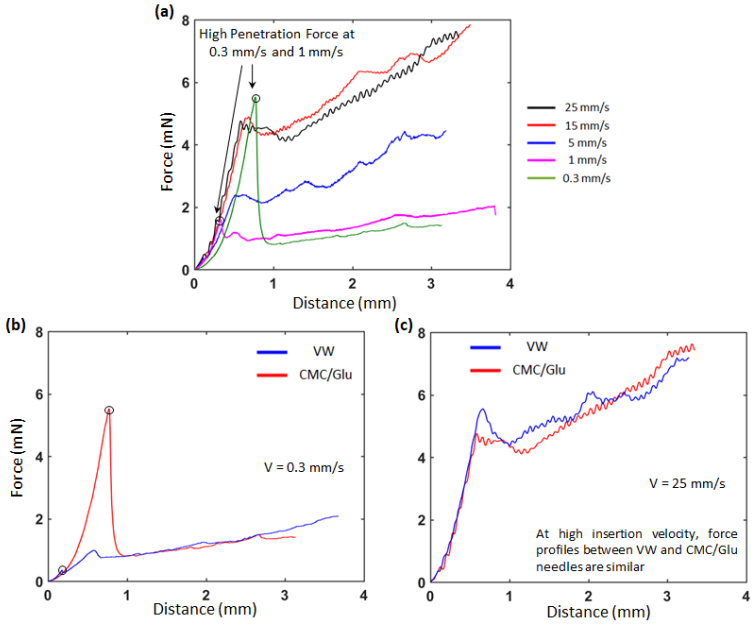

Figure 4.24: The effect of needle material on the insertion forces at varying insertion speeds. **(a)** Insertion force profile for CMC/Glu (210 μm, 30° angle, pyramid tip and 6 μm radius) needle into agarose gel all insertion velocities, **(b)** Insertion force comparison between CMC/Glu and VeroWhite at insertion speeds of 0.3 mm/s and, **(c)** 25 mm/s (Penetrations points are marked with a circle).

Wedge needles

Figure 4.25a shows the effect of insertion velocity on insertion forces for dissolvable wedge tip needles. Similar to the sharp tip needles, the obtained insertion force profiles are similar to those with the non-dissolvable needles at relatively high velocities, whereas they significantly vary at low speeds (Figures 4.25b and 4.25c). However, as compared to sharp pyramid tip shape,

the wedge tip needle has a minimum insertion velocity of 15mm/s to avoid blunting of the needle tips, thereby resulting in force profiles similar to those with the non-dissolvable needles.

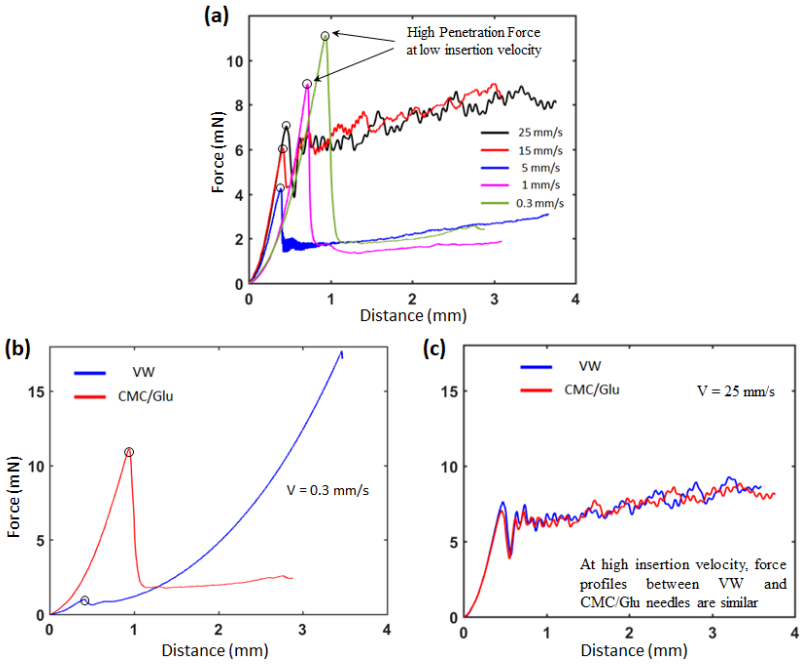

Figure 4.25: The effect of needle material on the insertion forces at varying insertion speeds. **(a)** Insertion force profile for CMC/Glu (210 µm, 30° angle, wedge tip) needle into agarose gel all insertion velocities**, (b)** Insertion force comparison between CMC/Glu and VeroWhite at insertion speeds of 0.3 mm/s and, **(c)** 25 mm/s (Penetrations points are marked with a circle).

4.2.5 Force analysis associated with the non-dissolvable needles into brain tissue

To study the force signature in actual brain tissue with non-dissolvable needles, the experiments are performed using square cross-section VeroWhite needles (30° apex angle, 210 µm width, 6 µm tip radius) on the rat brain tissue at varying insertion speeds (0.3 mm/s, 1 mm/s, 5 mm/s, 15 mm/s, and 25 mm/s) with three repetitions and the insertion forces are measured. Both the sharp and wedge needles are used for these experiments. The insertion forces obtained on the brain tissue are compared with those obtained on the brain tissue phantom model agarose gel.

Sharp needles

Figure 4.26a shows the effect of insertion velocity on insertion forces for non-dissolvable pyramid tip needles in the brain tissue. Figure 4.26b shows the comparison of the insertion forces obtained in the brain tissue with those obtained in the brain tissue model agarose when inserted at 5 mm/s. As seen in the agarose gel, the forces increase with increasing speed due to the strain hardening effect (Figure 4.26a). However, there are significant differences between the insertion forces obtained in brain tissue and those obtained in the agarose phantom model (Figure 4.26b). The decrease in force around observed after 2.5 mm of penetration depth is due to the difference in mechanical property of grey and white matter. The transition from grey to white matter in rat brain occurs around 2.5 mm to 3mm from the surface and a similar decrease in force due to such transition has been reported in literature [52].

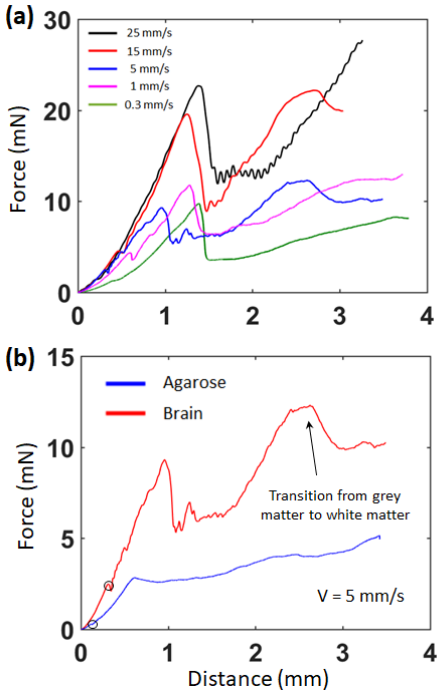

Figure 4.26: Insertion forces when non-dissolvable sharp needles are inserted into the brain tissue: **(a)** Insertion force profile for VeroWhite (210 µm, 30° angle, pyramid tip and 6 µm radius) needle into brain tissue all insertion velocities, **(b)** Insertion force comparison between Brain and Agarose at insertion speeds of 5 mm/s. (Circle represent the penetrations points)

An analysis of the effect of insertion speed on the insertion forces with non-dissolvable needles is performed and the results are shown in Figure 4.27.

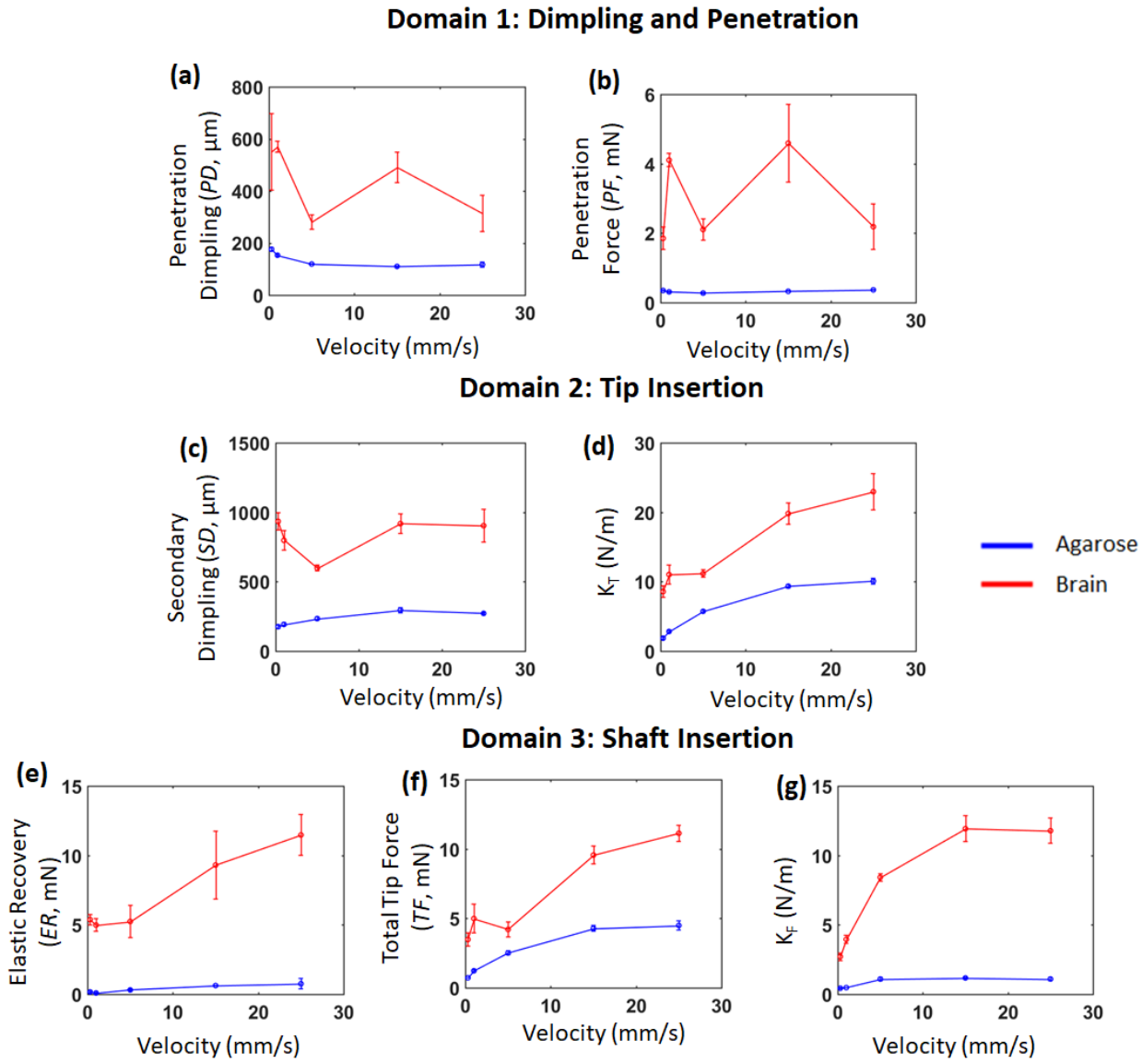

Figure 4.27: Effect of velocity on different insertion force parameters for VeroWhite (210 µm, 30° angle, pyramid tip and 6 µm radius) needle insertion into brain tissue. These parameters are also compared with corresponding parameters obtained from insertion into agarose. **(a)** Penetration dimpling (*PD*), **(b)** Penetration force (*PF*), **(c)** Secondary dimpling (*SD*), **(d)** K_T (rate of force increase during tip insertion), **(e)** Elastic recovery (*ER*), **(f)** Total tip force (*TF*), **(g)** K_F (friction force/length).

The magnitudes of individual parameters are much higher in brain than in agarose. Furthermore, there is a relatively large deviation in individual parameters of insertion force

profiles obtained in the actual brain tissue as compared to those obtained in the agarose gel (comparison of Figure 4.16 and Figure 4.27). These differences between the insertion forces obtained in brain tissue and those obtained in agarose gel could be attributed to the differences in physical properties of brain tissue and agarose gel. For instance, relatively larger deformation of the brain tissue in pre-penetration and full tip insertion events (i.e., relatively higher primary and secondary dimpling amounts, Figures 27a and c) occurs due to the elastic arachnoid layer which is composed of collagen and elastic fibers, and much more elastic than agarose gel [91]. Despite the differences in magnitudes of all the insertion force parameters obtained in brain tissue and agarose gel, the trends with increasing speed are similar in both brain tissue and agarose gel, except the initial pre-penetration domain.

Wedge needles

Figure 4.28a shows the effect of insertion velocity on insertion forces for non-dissolvable wedge tip needles in the brain tissue. Figure 4.28b shows the comparison of the insertion forces obtained in the brain tissue with those obtained in the brain tissue model agarose when inserted at 5 mm/s. As seen in the agarose gel, the forces increase with increasing speed due to the strain hardening effect (Figure 4.28a). However, there are significant differences between the insertion forces obtained in brain tissue and those obtained in the agarose phantom model (Figure 4.28b).

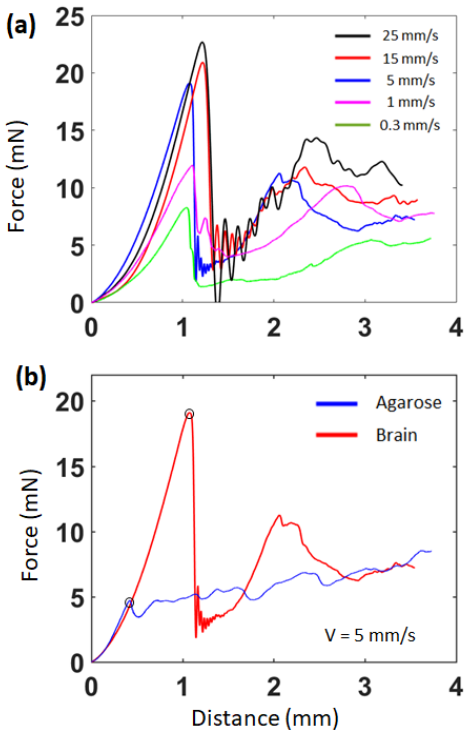

Figure 4.28: Insertion forces when non-dissolvable wedge needles are inserted into the brain tissue:**(a)** Insertion force profile for VeroWhite (210 µm, 30° angle, pyramid tip and 6 µm radius) needle into brain tissue all insertion velocities, **(b)** Insertion force comparison between Brain and Agarose at insertion speeds of 5 mm/s. (Oscillations observed at 25 mm/s is due to sensor ringing effect; Penetrations points are marked with a circle).

As seen in sharp non-dissolvable needles, the magnitudes of individual parameters are much higher in brain tissue than in agarose gel. Furthermore, the individual parameters of the insertion forces increase with increasing speed, except the pre-penetration dimpling amount (*PD*) (Figure 29a). Interestingly, the pre-penetration dimpling amount is constant with increasing speed. Based on these results, a velocity of 5mm/s is suggested to lower the insertion forces while avoiding any tissue dragging.

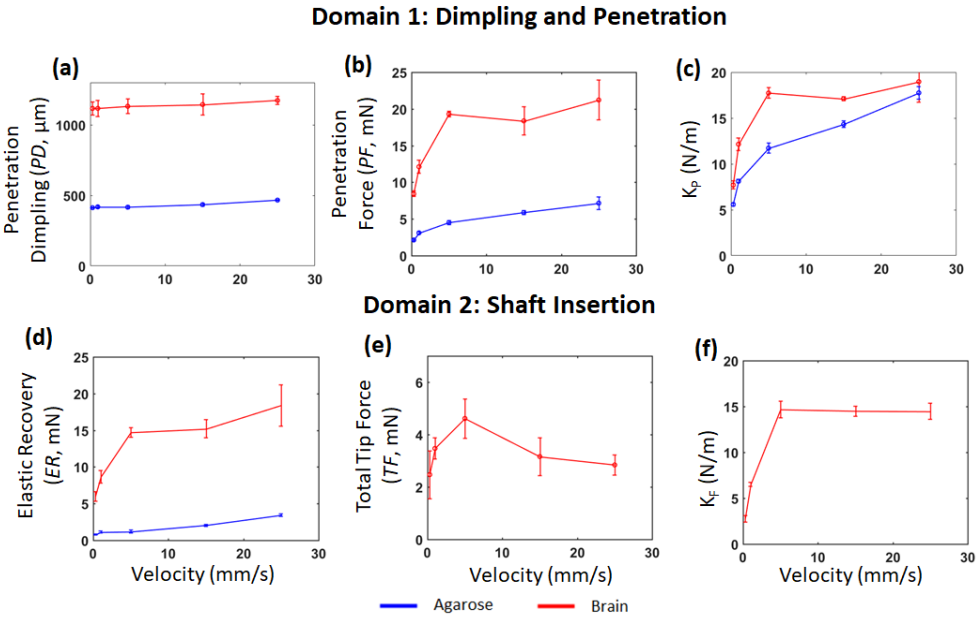

Figure 4.29: Effect of velocity on different insertion force parameters for VeroWhite (210 µm width, 30° angle, wedge tip) needle insertion into brain tissue. These parameters are also compared with corresponding parameters obtained from insertion into agarose gel. **(a)** Penetration dimpling (*PD*), **(b)** Penetration force (*PF*), **(c)** K_P (stiffness), **(d)** Elastic recovery (*ER*), **(e)** Total tip force (*TF*), **(f)** K_F (friction force/length).

Figure 4.30 compares the major parameters of the insertion forces obtained with the sharp and wedge designs in the rat brain tissue. The penetration and friction forces (Figures 4.30a and b) are relatively larger with sharp designs, whereas elastic recovery (Figure 4.30c) post complete tip immersion is higher with the wedge design, especially at high speeds.

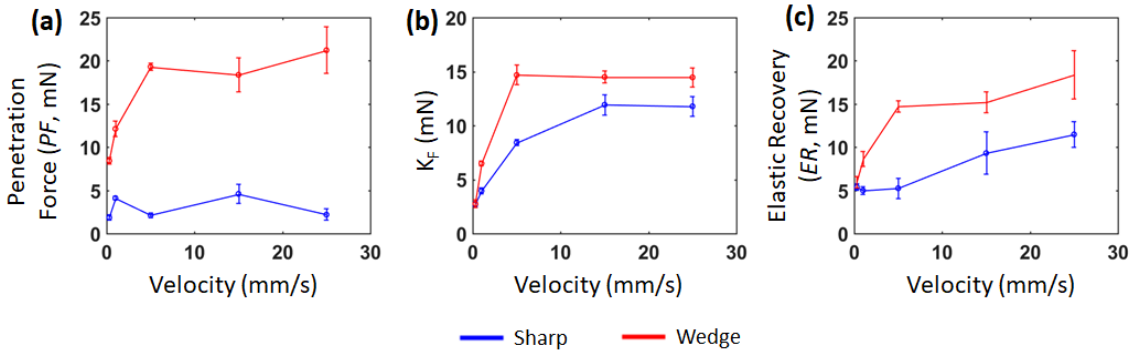

Figure 4.30: Effect of sharp (6 µm tip radius) and wedge tip-type on different insertion force parameters for VeroWhite (210 µm, 30° angle) needle insertion into brain tissue. **(a)** Penetration force (*PF*), **(b)** K_F (friction force/length), **(c)** Elastic recovery (ER_P from wedge and *ER* from sharp needle designs are compared).

4.2.6 Force analysis associated with the dissolvable needles into brain tissue

To study the force signature in actual brain tissue with dissolvable needles, the experiments are performed using square cross-section CMC/Gluc needles (30° apex angle, 210 μm width, 6 μm tip radius) on the rat brain tissue at varying insertion speeds (0.3 mm/s, 1 mm/s, 5 mm/s, 15 mm/s, and 25 mm/s) with three repetitions and the insertion forces are measured. Both the sharp and wedge needles are used for these experiments. The insertion forces obtained on the brain tissue are compared with those obtained on the brain tissue phantom model agarose gel.

Wedge needles

Figure 4.31 shows the effect of insertion velocity on insertion forces for dissolvable wedge tip needles in the brain tissue. Both the penetration and overall forces are higher at lower velocities.

Analysis of different parameters (Figures 4.32a and b) shows that both dimpling, and penetration forces are higher at low velocities as compared to those obtained with non-dissolvable needles. Furthermore, as seen in brain tissue phantom agarose gel, the individual parameters of the insertion forces obtained with the dissolvable needles converge to those obtained with the non-dissolvable needles at high speeds. Interestingly, different from the agarose gel, in the brain tissue, even the friction force, which increases significantly at low velocity, converges at high insertion speeds.

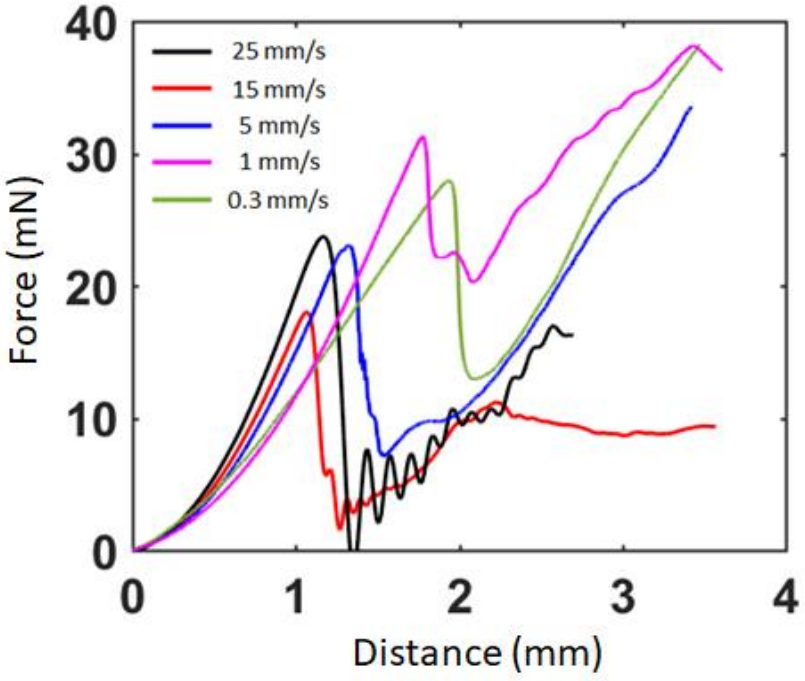

Figure 4.31: Insertion force profile for CMC/Glu (210 µm, 30° angle, wedge tip) needle into brain at all insertion velocities. (Oscillations at 25 mm/s is due to sensor ringing effect).

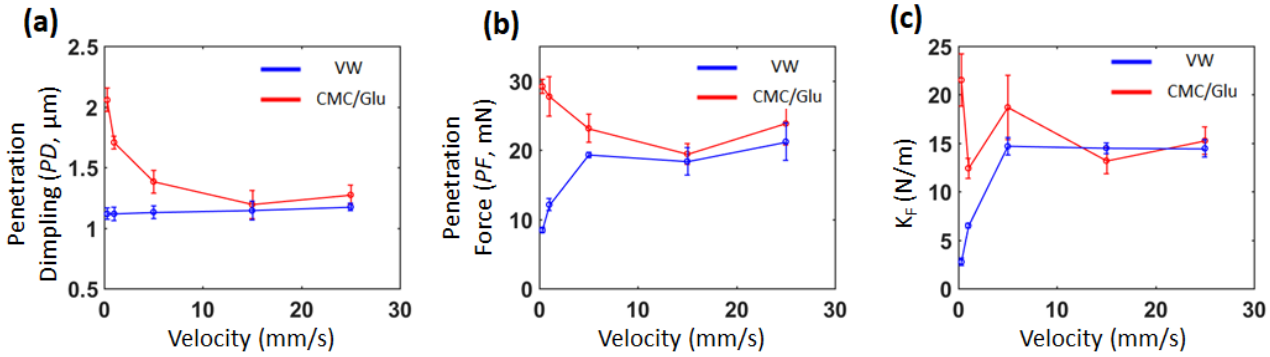

Figure 4.32: Effect of velocity on insertion force parameters for the insertion of wedge dissolvable needles into brain tissue and comparison with the non-dissolvable VeroWhite needles. **(a)** Penetration dimpling (*PD*), **(b)** Penetration force (*PF*), **(c)** K_F (friction force/length)

Sharp needles

Figure 4.33 shows the effect of insertion velocity on insertion forces for dissolvable pyramid tip needles in the brain tissue. It is observed that at lower speeds, penetration dimpling is significantly higher (i.e., 3times, Figure 4.34a) and there is no tip insertion region observed.

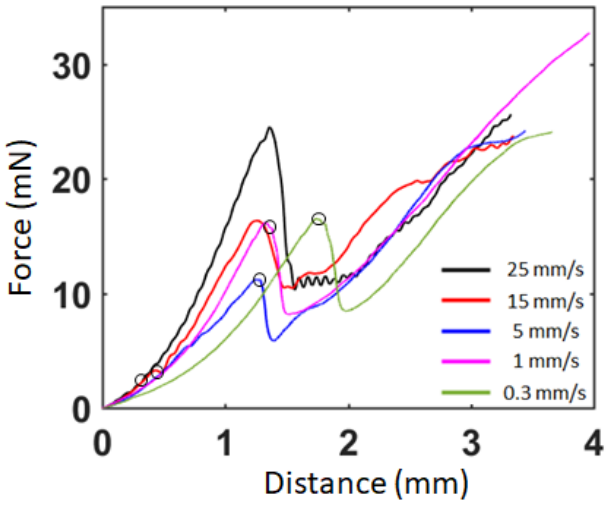

Figure 4.33: Insertion force profile for CMC/Glu (210 µm, 30° angle, pyramid tip and 6 µm radius) needle into brain tissue at all insertion velocities. (Penetrations points are marked with a circle).

Analysis of different parameters (Figure 4.34) shows that the blunting of the tip causes higher dimpling and behaves similar to wedge needle designs. Penetrations forces (Figure 4.34b) are 4 times higher at low speeds. Similar findings are observed for the friction forces (Figure 4.34c) due to absorption of water by the needle from the tissue. At high speeds, these parameters (*PD*, *PF* and K_F) converge to the ones obtained for VeroWhite needles.

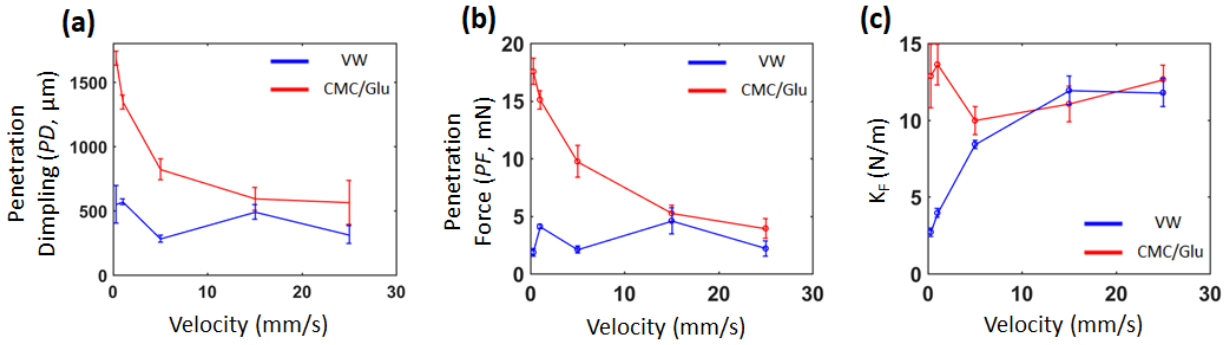

Figure 4.34: Effect of velocity on insertion force parameters for the insertion of sharp dissolvable needles into brain tissue and comparison with the non-dissolvable VeroWhite needles. **(a)** Penetration dimpling (*PD*), **(b)** Penetration force (*PF*), **(c)** K_F (friction force/length).

4.3 Summary and Conclusions

This chapter provided a fundamental understanding on the interaction between brain tissue/brain tissue phantom and dissolvable delivery vehicles through insertion studies performed

using a custom-made insertion setup. The following specific conclusions are drawn from this study:

- The designed and developed tailor-made sensor is capable of measuring mN level forces during the insertion of delivery vehicles into brain tissue phantom agarose gel and rat brain tissue accurately.
- Agarose gel, which has been extensively used in the literature, has substantially lower insertion forces than brain tissue. This difference is mainly due to the presence of arachnoid and pia layers at the brain surface. Dimpling amounts, penetration and friction forces, and elastic recovery are much larger in brain than those in agarose gel.
- Insertion speed critically affects the insertion forces in both brain tissue phantom agarose and actual brain tissue. In general, the insertion forces increase with the increasing insertion speed due to the strain hardening of the tissue. Furthermore, the tissue cutting mechanism changes at lower speeds (<1mm/s) from tissue shearing to tissue dragging. As such, the insertion speed needs to be optimized to avoid tissue dragging and to minimize the insertion forces.
- Tip geometry (tip radius and tip angle) plays a critical role in the interaction of delivery vehicle with the phantom brain tissue. While the tip radius controls the penetration event (i.e., penetration dimpling and force), the tip angle controls the tip force and secondary dimpling. As expected, the larger the tip radius and the tip angle of the delivery vehicles are, the higher the associated forces and dimpling amounts are. Therefore, it is important to have sharp needles with optimized apex angle to minimize the insertion forces.

- The tip type significantly affects the insertion forces. Fully 3D pyramid head needles with sharp tips have significantly lower penetration dimpling amounts and forces as compared to wedge and flat needles due to the reduced surface area at the tip.
- The cross-section area of the delivery needles is correlated with the friction forces. As expected, the insertion forces have an increasing trend with the increasing needle size. Furthermore, friction forces dominate the entire insertion force profile at higher speeds (>5 mm/s) as compared to the more significant tip forces at low speeds for brain tissue.
- The cross-section shape has negligible effect on the penetration dimpling amount and forces. The transition from the head to the stem portion of the needle affects the secondary dimpling. Specifically, secondary dimpling and elastic recovery are much lower with smooth transitions (i.e., circular designs).
- Non-dissolvable and dissolvable needles result in the similar mechanical interaction with the tissue at higher speeds. However, at lower speeds (<5 mm/s), biodissolvable needles become blunt due to the absorption of water from surrounding material, which leads to higher penetration forces and dimpling amount. Therefore, it is necessary to determine the minimum insertion velocity for the dissolvable probes to avoid the dissolution of the tip before the complete insertion.
- Insertion of biodissolvable needles results in higher forces at lower (<5 mm/s) speeds. Specifically, both the penetration and friction forces increase at lower velocities due to the blunting of the tip and increased surface area. On the other hand, at higher velocities the force parameters for biodissolvable needles converge to those obtained with the non-dissolvable needles.

Chapter 5

Conclusions and Future Work

5.1 Conclusions

This thesis introduced dissolvable delivery vehicles for ultra-miniature neural probes towards improving the functionality of the Brain Machine Interfaces. The mechanical mismatch between the brain tissue and traditional probes (e.g., silicon probes) is a major challenge for clinical applications of such neural interfaces: there is a considerable data in the literature that indicates that this mechanical mismatch is primarily responsible for the chronic damage (e.g., glial scar formation) that undermines the fidelity of action potentials measured from the brain.

Towards addressing this challenge, in this thesis, a novel manufacturing method was developed to integrate the sub-cellular sized probes (e.g., Px-Pt probe, 2.7 μm x 10 μm) with biodissolvable needles for reliable delivery of the probes to the targeted locations in the brain. Geometric characterization of the fabricated biodissolvable needles was performed to evaluate accuracy and reproducibility of the fabrication approach. Mechanical characterization of the fabricated needles demonstrated that the dissolvable delivery needles can successfully deliver the probes to the targeted location in both brain tissue phantoms and in actual brain tissue. Furthermore, it was shown that the direct bonding method ensures the insulation integrity of the probes and a broader design flexibility for the delivery vehicles. Based upon the work presented in this thesis, the following conclusions were drawn:

- The spin-casting process is a viable technique for accurate and reproducible fabrication of dissolvable delivery vehicles from a broad range of biodissolvable materials (e.g., glucose, maltodextrin and sucrose). The sugar-based materials have sufficient toughness for mechanical failure-free insertion into brain tissue. Such delivery vehicles can also co-deliver drugs along with ultra-miniature probes to mitigate the acute inflammatory response.
- Upon insertion into the brain, the biodissolvable needles absorb the water from the surrounding tissue and dissolve away over a period of time, thereby significantly reducing the chronic strains arising due to micromotion between the brain and skull.
- The direct assembly method, which integrates a separately spin-casted biodissolvable needle with a compliant probe, significantly increases the process yield with respect to co-manufacturing of the probe and the microneedles. Furthermore, this approach also enables utilizing more optimized delivery needles, such as those with sharp, pyramidal tips for reduced forces.
- The flexural based force measurement approach developed in this work is capable of measuring milli-Newton level forces accurately. The sensitivity of the load cell can be adjusted by changing the beam thickness.
- The insertion forces obtained from agarose and from freshly excised brain tissue are significantly different. This may be attributed to the presence of arachnoid and pia layers on the brain surface, resulting in large penetration/puncture forces and high dimpling; however, future research is needed to directly conclude this hypothesis. The force magnitudes, dimpling, and friction are all considerably larger in brain then in agarose. Notwithstanding, in many cases, the data in agarose shows the same trends as that in

brain, such as for the effect of insertion speed, tip sharpness, and other needle-geometry parameters.

- Strain hardening effect is also a major factor while choosing appropriate insertion velocity. Both the tip and friction forces increase with increased insertion velocity for the brain tissue.
- Tip geometry such as tip radius, tip angle and tip shapes (wedge and sharp) affect the forces at the tips significantly. At low velocities, the tissue interaction at tip changes from shearing to dragging, resulting in higher forces and visible damage to the surrounding phantom tissue. Increasing the insertion velocity compensates for the poor tip design to some extent. Although forces decrease due to mitigation of dragging effect when insertion velocity is increased, further increase in velocity leads to increase in insertion forces again due to strain hardening. Based on this knowledge, an optimal insertion velocity should be obtained for such designs.
- The biodissovable needles must be inserted at high speeds since the water from the tissue dissolves the needle tips, increasing its bluntness. Thus, at slower speeds (where the extent of blunting is larger), the penetration forces and the associated tissue damage increases considerably. Above a critical insertion speed, this blunting effect becomes negligible, and the data from the dissolvable needle converges with that from the non-dissolvable needle.

5.2 Future Work

5.2.1 Assessment of tissue damage for different needle designs and insertion speeds

Implantation of the neural probes using the delivery vehicles (i.e., biocompatible needles) to targeted brain regions is an invasive process, thereby resulting in brain tissue damage. The needle design parameters i.e., different material combinations (silk fibroin, polyethylene glycol (PEG), maltose, gelatin etc.) and geometries (fabricating and testing smaller cross sections than 100 μm x 100 μm), as well as insertion conditions affect the ensuing tissue damage. Therefore, it is necessary to probe the effect of delivery vehicle design and insertion parameters on the tissue damage. Most importantly, the correlation between the insertion mechanisms/forces and tissue damage should be studied for successful and minimally-invasive implantation of neural probes. To this end, a design of experiments matrix shown in Table 4.4 can be used. The insertion forces associated with these parameters can be measured and analyzed. The treated tissue samples can be frozen and sectioned to investigate the mechanical tissue damage occurring during the insertion. The relationship between the tissue damage and insertion forces can be evaluated to identify favorable delivery vehicle designs and insertion speeds. Glial scar formation due to different delivery vehicle designs (i.e., materials and geometries) and insertion speeds should also be evaluated, since it would directly affect the fidelity of recorded signals.

5.2.2 Vibration assisted insertion to reduce insertion force and tissue damage

Vibration assistance has the potential to reduce the insertion forces during the interaction of the delivery vehicles with the brain tissue [92]. The custom-made setup constructed in this thesis can be used for the vibration-assisted insertion experiments. However, these experiments will require an additional system to provide the vibration-assistance. Specifically, a piezoelectric

actuator can be used to provide the vibration assistance to the neural probe delivery vehicle at different frequencies and vibration amplitudes. To design the vibration assistance system, finite element simulations can be used to optimize the dynamic response of the piezoelectric actuator. Furthermore, since these experiments will be dynamic in nature as opposed to the static insertion forces measured in this thesis, they will require dynamic calibration of the load cell up to high frequencies through experimental modal analysis, where an impact excitation system with an embedded dynamic force sensor can be used to excite the load cell, while measuring the displacement output using a non-contact displacement sensor. Ultimately, a custom-made insertion setup for effective vibration-assisted insertion experiments can be constructed. Subsequently, the effect of insertion speed, vibration frequency, and vibration amplitude on insertion forces can be studied for different needle designs, and the effect of vibration frequency and amplitude on the insertion forces can be revealed. Finally, the favorable insertion speeds in the presence of vibration assistance can be determined to minimize the insertion forces.

Bibliography

[1] E. N. Brown, L. M. Frank, D. Tang, M. C. Quirk, and M. A. Wilson, "A statistical paradigm for neural spike train decoding applied to position prediction from ensemble firing patterns of rat hippocampal place cells.," *J. Neurosci.*, vol. 18, no. 18, pp. 7411–25, Sep. 1998.

[2] E. E. Fetz and D. V. Finocchio, "Correlations between activity of motor cortex cells and arm muscles during operantly conditioned response patterns," *Exp. Brain Res.*, vol. 23, no. 3, pp. 217–240, Sep. 1975.

[3] T. D. Y. Kozai *et al.*, "Comprehensive chronic laminar single-unit, multi-unit, and local field potential recording performance with planar single shank electrode arrays," *J. Neurosci. Methods*, vol. 242, pp. 15–40, Mar. 2015.

[4] A. P. Georgopoulos, A. B. Schwartz, and R. E. Kettner, "Neuronal population coding of movement direction.," *Science*, vol. 233, no. 4771, pp. 1416–9, Sep. 1986.

[5] W. J. Kargo and D. A. Nitz, "Early skill learning is expressed through selection and tuning of cortically represented muscle synergies.," *J. Neurosci.*, vol. 23, no. 35, pp. 11255–69, Dec. 2003.

[6] D. J. Krupa *et al.*, "Immediate thalamic sensory plasticity depends on corticothalamic feedback.," *Proc. Natl. Acad. Sci. U. S. A.*, vol. 96, no. 14, pp. 8200–5, Jul. 1999.

[7] A. B. Schwartz and D. W. Moran, "Arm trajectory and representation of movement processing in motor cortical activity," *Eur. J. Neurosci.*, vol. 12, no. 6, pp. 1851–1856, Jun. 2000.

[8] D. M. Taylor, S. I. H. Tillery, A. B. Schwartz, S. J. Rowan, and C. Weder, "Direct cortical

control of 3D neuroprosthetic devices.," *Science*, vol. 296, no. 5574, pp. 1829–32, Jun. 2002.

[9] J. Bartels *et al.*, "Neurotrophic electrode: Method of assembly and implantation into human motor speech cortex," *J. Neurosci. Methods*, vol. 174, no. 2, pp. 168–176, Sep. 2008.

[10] D. McCreery, A. Lossinsky, V. Pikov, and X. Liu, "Microelectrode Array for Chronic Deep-Brain Microstimulation and Recording," *IEEE Trans. Biomed. Eng.*, vol. 53, no. 4, pp. 726–737, Apr. 2006.

[11] K. L. Drake, K. D. Wise, J. Farraye, D. J. Anderson, and S. L. BeMent, "Performance of planar multisite microprobes in recording extracellular single-unit intracortical activity," *IEEE Trans. Biomed. Eng.*, vol. 35, no. 9, pp. 719–732, 1988.

[12] T. D. Y. Kozai *et al.*, "Effects of caspase-1 knockout on chronic neural recording quality and longevity: Insight into cellular and molecular mechanisms of the reactive tissue response," *Biomaterials*, vol. 35, no. 36, pp. 9620–9634, Dec. 2014.

[13] Y. T. Kim, R. W. Hitchcock, M. J. Bridge, and P. A. Tresco, "Chronic response of adult rat brain tissue to implants anchored to the skull," *Biomaterials*, vol. 25, no. 12, pp. 2229–2237, 2004.

[14] V. S. Polikov, P. A. Tresco, and W. M. Reichert, "Response of brain tissue to chronically implanted neural electrodes," *J. Neurosci. Methods*, vol. 148, no. 1, pp. 1–18, 2005.

[15] N. Alba, Z. Du, K. Catt, T. Kozai, and X. Cui, "In Vivo Electrochemical Analysis of a PEDOT/MWCNT Neural Electrode Coating," *Biosensors*, vol. 5, no. 4, pp. 618–646, Oct. 2015.

[16] T. D. Y. Kozai, A. S. Jaquins-Gerstl, A. L. Vazquez, A. C. Michael, and X. T. Cui, "Brain Tissue Responses to Neural Implants Impact Signal Sensitivity and Intervention

Strategies," *ACS Chem. Neurosci.*, vol. 6, no. 1, pp. 48–67, Jan. 2015.

[17] T. D. Y. Kozai, N. A. Alba, H. Zhang, N. A. Kotov, R. A. Gaunt, and X. T. Cui, "Nanostructured Coatings for Improved Charge Delivery to Neurons," in *Nanotechnology and Neuroscience: Nano-electronic, Photonic and Mechanical Neuronal Interfacing*, New York, NY: Springer New York, 2014, pp. 71–134.

[18] P. J. Rousche and R. A. Normann, "Chronic recording capability of the Utah Intracortical Electrode Array in cat sensory cortex," *J. Neurosci. Methods*, vol. 82, no. 1, pp. 1–15, Jul. 1998.

[19] K. C. Cheung, K. Djupsund, Y. Dan, and L. P. Lee, "Implantable multichannel electrode array based on soi technology," *J. Microelectromechanical Syst.*, vol. 12, no. 2, pp. 179–184, Apr. 2003.

[20] P. T. McCarthy, K. J. Otto, and M. P. Rao, "Robust penetrating microelectrodes for neural interfaces realized by titanium micromachining," *Biomed. Microdevices*, vol. 13, no. 3, pp. 503–515, Jun. 2011.

[21] H.-Y. Chan, M. Varney, S. Hatch, and D. M. Aslam, "Implantable polycrystalline diamond neural probe for in vivo and in vitro physiological recording," in *TRANSDUCERS 2009 - 2009 International Solid-State Sensors, Actuators and Microsystems Conference*, 2009, pp. 1202–1205.

[22] Ho-Yin Chan, D. M. Aslam, J. A. Wiler, and B. Casey, "A Novel Diamond Microprobe for Neuro-Chemical and -Electrical Recording in Neural Prosthesis," *J. Microelectromechanical Syst.*, vol. 18, no. 3, pp. 511–521, Jun. 2009.

[23] P. T. McCarthy, M. P. Rao, and K. J. Otto, "Simultaneous recording of rat auditory cortex and thalamus via a titanium-based, microfabricated, microelectrode device," *J. Neural Eng.*, vol. 8, no. 4, p. 046007, Aug. 2011.

[24] T. Escamilla-Mackert, N. B. Langhals, T. D. Y. Kozai, and D. R. Kipke, "Insertion of a three dimensional silicon microelectrode assembly through a thick meningeal membrane," in *2009 Annual International Conference of the IEEE Engineering in Medicine and Biology Society*, 2009, pp. 1616–1618.

[25] R. Biran, D. C. Martin, and P. A. Tresco, "Neuronal cell loss accompanies the brain tissue response to chronically implanted silicon microelectrode arrays," *Exp. Neurol.*, vol. 195, no. 1, pp. 115–126, 2005.

[26] G. C. McConnell, H. D. Rees, A. I. Levey, C.-A. Gutekunst, R. E. Gross, and R. V Bellamkonda, "Implanted neural electrodes cause chronic, local inflammation that is correlated with local neurodegeneration," *J. Neural Eng.*, vol. 6, no. 5, p. 056003, Oct. 2009.

[27] J. T. Neary, Y. Kang, K. A. Willoughby, and E. F. Ellis, "Activation of extracellular signal-regulated kinase by stretch-induced injury in astrocytes involves extracellular ATP and P2 purinergic receptors.," *J. Neurosci.*, vol. 23, no. 6, pp. 2348–56, Mar. 2003.

[28] S. Metz, A. Bertsch, D. Bertrand, and P. Renaud, "Flexible polyimide probes with microelectrodes and embedded microfluidic channels for simultaneous drug delivery and multi-channel monitoring of bioelectric activity," *Biosens. Bioelectron.*, vol. 19, no. 10, pp. 1309–1318, May 2004.

[29] J. P. Seymour and D. R. Kipke, "Neural probe design for reduced tissue encapsulation in CNS," *Biomaterials*, vol. 28, no. 25, pp. 3594–3607, 2007.

[30] T. D. Yoshida Kozai *et al.*, "Ultrasmall implantable composite microelectrodes with bioactive surfaces for chronic neural interfaces," *Nat. Mater.*, vol. 11, no. 12, pp. 1065–1073, 2012.

[31] T. D. Y. Kozai *et al.*, "Chronic *In Vivo* Evaluation of PEDOT/CNT for Stable Neural

Recordings," *IEEE Trans. Biomed. Eng.*, vol. 63, no. 1, pp. 111–119, Jan. 2016.

[32] C. L. Kolarcik *et al.*, "Elastomeric and soft conducting microwires for implantable neural interfaces," *Soft Matter*, vol. 11, no. 24, pp. 4847–4861, Jun. 2015.

[33] J. R. Capadona, K. Shanmuganathan, D. J. Tyler, S. J. Rowan, and C. Weder, "Stimuli-responsive polymer nanocomposites inspired by the sea cucumber dermis.," *Science*, vol. 319, no. 5868, pp. 1370–4, Mar. 2008.

[34] B. A. Wester, R. H. Lee, and M. C. LaPlaca, "Development and characterization of in vivo flexible electrodes compatible with large tissue displacements.," *J. Neural Eng.*, vol. 6, no. 2, p. 024002, 2009.

[35] J. P. Seymour, Y. M. Elkasabi, H.-Y. Chen, J. Lahann, and D. R. Kipke, "The insulation performance of reactive parylene films in implantable electronic devices," *Biomaterials*, vol. 30, no. 31, pp. 6158–6167, Oct. 2009.

[36] Changlin Pang *et al.*, "A New Multi-Site Probe Array with Monolithically Integrated Parylene Flexible Cable for Neural Prostheses," in *2005 IEEE Engineering in Medicine and Biology 27th Annual Conference*, 2005, pp. 7114–7117.

[37] P. R. Patel *et al.*, "Chronic *in vivo* stability assessment of carbon fiber microelectrode arrays," *J. Neural Eng.*, vol. 13, no. 6, p. 066002, Dec. 2016.

[38] D. P. O'Brien, T. R. Nichols, and M. G. Allen, "Flexible microelectrode arrays with integrated insertion devices," *Tech. Dig. MEMS 2001. 14th IEEE Int. Conf. Micro Electro Mech. Syst. (Cat. No.01CH37090)*, vol. 00, pp. 216–219.

[39] T. D. Y. Kozai and D. R. Kipke, "Insertion shuttle with carboxyl terminated self-assembled monolayer coatings for implanting flexible polymer neural probes in the brain," *J. Neurosci. Methods*, vol. 184, no. 2, pp. 199–205, 2009.

[40] P. J. Gilgunn *et al.*, "An ultra-compliant, scalable neural probe with molded biodissolvable

delivery vehicle," in *2012 IEEE 25th International Conference on Micro Electro Mechanical Systems (MEMS)*, 2012, pp. 56–59.

[41] W. F. H. Rakuman *et al.*, "Ultra-compliant neural probes are subject to fluid forces during dissolution of polymer delivery vehicles," in *2013 35th Annual International Conference of the IEEE Engineering in Medicine and Biology Society (EMBC)*, 2013, pp. 1550–1553.

[42] G. Lind, C. E. Linsmeier, J. Thelin, and J. Schouenborg, "Gelatine-embedded electrodes—a novel biocompatible vehicle allowing implantation of highly flexible microelectrodes," *J. Neural Eng.*, vol. 7, no. 4, p. 046005, Aug. 2010.

[43] D. Lewitus, K. L. Smith, W. Shain, and J. Kohn, "Ultrafast resorbing polymers for use as carriers for cortical neural probes," *Acta Biomater.*, vol. 7, no. 6, pp. 2483–2491, 2011.

[44] D. Y. Lewitus, K. L. Smith, W. Shain, D. Bolikal, and J. Kohn, "The fate of ultrafast degrading polymeric implants in the brain," *Biomaterials*, vol. 32, no. 24, pp. 5543–5550, 2011.

[45] A. Lecomte *et al.*, "Silk and PEG as means to stiffen a parylene probe for insertion in the brain: Toward a double time-scale tool for local drug delivery," *J. Micromechanics Microengineering*, vol. 25, no. 12, 2015.

[46] J. Agorelius, F. Tsanakalis, A. Friberg, P. T. Thorbergsson, L. M. E. Pettersson, and J. Schouenborg, "An array of highly flexible electrodes with a tailored configuration locked by gelatin during implantation—initial evaluation in cortex cerebri of awake rats," *Front. Neurosci.*, vol. 9, p. 331, Sep. 2015.

[47] F. Wu, L. Tien, F. Chen, D. Kaplan, J. Berke, and E. Yoon, "A multi-shank silk-backed parylene neural probe for reliable chronic recording," in *2013 Transducers & Eurosensors XXVII: The 17th International Conference on Solid-State Sensors, Actuators and Microsystems (TRANSDUCERS & EUROSENSORS XXVII)*, 2013, pp. 888–891.

[48] V. S. Polikov, P. A. Tresco, and W. M. Reichert, "Response of brain tissue to chronically implanted neural electrodes," *J. Neurosci. Methods*, vol. 148, no. 1, pp. 1–18, Oct. 2005.

[49] A. Andrei, M. Welkenhuysen, B. Nuttin, and W. Eberle, "A response surface model predicting the *in vivo* insertion behavior of micromachined neural implants," *J. Neural Eng.*, vol. 9, no. 1, p. 016005, Feb. 2012.

[50] D. J. Edell, V. V. Toi, V. M. McNeil, and L. D. Clark, "Factors influencing the biocompatibility of insertable silicon microshafts in cerebral cortex," *IEEE Trans. Biomed. Eng.*, vol. 39, no. 6, pp. 635–643, Jun. 1992.

[51] W. Jensen, K. Yoshida, and U. G. Hofmann, "In-vivo implant mechanics of flexible, silicon-based ACREO microelectrode arrays in rat cerebral cortex," *IEEE Trans. Biomed. Eng.*, vol. 53, no. 5, pp. 934–940, May 2006.

[52] M. Welkenhuysen, A. Andrei, L. Ameye, W. Eberle, and B. Nuttin, "Effect of Insertion Speed on Tissue Response and Insertion Mechanics of a Chronically Implanted Silicon-Based Neural Probe," *IEEE Trans. Biomed. Eng.*, vol. 58, no. 11, pp. 3250–3259, Nov. 2011.

[53] Y.-T. Kim, R. W. Hitchcock, M. J. Bridge, and P. A. Tresco, "Chronic response of adult rat brain tissue to implants anchored to the skull," *Biomaterials*, vol. 25, no. 12, pp. 2229–2237, May 2004.

[54] A. Lecomte, E. Descamps, and C. Bergaud, "A review on mechanical considerations for chronically-implanted neural probes," *J. Neural Eng.*, vol. 15, no. 3, p. 031001, Jun. 2018.

[55] C. Hassler, R. P. von Metzen, P. Ruther, and T. Stieglitz, "Characterization of parylene C as an encapsulation material for implanted neural prostheses," *J. Biomed. Mater. Res. Part B Appl. Biomater.*, vol. 9999B, no. 1, p. NA-NA, Apr. 2010.

[56] J.-M. Hsu, L. Rieth, R. A. Normann, P. Tathireddy, and F. Solzbacher, "Encapsulation of

an Integrated Neural Interface Device With Parylene C," *IEEE Trans. Biomed. Eng.*, vol. 56, no. 1, pp. 23–29, Jan. 2009.

[57] A. Gilletti and J. Muthuswamy, "Brain micromotion around implants in the rodent somatosensory cortex," *J. Neural Eng.*, vol. 3, no. 3, pp. 189–195, Sep. 2006.

[58] J. Subbaroyan, D. C. Martin, and D. R. Kipke, "A finite-element model of the mechanical effects of implantable microelectrodes in the cerebral cortex," *J. Neural Eng.*, vol. 2, no. 4, pp. 103–113, Dec. 2005.

[59] H. Lee, R. V. Bellamkonda, W. Sun, and M. E. Levenston, "Biomechanical analysis of silicon microelectrode-induced strain in the brain," *J. Neural Eng.*, vol. 2, no. 4, pp. 81–89, 2005.

[60] L. Karumbaiah *et al.*, "The upregulation of specific interleukin (IL) receptor antagonists and paradoxical enhancement of neuronal apoptosis due to electrode induced strain and brain micromotion," *Biomaterials*, vol. 33, no. 26, pp. 5983–5996, Sep. 2012.

[61] R. Zhu, G. L. Huang, H. Yoon, C. S. Smith, and V. K. Varadan, "Biomechanical Strain Analysis at the Interface of Brain and Nanowire Electrodes on a Neural Probe," *J. Nanotechnol. Eng. Med.*, vol. 2, no. 3, p. 031001, Aug. 2011.

[62] C. S. Bjornsson *et al.*, "Effects of insertion conditions on tissue strain and vascular damage during neuroprosthetic device insertion," *J. Neural Eng.*, vol. 3, no. 3, pp. 196–207, Sep. 2006.

[63] M. D. Johnson, O. E. Kao, and D. R. Kipke, "Spatiotemporal pH dynamics following insertion of neural microelectrode arrays," *J. Neurosci. Methods*, vol. 160, no. 2, pp. 276–287, Mar. 2007.

[64] N. T. Markwardt, J. Stokol, and R. L. Rennaker II, "Sub-meninges implantation reduces immune response to neural implants," *J. Neurosci. Methods*, vol. 214, no. 2, pp. 119–125,

Apr. 2013.

[65] T. D. Y. Kozai, J. R. Eles, A. L. Vazquez, and X. T. Cui, “Two-photon imaging of chronically implanted neural electrodes: Sealing methods and new insights,” *J. Neurosci. Methods*, vol. 258, pp. 46–55, Jan. 2016.

[66] A. J. Sawyer and T. R. Kyriakides, “Nanoparticle-based evaluation of blood–brain barrier leakage during the foreign body response,” *J. Neural Eng.*, vol. 10, no. 1, p. 016013, Feb. 2013.

[67] T. D. Y. Kozai *et al.*, “Mechanical failure modes of chronically implanted planar silicon-based neural probes for laminar recording,” *Biomaterials*, vol. 37, pp. 25–39, Jan. 2015.

[68] K.-K. Lee *et al.*, “Polyimide-based intracortical neural implant with improved structural stiffness,” *J. Micromechanics Microengineering*, vol. 14, no. 1, pp. 32–37, Jan. 2004.

[69] D.-H. Kim and D. C. Martin, “Sustained release of dexamethasone from hydrophilic matrices using PLGA nanoparticles for neural drug delivery,” *Biomaterials*, vol. 27, no. 15, pp. 3031–3037, May 2006.

[70] D. H. Kim *et al.*, “Dissolvable films of silk fibroin for ultrathin conformal bio-integrated electronics,” *Nat. Mater.*, vol. 9, no. 6, pp. 1–7, 2010.

[71] Z. Xiang *et al.*, “Ultra-thin flexible polyimide neural probe embedded in a dissolvable maltose-coated microneedle,” *J. Micromechanics Microengineering*, vol. 24, no. 6, 2014.

[72] S. Takeuchi, T. Suzuki, K. Mabuchi, and H. Fujita, “3D flexible multichannel neural probe array,” *J. Micromechanics Microengineering*, vol. 14, no. 1, pp. 104–107, 2004.

[73] W. Shen *et al.*, “Extracellular matrix-based intracortical microelectrodes: Toward a microfabricated neural interface based on natural materials,” *Microsystems Nanoeng.*, vol. 1, no. 1, p. 15010, Dec. 2015.

[74] F. Casanova, P. R. Carney, and M. Sarntinoranont, “In vivo evaluation of needle force and

friction stress during insertion at varying insertion speed into the brain," *J. Neurosci. Methods*, vol. 237, pp. 79–89, Nov. 2014.

[75] A. A. Sharp, A. M. Ortega, D. Restrepo, D. Curran-Everett, and K. Gall, "*In Vivo* Penetration Mechanics and Mechanical Properties of Mouse Brain Tissue at Micrometer Scales," *IEEE Trans. Biomed. Eng.*, vol. 56, no. 1, pp. 45–53, Jan. 2009.

[76] S. Deitch Mark Choi, "Brain Model for Microelectrode Implantation Testing."

[77] N. Haj Hosseini, R. Hoffmann, S. Kisban, T. Stieglitz, O. Paul, and P. Ruther, "Comparative study on the insertion behavior of cerebral microprobes," in *2007 29th Annual International Conference of the IEEE Engineering in Medicine and Biology Society*, 2007, pp. 4711–4714.

[78] R. Pomfret, G. Miranpuri, and K. Sillay, "The substitute brain and the potential of the gel model," *Ann. Neurosci.*, vol. 20, no. 3, pp. 118–122, 2013.

[79] Z.-J. Chen *et al.*, "A realistic brain tissue phantom for intraparenchymal infusion studies," *J. Neurosurg.*, vol. 101, no. 2, pp. 314–322, Aug. 2004.

[80] F. Casanova, P. R. Carney, and M. Sarntinoranont, "Influence of Needle Insertion Speed on Backflow for Convection-Enhanced Delivery," *J. Biomech. Eng.*, vol. 134, no. 4, p. 041006, Apr. 2012.

[81] F. Casanova, P. R. Carney, and M. Sarntinoranont, "In vivo evaluation of needle force and friction stress during insertion at varying insertion speed into the brain," *J. Neurosci. Methods*, vol. 237, pp. 79–89, Nov. 2014.

[82] L. Barrangou, "Sensory Texture and Fundamental Rheology of Agar and Agarose Gels," Jan. 2006.

[83] S. Budday *et al.*, "Mechanical properties of gray and white matter brain tissue by indentation.," *J. Mech. Behav. Biomed. Mater.*, vol. 46, pp. 318–30, Jun. 2015.

[84] T. D. Y. Kozai *et al.*, "Chronic tissue response to carboxymethyl cellulose based dissolvable insertion needle for ultra-small neural probes," *Biomaterials*, vol. 35, no. 34, pp. 9255–9268, Nov. 2014.

[85] R. Khilwani *et al.*, "Ultra-miniature ultra-compliant neural probes with dissolvable delivery needles: design, fabrication and characterization," *Biomed. Microdevices*, vol. 18, no. 6, p. 97, Dec. 2016.

[86] A. Weltman, J. Yoo, and E. Meng, "Flexible, Penetrating Brain Probes Enabled by Advances in Polymer Microfabrication," *Micromachines*, vol. 7, no. 10, p. 180, Oct. 2016.

[87] B. Bediz *et al.*, "Dissolvable Microneedle Arrays for Intradermal Delivery of Biologics: Fabrication and Application," *Pharm. Res.*, vol. 31, no. 1, pp. 117–135, Jan. 2014.

[88] E. Korkmaz *et al.*, "Therapeutic intradermal delivery of tumor necrosis factor-alpha antibodies using tip-loaded dissolvable microneedle arrays," *Acta Biomater.*, vol. 24, pp. 96–105, Sep. 2015.

[89] E. Korkmaz *et al.*, "Tip-Loaded Dissolvable Microneedle Arrays Effectively Deliver Polymer-Conjugated Antibody Inhibitors of Tumor-Necrosis-Factor-Alpha Into Human Skin.," *J. Pharm. Sci.*, vol. 105, no. 11, pp. 3453–3457, Nov. 2016.

[90] E. Korkmaz, "Biodissolvable Microneedle Arrays for Effective Transdermal and Intradermal Delivery of Vaccines and Therapeutics: Manufacturing and Cutaneous Applications," *Dissertations*, Aug. 2016.

[91] X. Jin, K. H. Yang, and A. I. King, "Mechanical properties of bovine pia–arachnoid complex in shear," *J. Biomech.*, vol. 44, no. 3, pp. 467–474, Feb. 2011.

[92] P.-C. Chen and A. Lal, "Detachable ultrasonic enabled inserter for neural probe insertion using biodissolvable Polyethylene Glycol," in *2015 Transducers - 2015 18th International Conference on Solid-State Sensors, Actuators and Microsystems (TRANSDUCERS)*, 2015